University of Ljubljana
Faculty of Mathematics and Physics

Simon Širca

The axial form factor of the nucleon from coincident pion electro-production at low Q^2

Doctoral dissertation

Supervisor: prof. dr. Milan Potokar
Co-supervisor: prof. dr. Thomas Walcher

Ljubljana, 1999

To my mother, and other teachers.

I would like to thank my supervisor Prof. Dr. Milan Potokar for giving me the opportunity to face the challenges of experimental nuclear physics as a member of the A1 Collaboration at the Nuclear Physics Institute of the Mainz University, and for his continuous interest in my work. My experimental co-supervisor Prof. Dr. Thomas Walcher deserves my gratitude for his confidence in assigning to me the 'hot topic' of the axial form factor, and for many food-for-thought discussions and goal-oriented incentives. I am also indebted to Prof. Dr. Reiner Neuhausen who constantly assisted in making my visits to Mainz possible, and to Dr. habil. Günther Rosner for help during the experiment and data analysis.

I thank my theoretical co-supervisor Prof. Dr. Bojan Golli for keeping a watchful eye over my work. Ever since my final year as an undergraduate, his instinct and experience in physics were often stepping-stones that protected me from wading the stream of erroneous ideas, pitfalls and dead-alleys of calculations. I am also grateful to Prof. Dr. Manuel Fiolhais who enabled me to visit the University of Coimbra twice, and to Dr. Pedro Alberto and Dr. Jose Amoreira, who succeeded in making these stays even more fruitful and pleasant.

The experimental part of my work could not have been started, let alone accomplished, without the help of all members of the A1 Collaboration. I have repeatedly resorted to this source of knowledge, which seems to embody the Feynman's vision of the "expanding frontier of ignorance". But my particular thanks go to Dipl. Phys. Arnd Liesenfeld, Dr. Michael Distler, Dr. Richard Florizone, Dr. Harald Merkel, Dr. Ulrich Müller, Dipl. Phys. Axel Wagner, Dipl. Phys. Ralph Böhm, and mag. Klemen Bohinc for helping me, everyone in his own way. Arnd Liesenfeld is an outstanding exception I wish to highlight — his immense patience, his rich experience, and his readiness to help show even the Feynman's frontier in a friendlier perspective.

At the end, I owe gratitude to my family and ask their forgiveness for me sacrificing much of the spare time to this work instead of to them.

Abstract

Near-threshold electro-production of charged pions on protons at low Q^2 is a contemporary, precise tool to study the axial-vector form factor of the nucleon, which is intimately related to calculations of chiral perturbation theory and to chiral quark models of nucleon structure.

This thesis discusses the acquisition and the analysis of the $p(e, e'\pi^+)n$ data obtained in a coincidence experiment performed with the A1 Collaboration at the Nuclear physics institute of the Mainz University, at $W = 1125\,\mathrm{MeV}$ and at $Q^2 = 0.117$, 0.195 and $0.273\,(\mathrm{GeV}/c)^2$. The transverse and the longitudinal cross-sections are determined from the measured cross-sections using the Rosenbluth method, and the axial form factor with the corresponding axial mass parameter are extracted from the transverse part. In addition, the axial form factor of the nucleon is calculated in the framework of the quark-level linear sigma model and the chromodielectric model, where centre-of-mass and recoil effects are eliminated.

Keywords: electro-production of pions on the nucleon, coincidence experiments with electrons, structure functions, axial form factor, chiral perturbation theory, linear sigma model, chromodielectric model, CMS corrections, recoil corrections.

PACS (1998): 13.60.Le, 14.20.Dh, 12.39.–x, 12.39.Fe .

Contents

1. Introduction **1**

2. General formalism **6**

2.1 The expression for the reaction cross-section 6

2.2 Motivation for the separation of the structure functions and extraction of G_A . . . 11

3. Experimental setup **16**

3.1 The MaMi–B accelerator 16

3.2 The hydrogen cryo-target and the beam wobbler 17

3.3 Magnetic spectrometers and detector systems 20

3.4 Electronics 25

4. Data analysis **29**

4.1 Coincidence time 29

4.2 Missing mass 31

4.3 Further background reduction 33

4.4 Detector efficiencies 34

4.5 Correction factors 37

4.6 Luminosity 40

4.7 Spectrometer acceptances 42

4.8 The differential cross-section 43

5. Extracting $G_A(q^2)$ from experiment **47**

5.1 Early theories 48

5.2 The DT model 49

5.3 Chiral perturbation theory 51

6. Calculation of the nucleon axial form factor **53**

6.1 The axial-vector coupling constant 53

6.2 Definition of $G_A(q^2)$ 58

6.3 $G_A(q^2)$ in the MIT bag and in models with a scalar confining potential 58

6.4 $G_A(q^2)$ in the LSM and the CDM 59

7. Summary and outlook **67**

Appendix **69**

A Extracting M_A from (anti)neutrino scattering experiments **69**

B Multipole expansion **71**

C Isospin decomposition **76**

D Corrections of radiation losses in $p(e, e'\pi^+)n$ **77**

E The DHKT model **82**

F The Lagrangians of the LSM and the CDM **84**

G The model wave-function of the LSM and the CDM **86**

H Evaluation of $G_A(q^2)$ in the LSM and the CDM: technical details **88**

H.1 The quark contribution to the term with $j_0(qr)$ 88

H.2 The quark contribution to the term with $j_2(qr)$ 89

H.3 The meson contribution to the term with $j_0(qr)$ 91

H.4 The meson contribution to the term with $j_2(qr)$ 93

H.5 The norm overlap 94

References **97**

1

Introduction

Der wahre Weg geht über ein Seil,
das nicht in der Höhe gespannt ist,
sondern knapp über dem Boden.
Es scheint mehr bestimmt stolpern zu machen,
als begangen zu werden.

Franz Kafka

For the past four decades, nuclear and particle physics research focuses on *coincidence experiments*, in which the target nuclei are probed by either hadron or electron beams. In these measurements, the scattered projectile is detected in coincidence with the ejected particle or the residual nucleus. Since the hadronic cross-sections are usually large, *hadronic* probes were successfully used in the early coincidence measurements, even though the accelerator duty factors were rather low and the underlying interaction was poorly known. In a typical experiment of the time, e. g. $A(p,pp)A-1$, the scattered protons were detected in coincidence with the protons ejected from the nucleus A [1].

But the physical picture of such processes was obscured by the ignorance of both strong interaction matrix elements, the studied one (in the output channel) as well as the one that represents the excitation of the system under study (in the entrance channel). This meant that the extracted physical knowledge largely depended on the ability of certain models to describe the strong interaction. Coincidence measurements were therefore mostly limited to processes of minimal complexity, for example, to quasi-elastic scattering, where particular kinematical conditions can be chosen in which the hadronic projectile probes almost free nucleons within the nucleus; at the same time, the interaction between the ejected nucleon and the residual nucleus is negligible in the first approximation. It should be stressed, however, that the accuracy of the experiments does grow over years and that the sophistication of the models gradually improves. For example, recent theoretical analyses of the $p(p,p'\pi^+)n$ process [2] based on the one-pion exchange approximation parameterised in terms of the DWBA t-matrix for the first step of $pp \to n\Delta^{++}(p\Delta^+) \to np\pi^+$, agrees remarkably well with the accurate coincidence data of [3].

Nevertheless, experiments with *electron beams* that evolved later on introduced a major improvement in the field. Electrons are point-like particles without internal structure or excited states. In addition, the electro-magnetic interaction of the electrons with the probed particles is well understood, and has a relatively weak coupling constant. Contrary to hadronic projectiles probing only the nuclear surface, electrons therefore penetrate deeply into the target nucleus and interact without disturbing other nuclear constituents. The interaction of an electron with a light nucleus can be visualised as an exchange of a single virtual photon, and first order perturbation approach is usually sufficient to describe the electro-magnetic parts of the reaction amplitudes in the interpretation of experimental results.

Electron scattering experiments can be classified into two groups, depending on whether any hadrons are detected in coincidence with the scattered electron or not. In *inclusive* measurements, the final nuclear state is not unique. Since the scattered electron is the only detected particle, several nuclear states are effectively summed over in the cross-section. In *exclusive* experiments, the scattered electron is detected in coincidence with one or more ejected or recoiled hadrons, and only a specific final state is considered. Since the electro-magnetic interaction cross-sections are small, coincidence experiments with electrons were impossible in the early days of pulsed, low duty-factor accelerators, even though these provided high peak currents. The detectors and spectrometers used to identify and analyse the reaction products were not capable of handling these short, intense particle bursts. In addition, they had small angular and momentum acceptances.

Exclusive measurements of one nucleon knock-out reactions $A(e,e'p)B$ [4] or pion electro-production $A(e,e'\pi)B$ [5] were among the first modern electron coincidence experiments. In the $(e,e'p)$ measurements, in which the momentum of the ejected proton is determined simultaneously with the momentum of the electron, the extracted reaction amplitudes directly reflect the Fourier transforms of the corresponding part of the nuclear wave-function. If the incoming electron also excites one of the target nucleons into an excited state, the measured final hadron can be linked to the decay of the corresponding resonant state and to its propagation through the nuclear medium. Moreover, the coincidence cross-section allows access to a narrower set of matrix elements (with their magnitudes and relative phases) which are unattainable in the inclusive cross-section, and thereby convey a richer information on the nuclear structure.

Similarly, coincidence reactions like $N(e,e'\pi)N'$ offer an insight into the structure of the nucleon. The pioneering coincidence experiments of pion electro-production on the nucleon were carried out about three decades ago at DESY in Hamburg, in Saclay, Frascati, Bonn, Manchester, and other European laboratories (see [6] and references quoted in section 2.2 for a review). Unfortunately, the experimental data were burdened with large statistical and systematical uncertainties for the reasons enumerated above.

Today, new electron accelerators with high duty-factors or continuous electron beams (MIT–Bates, NIKHEF, MaMi, TJNAF) and highly efficient detector systems enable us to significantly improve the accuracy of the experiments. Among the observables that can be measured with these modern setups, or re-measured with much lower uncertainties, the electroweak form factors of the nucleon are among the most relevant. Simultaneously, quantum chromodynamics (QCD) evolved as the fundamental theory of the strong interactions [7], giving birth or inspiring several effective theories and models of hadron structure. In particular, the chiral perturbation theory (χPT) recently emerged as an effective field theory of the standard model below the chiral symmetry breaking scale [8]. Modern detector setups allow us to access previously unattainable kinematical regions of the nucleon-pion processes, in which the perturbative QCD approach is inappropriate, so these new measurements may serve not only as constraints on the existing models of the nucleon structure, but also as a testing ground of χPT predictions.

Particularly the *axial form factor* of the nucleon recently received intense renewed attention because of sizeable inconsistencies in the world supply of data available to date. There are basically two methods to determine this form factor. One set of experimental data comes from measurements of quasi-elastic (anti)neutrino scattering on protons [9, 10, 11], deuterons [12, 13, 14, 15, 16] and other nuclei (Al, Fe) [17, 18] or composite targets like freon [19, 20, 21, 22] and propane [22, 23]. The procedure [1] followed in the extraction of the axial form factor is to fit the q^2-dependence of the (anti)neutrino-nucleon cross-section

$$\frac{d\sigma^{\nu,\overline{\nu}}}{dq^2} \propto A(q^2) \pm B(q^2)\,\frac{s-u}{M} + C(q^2)\,\frac{(s-u)^2}{M}\,,$$

in which the axial form factor $G_A(q^2)$ is contained in the bilinear forms $A(q^2)$, $B(q^2)$ and $C(q^2)$ of the nucleon form factors F_1, F_2 and G_A itself. The latter is assumed to be the only unknown quantity, parameterised empirically in terms of an 'axial mass' M_A (or, equivalently, in terms of an 'axial radius' $r_A \equiv \sqrt{12}/M_A$) as

$$G_A(q^2) = \frac{g_A(q^2)}{g_A(0)} \simeq \frac{1}{(1-q^2/M_A^2)^2}\,, \tag{1.1}$$

where $g_A(0) = 1.2670 \pm 0.0035$ [25] is the axial coupling constant. Figure 1.1 shows the available supply of values for M_A obtained from these studies. References [17, 19, 20, 23] reported severe uncertainties in either knowledge of the incident neutrino flux or reliability of the theoretical input needed to subtract the background from genuine elastic events (both of which gradually improved in subsequent experiments). Their reported values fall well outside the range of values known today and exhibit very large statistical and systematical errors. Following the data selection criteria of the PDG ([24], p. 9) they were excluded from this compilation.

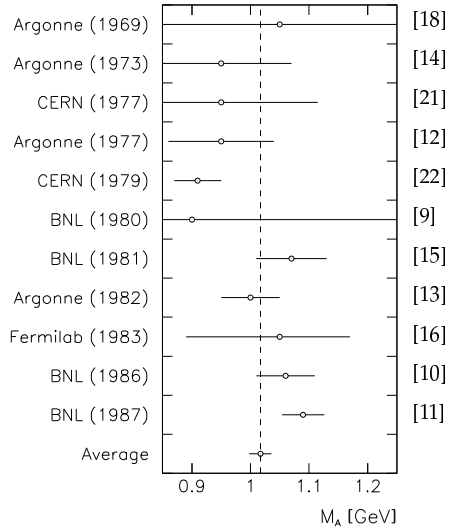

Figure 1.1: The axial mass M_A as extracted from quasi-elastic neutrino and anti-neutrino scattering experiments (the references for the individual data points are given on the right). The weighted average with statistical and systematical errors (if they have been specified separately) added in quadrature is $M_A = (1.017 \pm 0.019)\,\mathrm{GeV}$, or $(1.017 \pm 0.023)\,\mathrm{GeV}$ using the scaled-error averaging recommended by [24].

[1] A brief description of the formalism underlying the extraction of G_A from (anti)neutrino-nucleon scattering is given in Appendix A.

Another body of data comes from charged pion electro-production on protons [26, 27, 28, 29, 30, 31, 32, 33, 34, 35] not far above the pion production threshold. As opposed to neutrino scattering studies which can be covered by the basic Cabibbo theory, extracting the axial form factors from electron scattering measurements requires a more profound theoretical picture of the process, involving specific models of the nucleon structure; the situation is reviewed in chapter 5. The results of various approaches are shown in figure 1.2. Note again that references [36, 37] were omitted from the fit for lack of reasonable compatibility with other results.

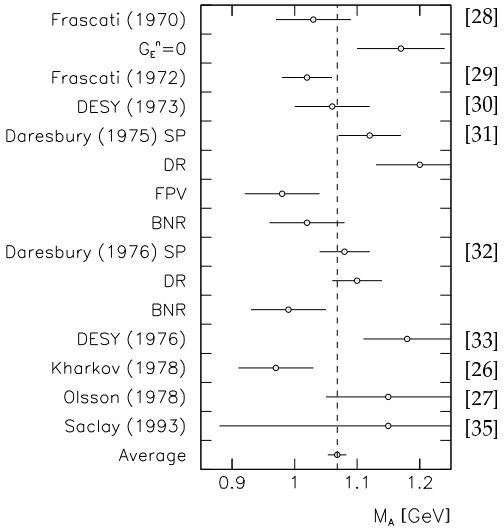

Figure 1.2: The axial mass M_A as extracted from charged pion electro-production experiments (the references for the individual data points are given on the right). The weighted average with statistical and systematical errors added in quadrature (if they have been specified separately) is $M_A = (1.068 \pm 0.015)\,\mathrm{GeV}$, or $(1.068 \pm 0.017)\,\mathrm{GeV}$ using the scaled-error averaging recommended by [24].

Although the results of the individual axial form factor determinations deviate substantially from one another, there seems to be a significant difference of $\Delta M_A = (0.051 \pm 0.024)\,\mathrm{GeV}$ between the neutrino and electron scattering weighted averages. But it seems obvious from figures 1.1 and 1.2 that at least in the older experiments the systematical errors were grossly underestimated and that the $\pm 0.024\,\mathrm{GeV}$ deviation of ΔM_A is too small. The scaled-error weighted averaging of the PDG gives a larger deviation of $\pm 0.028\,\mathrm{GeV}$. Similarly, making an 'iterative' weighted average of the uncertainties by using the deviations of individual values of M_A from the calculated weighted mean, we obtain $M_A = (1.017 \pm 0.029)\,\mathrm{GeV}$ from neutrino scattering experiments. From electron scattering experiments, we get $M_A = (1.068 \pm 0.023)\,\mathrm{GeV}$, and so the difference is $\Delta M_A = (0.051 \pm 0.037)\,\mathrm{GeV}$.

This 'axial mass discrepancy' and its inconclusive uncertainty were in the focus of our investigation of the reaction $p(e, e'\pi^+)n$, and one of our principal aims was to perform a measurement accurate enough to show whether the discrepancy is genuine and, according to the result, to either make a claim in favour or against the $\mathcal{O}(q^2)$ prediction of χPT for ΔM_A. The meaning and possible physical background of this discrepancy are discussed in section 2.2 (and later in section 5.3), and the pion electro-production formalism is reviewed at the beginning of chapter 2.

The experimental part of this thesis deals with the $p(e, e'\pi^+)n$ coincidence experiment performed by the A1 Collaboration at the Institute for Nuclear Physics, University of Mainz. In this experiment, our intention was the extraction of the q^2-dependence of the nucleon axial form factor by means of an effective Lagrangian model [38] based on the formalism of [40, 41]

and [42]. The measurement was performed at the invariant mass of $W = 1125\,\mathrm{MeV}$ and at virtual photon four-momentum transfers q^2 of -3, -5 and $-7\,\mathrm{fm}^{-2}$, in order to be able to perform a q^2-fit of the model calculation to the data.

The experimental equipment used in the experiment (the electron accelerator, the cryogenic liquid hydrogen target, the magnetic spectrometers and the detector systems) is described in chapter 3. Chapter 4. is entirely devoted to the data analysis. Several cuts and correction factors were applied to the raw experimental data to generate the missing mass spectra containing true coincident events within their peaks. These spectra are normalised to the simulated detector acceptances and the calculated luminosities to yield the reaction cross-sections in each measured setting. For each q^2, the transversal and longitudinal parts are separated from the measured cross-sections by the Rosenbluth technique. The axial form factor and the pion charge form factor can then be extracted from the q^2-dependence of these cross-sections using specific theoretical models, and some of the past attempts using data from inclusive electron scattering and pion electro-production on proton targets are reviewed in chapter 5. Emphasis is finally given to the effective Lagrangian approach used in our own analysis.

A great deal of motivation to study the nucleon axial form factor originates in the 'axial mass discrepancy' described above, but the knowledge of $G_A(q^2)$ can also assist us in finding out its proper theoretical understanding, and in particular of the axial coupling constant $g_A \equiv g_A(0)$. Chapter 6. therefore starts with a historically annotated formal introduction to the axial coupling constant and reviews some general theoretical concepts and problems. In the second part of the chapter, we calculate $G_A(q^2)$ in the framework of the linear σ-model (characterised by an extraordinary strong pion cloud surrounding the quark core), and the chiral chromodielectric model (which possesses a peculiar QCD-inspired, dynamically generated binding field for quarks), and investigate to what extent the elimination of *spurious centre-of-mass motion* and *recoil effects* improves the agreement of the model calculations with data. Chapter 7. summarises the results of the thesis.

2

General formalism

We can describe all reactions of the $A(e,e'X)B$ kind in which the scattered electron is detected in coincidence with the ejected particle X (e. g. one nucleon knockout reactions or pion electro-production off nucleons), with similar formal tools. This chapter describes the formalism of electron coincidence reactions, based on the assumptions that electrons may be described by plane waves and that a single virtual photon is exchanged between the scattering electron and the hadronic system. This *plane-wave Born approximation*, which is believed to be appropriate for electrons scattering on light nuclei, enables us to separate the physically interesting content of the electro-magnetic interaction in the hadronic vertex from the well known interaction in the electron vertex.

First I display the kinematics of the $p(e,e'\pi^+)n$ reaction. Then I show that a general expression for the differential reaction cross section can be obtained by contracting the leptonic and hadronic tensors, which are bilinear forms of electron and hadron electro-magnetic transition currents. The separation of the transverse and longitudinal parts of the measured differential reaction cross-section was one of the main goals of this thesis, and a commonly used procedure to perform the separation is presented next. At the end of the chapter I try to explain why both experimental and theoretical studies of pion electro-production off nucleons are currently highly physically motivated.

All derivations within this chapter are largely in the spirit of [43, 44]. The conventions of Bjorken and Drell [45] and Drechsel and Tiator [38] are adopted throughout the thesis.

2.1 The expression for the reaction cross-section

If the electro-magnetic process of pion electro-production off nucleons

$$e(p_e) + N(p_i) \to e'(p'_e) + \pi(p_\pi) + N'(p_f)\,,$$

is treated in the plane-wave Born approximation, it can be visualised as shown in figure 2.1, where momentum four-vectors of all the particles involved are listed. The incoming electron in the state $|\,e\,\rangle$ goes to the final state $|\,e'\,\rangle$ whereas the target nucleon $|\,i\,\rangle$ absorbs the virtual photon and becomes $|\,f\,\rangle$. When the virtual photon energy transfer exceeds the pion production threshold, a pion $|\,\pi\,\rangle$ can be emitted from the nucleon. The virtual photon then transfers energy and momentum $q = (\omega, \mathbf{q}) = p_e - p'_e = p_f + p_\pi - p_i$ to the nucleon,

$$\begin{aligned} \omega &= E_e - E'_e = E_f + E_\pi - E_i\,, \\ \mathbf{q} &= \mathbf{p}_e - \mathbf{p}'_e = \mathbf{p}_f + \mathbf{p}_\pi - \mathbf{p}_i\,. \end{aligned}$$

The differential reaction cross-section in the laboratory frame for such a reaction can be written in the standard form [45]

$$d\sigma = \frac{1}{|v_{ei}|}\overline{\sum_{fi}}\frac{m_e^2}{E_e E'_e}\frac{d^3\mathbf{p}'_e}{(2\pi)^3}\frac{M_i}{E_i}\frac{M_f}{E_f}\frac{d^3\mathbf{p}_f}{(2\pi)^3}\frac{1}{2E_\pi}\frac{d^3\mathbf{p}_\pi}{(2\pi)^3}\,|\mathcal{M}_{fi}|^2\,(2\pi)^4\,\delta^{(4)}(p_e + p_i - p'_e - p_f - p_\pi)\,,$$

where $|v_{ei}| = \beta_e = |\mathbf{p}_e|/E_e$ is the relative velocity between the target nucleon and the incoming electron, $|\mathcal{M}_{fi}|^2$ is the (complex) square of the invariant matrix element for the process under consideration, the $\delta^{(4)}$ function expresses overall energy and momentum conservation and where phase spaces of all outgoing particles were taken into account. When neither a polarised incoming electron beam is prepared nor the polarisation of the outgoing particles is measured, the reaction cross-section has to be averaged over the initial and summed over the final electron and nucleon spins, which is denoted by the $\overline{\sum}_{fi}$ symbol.

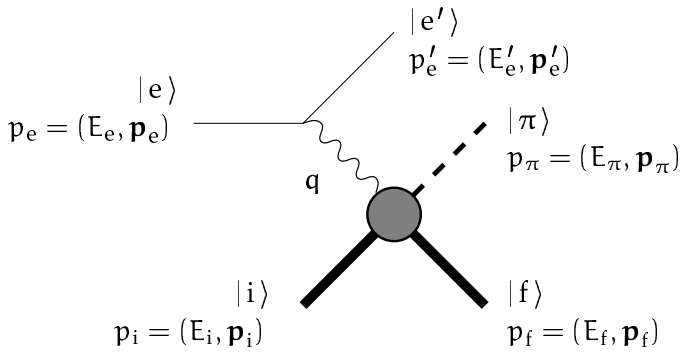

Figure 2.1: The reaction $N(e,e'\pi)N'$ in the plane-wave Born approximation.

In an exclusive reaction like $p(e,e'\pi^+)n$ only the scattered electron and the outgoing pion are measured in the final state. The recoiled neutron is not detected. Integrating the expression for $d\sigma$ first over $\mathbf{p}_f$ and then over $|\mathbf{p}_\pi|$ we eliminate the angular and momentum dependence of the cross-section with respect to the recoiled particle. This integration introduces a *recoil* factor f_{rec} into $d\sigma$, so that

$$\frac{d\sigma}{dE'_e\,d\Omega'_e\,d\Omega_\pi} = \frac{m_e^2 M_n}{(2\pi)^5 2M_p}\frac{|\mathbf{p}'_e||\mathbf{p}_\pi|}{|\mathbf{p}_e|}\frac{1}{f_{rec}}\overline{\sum_{fi}}|\mathcal{M}_{fi}|^2\,,$$

where

$$f_{rec} = \left|1 + \frac{\omega|\mathbf{p}_\pi| - E_\pi|\mathbf{q}|\cos\theta_\pi}{|\mathbf{p}_\pi|M_p}\right|$$

and θ_π is the angle between $\mathbf{q}$ and $\mathbf{p}_\pi$. The coordinate system used to discuss $p(e,e'\pi^+)n$ reaction kinematics is shown in figure 2.2. Momenta of the incoming and of the outgoing electron define the *scattering* plane. The *reaction* plane, tilted with respect to the scattering plane at an angle of ϕ_π, is in turn spanned by the momenta of the virtual photon and the outgoing pion.

To a reasonably good approximation of the pion electro-production process, the electrons interact with the hadronic system by exchanging a single virtual photon. The Lorentz-invariant matrix element $\mathcal{M}_{fi}$ can therefore generally be written as a product of the electron electromagnetic current, the photon propagator, and the hadronic electro-magnetic transition current. In the conventions used we have

$$\mathcal{M}_{fi} = \left[-e\,\overline{u}_e(p'_e, s'_e)\gamma^\mu u_e(p_e, s_e)\right]\frac{-g_{\mu\nu}}{q^2}\left[e\,J^\nu(q)_{fi}\right], \qquad (2.1)$$

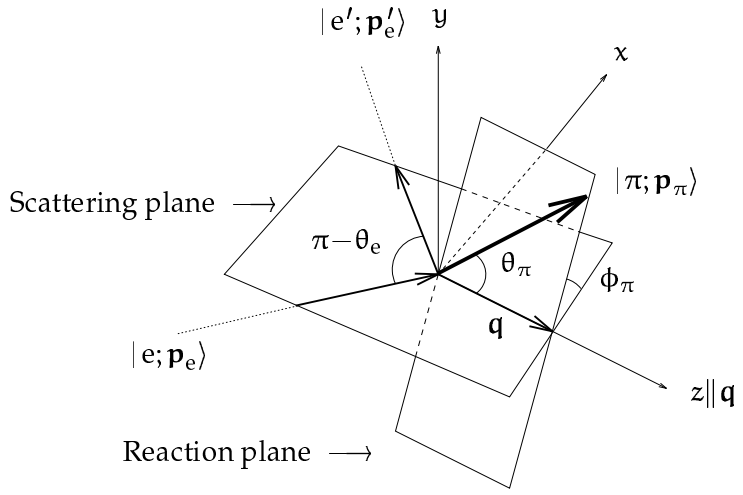

Figure 2.2: The coordinate system used to describe the $p(e,e'\pi^+)n$ reaction.

where u_e are standard Dirac spinors for electrons with four-momenta p_e and spin s_e. Here $J^\nu(q)_{fi}$ is the four-vector of the electro-magnetic transition current for the hadronic system, receiving four-momentum q from the virtual photon (see (B.1)). The square of the invariant matrix element, averaged over initial spins and summed over final spins, is equal to the contraction

$$\overline{\sum_{fi}}|\mathcal{M}_{fi}|^2 = \frac{(4\pi\alpha)^2}{(q^2)^2} L_{\mu\nu}(p'_e,s'_e;p_e,s_e)\, H^{\mu\nu}(q)_{fi}$$

of the leptonic and hadronic tensors

$$\begin{aligned} L_{\mu\nu}(p'_e,s'_e;p_e,s_e) &\equiv \overline{\sum_{fi}} [\,\overline{u}_e(p'_e,s'_e)\gamma_\mu u_e(p_e,s_e)\,]^* [\,\overline{u}_e(p'_e,s'_e)\gamma_\nu u_e(p_e,s_e)\,]\,, \\ H^{\mu\nu}(q)_{fi} &\equiv \overline{\sum_{fi}} J^{\mu*}(q)_{fi} J^\nu(q)_{fi}\,. \end{aligned}$$

The leptonic tensor is exactly calculable in QED. In the case when polarisation of the final electrons is not measured, it is equal to [45]

$$L_{\mu\nu}(p'_e,s'_e;p_e,s_e) = \frac{1}{2m_e^2}\left[p'_{e\mu}p_{e\nu} + p_{e\mu}p'_{e\nu} + \frac{q^2}{2}\,g_{\mu\nu}\right].$$

In this case the differential reaction cross-section in the laboratory system is equal to

$$\frac{d\sigma}{dE'_e\,d\Omega'_e\,d\Omega_\pi} = \frac{\alpha^2 M_n}{16\pi^3 M_p}\frac{|\mathbf{p}'_e||\mathbf{p}_\pi|}{|\mathbf{p}_e|}\frac{1}{(q^2)^2}\frac{1}{f_{rec}}\mathcal{R}_{fi}\,, \tag{2.2}$$

where

$$\mathcal{R}_{fi} \equiv v_0 \sum_\kappa v_\kappa \mathcal{R}^\kappa_{fi}\,,$$

and where we defined $v_0 \equiv (E'_e+E_e)^2 - |\mathbf{q}|^2$. Individual v_κs are called *electronic factors* and the corresponding $\mathcal{R}^\kappa_{fi}$s are the *hadronic structure functions*. The labels κ denote the longitudinal and transverse components of the polarisation of the virtual photon, which in turn correspond to the components of the hadronic transition current with respect to the direction of $\mathbf{q}$. In the

extreme relativistic limit $q^2 = -4E_e E_e' \sin^2 \frac{1}{2}\theta_e$ and $\nu_0 = 4E_e E_e' \cos^2 \frac{1}{2}\theta_e$, and it is instructive to rewrite (2.2) as

$$\frac{d\sigma}{dE_e' \, d\Omega_e' \, d\Omega_\pi} = \left[\frac{\alpha^2 \cos^2 \frac{1}{2}\theta_e}{4E_e^2 \sin^4 \frac{1}{2}\theta_e} \frac{1}{f_{rec}} \right] \frac{|\mathbf{p}_\pi| M_n}{16\pi^3 M_p} \sum_\kappa \nu_\kappa \mathcal{R}_{fi}^\kappa ,$$

where θ_e is the electron scattering angle and the term in brackets is the usual Mott cross-section.

The essential advantage of the factorised notation is that all dependence on the kinematical settings of a chosen measurement is carried by the electronic factors whereas the dynamics and the physical content of the process under consideration are stored in the hadronic structure functions. These are bilinear forms of components of the hadronic current four-vector, which can be directly extracted from an experiment by choosing appropriate kinematical conditions (energy of the incoming and of the outgoing electrons, electron scattering angle). In the case when we are not concerned about spins of the final particles and an unpolarised electron beam is used, only four electronic factors multiplying four corresponding hadronic structure functions enter the formalism. In the laboratory system we then have the electronic factors

$$\begin{aligned}
\nu_T &= -\frac{1}{2}\frac{q^2}{|\mathbf{q}|^2} + \tan^2 \frac{\theta_e}{2} , \\
\nu_L &= \left[\frac{q^2}{|\mathbf{q}|^2} \right]^2 , \\
\nu_{LT} &= \frac{1}{\sqrt{2}} \frac{q^2}{|\mathbf{q}|^2} \left[-\frac{q^2}{|\mathbf{q}|^2} + \tan^2 \frac{\theta_e}{2} \right]^{1/2} , \\
\nu_{TT} &= \frac{1}{2}\frac{q^2}{|\mathbf{q}|^2} ,
\end{aligned}$$

and the corresponding structure functions are

$$\begin{aligned}
\mathcal{R}_{fi}^T &= |J^+(\mathbf{q})_{fi}|^2 + |J^-(\mathbf{q})_{fi}|^2 , \\
\mathcal{R}_{fi}^L &= |\rho(\mathbf{q})_{fi}|^2 , \\
\mathcal{R}_{fi}^{LT} &= -2 \, \mathrm{Re} \, [\rho^*(\mathbf{q})_{fi} (J^+(\mathbf{q})_{fi} - J^-(\mathbf{q})_{fi})] , \\
\mathcal{R}_{fi}^{TT} &= \quad 2 \, \mathrm{Re} \, [J^{+*}(\mathbf{q})_{fi} J^-(\mathbf{q})_{fi}] .
\end{aligned}$$

We have written the components of the hadronic transition current four-vector $J^\mu = (\rho, \mathbf{J})$ in the $(\rho, J^\pm, J^z)$ basis and used current conservation

$$J^z(\mathbf{q})_{fi} = \frac{\omega}{|\mathbf{q}|} \rho(\mathbf{q})_{fi} .$$

In the treatment of pion electro-production we usually do not define hadronic states with respect to the laboratory frame, but with respect to the centre-of-mass system (CMS) of the final hadrons; in our case, this is the system of the ejected pion and the recoiled neutron (from now on, we shall label quantities in the CMS with a *). The transition to the CMS involves a Lorentz boost along $\mathbf{q}$ and it can be shown [44] that this amounts to replacing the energies and momenta in the laboratory frame with their CMS values and to multiplying the electronic factor ν_L by $(W/M_p)^2$ and ν_{LT} by W/M_p. The form of the Lorentz scalars is not affected, although the energy and momentum transfers ω and $\mathbf{q}$ in the laboratory frame are replaced by their CMS counterparts (the polar angle θ_π is also changed to $\theta_\pi^\star$, while the azimuthal angle $\phi_\pi = \phi_\pi^\star$).

In pion electro-production off nucleons we can safely set $M_n = M_p \equiv M$ so that the factors $(M/4\pi W)^2$ and $e^2 = 4\pi\alpha$ can be absorbed in the structure functions. It is also customary to

express all kinematical factors with degrees of transverse and longitudinal polarisation of the virtual photon [6]

$$\varepsilon = \left[1 - \frac{2|\mathbf{q}|^2}{q^2}\tan^2\frac{\theta_e}{2}\right]^{-1},$$
$$\varepsilon_L^\star = -\frac{q^2}{\omega^{\star 2}}\,\varepsilon\,,$$

and to define the *virtual photon flux*

$$\Gamma_v \equiv \frac{\alpha}{2\pi^2}\frac{|\mathbf{p}_e'|}{|\mathbf{p}_e|}\frac{Q_\gamma}{(-q^2)}\frac{1}{1-\varepsilon}\,.$$

It can be understood as the number of virtual photons exchanged between the hadronic system and the electron beam, emitted into the infinitesimal energy interval dE_e' and the solid angle interval $d\Omega_e'$. Here $Q_\gamma = (W^2 - M^2)/2M = WQ_\gamma^\star/M$ is the energy which a *real* photon should have had in order to excite a pion-nucleon final state with an invariant mass of W (the quantity Q_γ is also known as the *equivalent photon energy*). The differential reaction cross-section can then be rewritten in a factorised form in the CMS as

$$\frac{d\sigma}{dE_e'\,d\Omega_e'\,d\Omega_\pi^\star} = \Gamma_v\frac{d\sigma}{d\Omega_\pi^\star}\,. \tag{2.3}$$

The separation of the electronic factors and structure functions differs slightly from (2.2), but its physical content is the same. The response of the hadronic system in the observed process is contained in the differential reaction cross-section

$$\frac{d\sigma}{d\Omega_\pi^\star} = \frac{|\mathbf{p}_\pi^\star|}{Q_\gamma^\star}\left[\frac{W_{xx}+W_{yy}}{2} + \varepsilon_L W_{zz} - \sqrt{2\,\varepsilon_L\,(1+\varepsilon)}\,\mathrm{Re}\,W_{xz} + \varepsilon\,\frac{W_{xx}-W_{yy}}{2}\right]^\star,$$

in which the structure functions still encapsulate the components of physically interesting hadronic currents,

$$W_{\alpha\beta}^\star = e^2\left[\frac{M}{4\pi W}\right]^2 J_\alpha^*(\mathbf{q}^\star)J_\beta(\mathbf{q}^\star)\,.$$

Bilinear combinations $W_{\alpha\beta}$ of hadronic currents carry an implicit angular dependence on the azimuthal angle $\phi_\pi^\star = \phi_\pi$ and on the polar (scattering) angle $\theta_\pi^\star$. For our purposes, it is convenient to write out the ϕ_π-dependence explicitly and to suppress the $\theta_\pi^\star$-dependence for the moment. Let us rename

$$\begin{aligned}
\tfrac{1}{2}(W_{xx}+W_{yy})^\star &\equiv R_T\,,\\
W_{zz}^\star &\equiv R_L\,,\\
-\mathrm{Re}\,W_{xz}^\star &\equiv R_{LT}\cos\phi_\pi\,,\\
\tfrac{1}{2}(W_{xx}-W_{yy})^\star &\equiv R_{TT}\cos 2\phi_\pi\,,
\end{aligned}$$

and $R_\kappa \equiv (Q_\gamma^\star/|\mathbf{p}_\pi^\star|)\,d\sigma_\kappa/d\Omega_\pi^\star$, $\kappa \in \{T, L, LT, TT\}$, so that finally

$$\frac{d\sigma}{d\Omega_\pi^\star} = \frac{d\sigma_T}{d\Omega_\pi^\star} + \varepsilon_L^\star\frac{d\sigma_L}{d\Omega_\pi^\star} + \sqrt{2\,\varepsilon_L^\star(1+\varepsilon)}\,\frac{d\sigma_{LT}}{d\Omega_\pi^\star}\cos\phi_\pi + \varepsilon\frac{d\sigma_{TT}}{d\Omega_\pi^\star}\cos 2\phi_\pi\,. \tag{2.4}$$

2.2 Motivation for the separation of the structure functions and extraction of G_A

It is shown in appendix B, where the structure functions are expanded in terms of the electro-production multipole amplitudes and of the pion scattering angle $\theta^\star_\pi$, that in the first order of the multipole expansion $d\sigma_{LT}/d\Omega^\star_\pi \sim \sin\theta^\star_\pi$ and $d\sigma_{TT}/d\Omega^\star_\pi \sim \sin^2\theta^\star_\pi$. This means that a measurement in *parallel* kinematics, in which the centre of the hadronic spectrometer's acceptance is aligned with $\mathbf{q}$ ($\sin\theta^\star_\pi = 0$) enables us to disentangle the linear combination

$$\left.\frac{d\sigma_v}{d\Omega^\star_\pi}\right|_{\theta^\star_\pi=0} = \frac{d\sigma_T}{d\Omega^\star_\pi} + \varepsilon^\star_L \frac{d\sigma_L}{d\Omega^\star_\pi} \tag{2.5}$$

from the measured cross-section, whereas the two interference cross sections vanish. At chosen energy and momentum transfers ω and $|\mathbf{q}|$, the transversal and longitudinal cross sections can be separated by measurements at different values of $\varepsilon^\star_L$ by means of a straight-line fit.

The L/T separation of the electro-production cross-sections closely resembles the 'classical' Rosenbluth separation in inclusive electron scattering experiments $N(e,e')N$. In order to increase the accuracy of the separation, the $\varepsilon^\star_L$ has to span a lever arm as large as possible. But usually the range of its values is kinematically constrained by the mutual placement of the electron and the hadron spectrometer and by the maximal energy of the electron beam. Large values of $\varepsilon^\star_L$ correspond to smaller electron scattering angles, which are usually difficult to achieve experimentally due to the proximity of the exit beam pipe. On the other hand, small values of $\varepsilon^\star_L$ can be reached at large scattering angles, where the virtual photon flux Γ_v strongly decreases [2]. Especially in the early days of low duty-factor accelerators and detectors of moderate performance, results from electron coincidence experiments therefore suffered from large statistical and systematical uncertainties.

In spite of that, numerous measurements of charged pion electro-production were performed already in the 1960s and 1970s at the accelerator facilities in Hamburg, Daresbury, Frascati and Saclay: total or inclusive cross-section for $p(e,e')p$ in the region of the Δ resonance [46, 47, 48]; total cross-section for $p(e,e')p$ in the vicinity of the pion production threshold [26, 28, 29, 37] and in the Δ resonance region Δ [49]; the differential reaction cross-section for $p(e,e'p)\pi^0$ [50, 51, 52, 53, 54, 55, 56, 57] and $p(e,e'\pi^+)n$ [51, 58] near the Δ resonance; and the differential reaction cross-section for $p(e,e'\pi^+)n$ close to threshold [5, 30, 59, 60].

All these experiments, exclusively employing proton targets, were mostly aimed at measurements of angular distributions of the recoiled protons. Although electron accelerators with high peak beam intensities were used, coincidence measurements were strongly impaired by sudden particle bursts in the detectors due to the accelerators' pulsed mode of operation. In addition, experimental requirements in pion electro-production are not the same as in $(e,e'p)$ reactions: for example, to discern among $\pi^\pm$ and $e^\pm$, one needs highly efficient Čerenkov detectors in both spectrometer arms. Poor statistics practically did not allow the separation of electro-production cross-sections. For these reasons, pion electro-production experiments were completely halted after 1978. Figure 2.3, containing all available data on transverse and longitudinal cross-sections for $p(e,e'\pi^+)n$ to that time, shows a notable exception of [5] (and, conditionally, of [60]).

[2] The magnetic spectrometers used to detect and analyse the particles emerging from a coincidence reaction possess only finite momentum and angular acceptances. Although it is of no significance to the 'point-wise' L/T separation described here, one has to be aware that the extracted cross-sections are therefore implicitly averaged over certain kinematical variables, e. g. over dispersive and non-dispersive angles. If one wants to avoid this by narrowing the acceptances, one either needs to increase the total measurement time or cope with larger statistical errors.

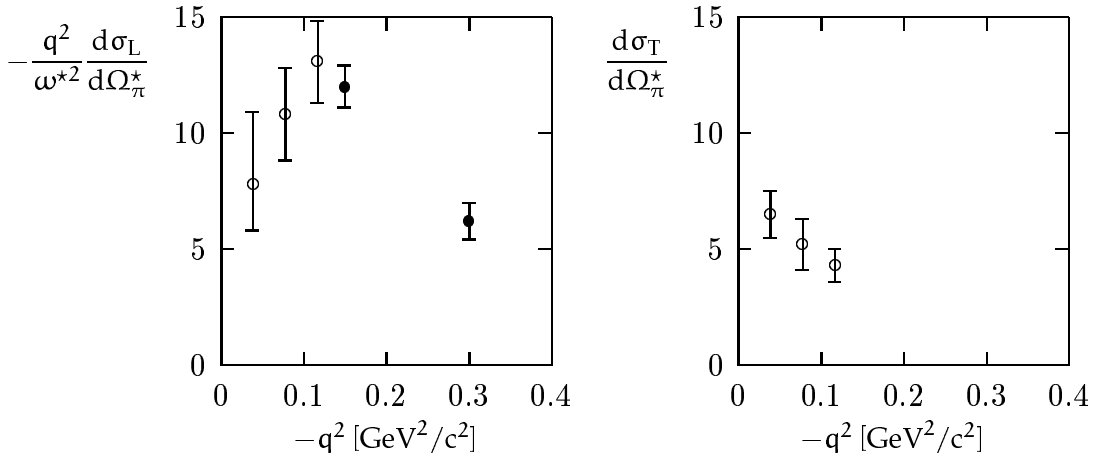

Figure 2.3: Longitudinal and transverse cross-sections $d\sigma_L/d\Omega_\pi^\star$ and $d\sigma_T/d\Omega_\pi^\star$, extracted from two $p(e,e'\pi^+)n$ coincidence experiments performed before 1978: ∘ [5], • [60] (for the latter, the $d\sigma_L$ was determined by assuming a fixed calculated value of $d\sigma_T$). Both measurements were done in parallel kinematics ($\theta_\pi^\star = 0$) with $W = 1175$ MeV. The cross-sections are in units of μb/sr.

With modern, high duty-factor electron accelerators and with new, large-acceptance and high-resolution magnetic spectrometers, coincidence electro-production experiments were reborn. In particular, coincidence pion electro-production experiments on the proton newly became interesting and feasible. For example, the interest in the L/T separation in charged pion electro-production was revived by the fact that in the charged channel, $e + p \to e' + n + \pi^+$, the transverse cross-section close to threshold is dominated by the electric dipole amplitude $\sqrt{2}(E_{0+}^{(0)} + E_{0+}^{(-)})$ (see appendix B and appendix C for its definition), which can be directly related to the axial coupling constant $g_A \equiv g_A(0)$ and to the axial form factor $G_A(q^2) \equiv g_A(q^2)/g_A(0)$ of the nucleon.

Although the axial-vector coupling constant appears to be a textbook topic, its experimental value seems to have been stabilised only recently. In fact, as pointed out by [64], the value of the axial coupling 'constant' increased for as much as 7 % since the early measurements in 1959, until the modern measurements in which the total relative experimental errors do not even exceed 0.5 % [65, 66, 67, 68, 69]. The issue at stake is non-trivial since pinning down the precise value of $g_A(0)$ also enables us to give a better estimate of the validity of the Goldberger-Treiman relation [61]

$$M g_A(0) = f_\pi g_{\pi NN}(0) \tag{2.6}$$

where $g_{\pi NN}(0)$ is the pion-nucleon coupling constant and $f_\pi = 92.4$ MeV is the pion decay constant ([25], p. 353.) The Goldberger-Treiman relation is mandated by the chiral symmetry of QCD and is generally believed to hold to a level better than 10 %. Since the $g_{\pi NN}$ in (2.6) should be evaluated at zero momentum transfer (which is unphysical), it is more appropriate to examine the Goldberger-Treiman *discrepancy*

$$\Delta_\pi = 1 - \frac{M g_A(0)}{f_\pi g_{\pi NN}(m_\pi^2)} = 1 - \frac{g_{\pi NN}(0)}{g_{\pi NN}(m_\pi^2)}\,. \tag{2.7}$$

Unfortunately, the chiral perturbation theory does not predict Δ_π. At the $\mathcal{O}(p^2)$ of the general πN Lagrangian, (2.6) remains exact; but even at the $\mathcal{O}(p^3)$, pion loops do not modify the $\mathcal{O}(p^2)$ expression and the value of Δ_π is essentially an input to the theory [62]. However, the Dashen-Weinstein theorem [63] relates Δ_π to the discrepancies defined analogously for the

$\Sigma \to N e \nu$ and $\Lambda \to N e \nu$ processes. It can be expressed as a 'sum rule'

$$\Delta_\pi = \frac{\sqrt{3}}{2}\frac{f_K}{f_\pi}\frac{m_u + m_d}{m_u + m_s}\left[\frac{g_{\Lambda KN}}{g_{\pi NN}}\Delta_K^\Lambda - \frac{1}{\sqrt{6}}\frac{g_{\Sigma KN}}{g_{\pi NN}}\Delta_K^\Sigma\right],$$

where

$$\Delta_K^\Lambda = 1 - \frac{(M - m_\Lambda)g_A^\Lambda(0)}{\sqrt{2}f_K g_{\Lambda KN}(m_K^2)} = 0.32\,,$$
$$\Delta_K^\Sigma = 1 - \frac{(M - m_\Sigma)g_A^\Sigma(0)}{\sqrt{2}f_K g_{\Sigma KN}(m_K^2)} = -0.05\,,$$

and where $g_{\Lambda KN}(m_K^2) = -13.5$, $g_{\Sigma KN}(m_K^2) = 4.3$, $g_A^\Lambda(0) = -0.72$ and $g_A^\Sigma(0) = 0.34$ as quoted in [64]. Further consideration depends on the value of $g_{\pi NN}(m_\pi^2)$. With the 'traditional' value of 13.4 [70], we get $\Delta_\pi = 0.041$ or $m_s/(m_u + m_d) \simeq 48$, whereas with the new value of 13.05 [71], we obtain $\Delta_\pi = 0.015$ or $m_s/(m_u + m_d) \simeq 17$. The latter result strongly favours the conventional χPT picture predicting $2m_s/(m_u + m_d) = 25$ to the generalised version predicting $2m_s/(m_u + m_d) < 25$. This is where the value of $g_A(0)$ comes into play: the smaller value of $g_{\pi NN}(m_\pi^2)$ and the current average experimental value of $g_A(0) = 1.2670 \pm 0.0035$ [25], hint at a validity of (2.6) to a level of $\simeq 1\,\%$, which is much smaller than the usually quoted $10\,\%$.

Similar historical developments could be observed in the understanding of the axial-vector form factor of the nucleon (see chapter 6. for a review). In the past few decades, its q^2-dependence emerged from a lively interplay between new experiments and theoretical models which were initially formulated for photo-production of massless particles. The statements about low energy photo-production of massless charged pions can be traced back to the Kroll-Ruderman result [72]. Considering only conservation of electro-magnetic current, they obtained the threshold electric dipole amplitude in the limit of vanishing pion mass (physically, $m_\pi = \mu M$ with $\mu \simeq 0.15$) and neglecting the terms linear in the photon momentum $|\mathbf{q}|$ ($|\mathbf{q}| \sim \mu$). In this limit, the charged pion photo-production amplitude is fixed by the pion charge

$$E_{0+}^{(-),\,KR} = \frac{e g_{\pi NN}}{8\pi M\,(1+\mu)^{3/2}} \xrightarrow{\mu \to 0} \frac{e g_{\pi NN}}{8\pi M}\,, \tag{2.8}$$

and correspondingly vanishes in the case of neutral pion photo-production. The theorem was subsequently extended to virtual photons by Nambu, Lurié and Shrauner [73, 74], who obtained the general result for the isospin $(-)$ threshold electric dipole amplitude

$$E_{0+}^{(-),\,NLS}(m_\pi = 0, q^2) = \left[1 - \frac{q^2}{4M^2}\right]^{1/2} \frac{e g_A}{8\pi f_\pi}\left\{G_A(q^2) + \frac{q^2}{4M^2 - 2q^2}\,G_M^v(q^2)\right\}, \tag{2.9}$$

where $G_M^v(q^2)$ is the nucleon isovector magnetic form factor and the Goldberger-Treiman relation has been used to substitute $g_{\pi NN}/M$ by g_A/f_π. Later, improved models were proposed [36, 75, 76, 77, 78, 79, 80, 81], most of them including model-dependent corrections due to the finite pion mass. The values of the axial form factor were determined from the slopes of the integrated differential electro-production cross-sections at threshold, relying on one or more of these models to extract M_A.

But the recent remarkable and *model-independent* result of chiral perturbation theory states that already at $\mathcal{O}(q^2)$, the NLS result of (2.9) has to be updated due to pion loop contributions to the threshold amplitude [82]. Contrary to the case of the Goldberger-Treiman discrepancy, these contributions do not vanish. They effectively reduce the mean-square axial radius

by about 10 % and make M_A *seem* about 5 % larger in electro-production than in neutrino scattering; this difference would then confirm and bridge the gap of $\Delta M_A = 50\,\mathrm{MeV}$ between the electron and neutrino scattering experiments. The aim of this thesis was therefore to investigate whether this gap was genuine and to remove the inconclusive uncertainty of ΔM_A by determining M_A from new, high precision pion electro-production data.

According to the original proposal [83], the reaction $p(e,e'\pi^+)n$ was to be studied at the invariant mass of $W = 1125\,\mathrm{MeV}$ (46 MeV above the pion production threshold), at three values of four-momentum transfer $q^2 = -1\,\mathrm{fm}^{-2}$, $-3\,\mathrm{fm}^{-2}$ and $-5\,\mathrm{fm}^{-2}$, and for each q^2, at three different virtual photon polarisations ε (or ε_L^*), in order to be able to perform the L/T separation of the cross sections. The actually measured kinematical settings are listed in table 2.1.

Data from settings 834, 500 and 219 were presented in [84, 85], and settings 742 and 229 were analysed in [86]. In the present thesis, data from the remaining settings 437, 648, 457 and 259 have been analysed. Thus a set of three cross-sections per single value of q^2 has been obtained, yielding three Rosenbluth-separated cross-sections. This enabled us to study the q^2-dependence of the transverse and longitudinal cross-sections, which are closely related to the q^2-dependence of the axial form factor of the nucleon and to the pion charge form factor, respectively. Since the values of q^2 and W were too high to be able to extract the $E_{0+}^{(-)}$ amplitude safely and to directly apply the χPT result, the cross-sections were analysed in terms of an effective Lagrangian model [38, 85].

Table 2.1: Experimental settings for $p(e,e'\pi^+)n$ at $W = 1125\,\mathrm{MeV}$. Throughout the text, particular settings are referred to by specifying the number following the decimal point in the setting's ε value, e. g. 648 for $\varepsilon = 0.648$. The hall-plane spectrometer angles are counted in the positive sense with respect to the electron beam leaving the target.

Setting (ε)	q^2 [GeV^2/c^2]	E_e [MeV]	E_e' [MeV]	θ_e [°]	θ_π [°]	p_π [MeV/c]
0.834	−0.117	855.11	587.35	−27.93	39.31	188.84
0.500		510.11	242.35	−58.22	28.31	
0.219		405.11	137.36	92.96	−18.41	
0.742	−0.195	855.11	545.79	−37.72	38.27	209.62
0.437		585.11	275.89	66.67	−28.03	
0.229		495.11	185.79	93.45	−20.12	
0.648	−0.273	855.11	504.55	46.83	−35.82	228.00
0.457		690.11	339.55	65.27	−29.37	
0.259		585.11	234.55	89.60	−21.90	

In the theoretical part of the thesis, our motivation is to investigate the axial form factor in the framework of two chiral quark models of the nucleon, the linear σ-model (LSM) and the chromodielectric model (CDM). In the non-perturbative region of QCD, it is currently impossible to study this observable in rigorous QCD calculations, so it is rather treated in a variety of QCD-inspired semi-phenomenological models. The two models we used provide an interesting and natural quark-level description of the statical and dynamical properties of nucleons

and can be viewed as a complement to the hadron-level, power-counting approach of χPT. Often, such models can be applied (or are the only means to study) processes at relatively high momenta of particles and momentum transfers beyond the scope of χPT.

Two important aspects have to be considered when calculating physical observables like g_A or $G_A(q^2)$. Whenever the nucleons are interpreted in terms of three quarks confined to a certain region of space (regardless of whether these couple to mesons or not), one has to deal with the problem of *spurious centre-of-mass motion*. Moreover, when form-factors are calculated and the nucleon is probed by a current, one has to properly correct for the *recoil*. But with the exception of the non-relativistic version of the harmonic oscillator quark model, the centre-of-mass motion can not be explicitly separated from the relative motion of the quarks. Similarly, in the LSM and the CDM we used in our theoretical analysis, the model nucleons emerge as solitons which are neither eigenstates of angular momentum or isospin, nor of linear momentum, and therefore break the rotational and translational invariance of the underlying Lagrangian. This prompted us to explore how these invariances of the LSM and the CDM can be restored in a combined spin/isospin-momentum projection procedure, and to attempt a calculation of $G_A(q^2)$ in which the centre-of-mass motion and recoil effects are eliminated.

3

Experimental setup

In this chapter I present the experimental equipment used in the electron coincidence experiments of the A1 Collaboration at the Institute for Nuclear Physics, University of Mainz. I briefly describe the electron accelerator and the hydrogen target used in the measurements of $p(e, e'\pi^+)n$. Later on, the magnetic spectrometers and their detector packages are described in some more detail.

3.1 The MaMi–B accelerator

In the past, coincidence experiments with electrons were difficult to perform and were burdened with large experimental errors. The reaction cross-sections are low and the efficiencies of the electron accelerators were small. The accelerators were only able to supply bunches of electrons in relatively wide-spaced time intervals (the ratio between the duration of the electron pulse and the time difference between the two consecutive pulses is called the *duty factor* (f_d) of an accelerator). A typical linear accelerator of the old generation was able to supply the peak pulse current of about 5 mA, so that with a duty factor of $f_d \simeq 1\,\%$, an average current of $I_a \simeq 50\,\mu A$ was available at the output, but the electrons were ejected only in short bursts. If these bursts were too intense, massive detector signal pile-ups occurred. An accelerator with a 100 % duty factor, on the other hand, can supply a *constant* beam intensity of $I_a \simeq 50\,\mu A$ so that the detector packages receive a more or less homogeneous load of incoming particles. But the essential advantage of the 100 % duty factor is the improvement of the signal-to-noise ratio: in electron coincidence experiments it is defined as the ratio between the number of true and accidental coincidences [87] (see also the discussion of subsection 4.1)

$$\frac{N_{true}}{N_{acc}} \propto \frac{f_d}{I_a} \tag{3.1}$$

and is proportional to the duty factor and inversely proportional to the average current. That is, at the same average current, a 100 % duty factor accelerator achieves a hundred times higher signal-to-noise ratio than a 1 % duty factor accelerator.

A small length of a linear accelerator is incompatible with a high duty factor. Should the length of the acceleration distance be kept as small as possible, the electric field gradients in the acceleration structures should be as high as possible. But high gradients cause high currents and extensive thermal losses in the microwave resonators' walls so that only pulsed (low duty factor) mode of operation can be realised. To get a continuous electron beam, the resonators have to be fed with constant HF power. This can only be achieved if either the electric field gradients are small or super-conducting resonators are used.

The electron accelerator MaMi–B (Mainzer Mikrotron B) consists of a linear injector accelerator and three consecutive microtrons (partitioning of the accelerator into three consecutive stages is mandated by requirements on the beam quality (focusing)). Acceleration of electrons over unacceptably long distances is avoided by the 'racetrack' mode of operation. In each turn, electrons first gain energy in the acceleration cavities, and are then bent by the two recirculation magnets on the edges of the microtron into the very same series of cavities. Figure 3.1 shows a schematic view of one of the microtron stages. The electrons leave the second microtron stage with an energy of 180.02 MeV and gain an energy of 7.504 MeV per turn in the final, third stage with a maximum of $n_{max} = 90$ recirculations. The final electron beam energy can be parameterised as

$$E_{beam}(n) = (180.02 + 7.504\,n - 3.5 \cdot 10^{-5} n^2 \pm 0.16)\,\text{MeV}\,,$$

where n is the number of turns in the last microtron stage. The maximum electron energy of $E_{beam}(90) = 855.10$ MeV is limited by the strengths of the bending magnets.

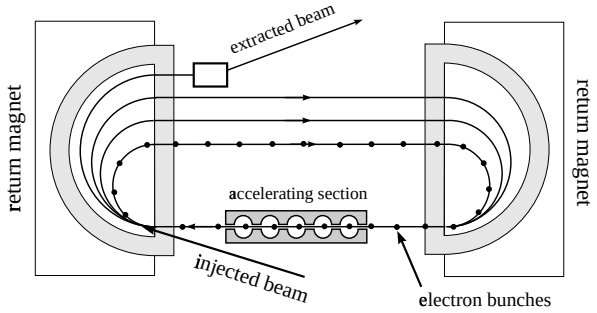

Figure 3.1: One of the three microtron stages of the MaMi–B accelerator.

A deflection system is used to extract the beam from the last microtron and transport it to the experimental hall. The electron beam has a maximum intensity of about 80 μA. Low electric field gradients in the acceleration cavities and klystrons maintain a practically continuous electron beam, which is of paramount importance in low background, high precision coincidence measurements.

3.2 The hydrogen cryo-target and the beam wobbler

To perform a stable measurement of $p(e, e'\pi^+)n$, a reliable cryogenic hydrogen target and its cooling system are needed. They were both designed to withstand high incoming electron beam currents, which could cause local overheating of liquid hydrogen and formation of gas bubbles in the scattering cell.

During the experiment, a Philips-Sterling cooling machine cools and liquefies the hydrogen in the primary circuit with a power of 75 W at a temperature of about 20 K. Along the transfer tube, the liquid hydrogen flows into the scattering chamber and to the secondary heat exchanger (figure 3.2). The actual scattering cell (figure 3.3) lies within the secondary thermal circuit. Two types of cells were used in our experiments: in the settings 834, 500, 219, 742 and 229, we used the cylindrical cell with a diameter of 2 cm and 50 μm thick Havar walls; in all other settings, we used a 4.95 cm long, 1.15 cm wide and 1 cm high scattering cell with vertically circular end caps and 10 μm thick Havar walls [88]. A rotor within the secondary circuit enforces the circulation of the liquid hydrogen to dissipate thermal loads as quickly as possible. Temperature stabilisation is achieved by temperature sensors coupled to heating resistors. The

warmed-up hydrogen from the primary circuit is then transported back to the main cooling machine.

At the same time, the incident electron beam is deflected in mutually perpendicular directions transversely with respect to the beam axis with frequencies of a few kHz and amplitudes of a few mm (figure 3.4). Together with forced circulation, this 'wobbling' of the beam helps us attain higher beam currents and avoid local overheating of hydrogen within the target cell.

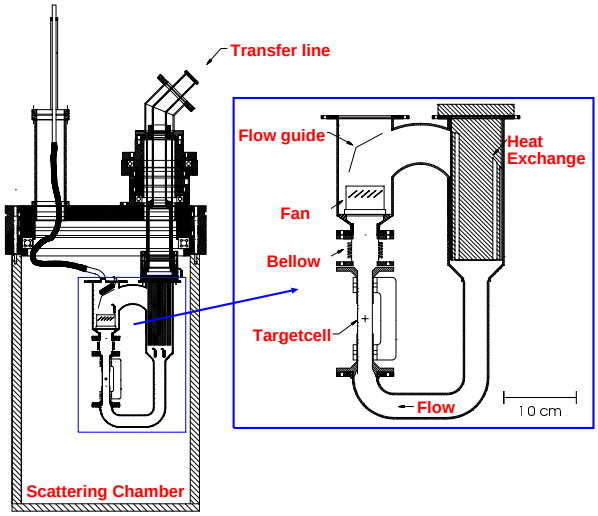

Figure 3.2: Hydrogen cryo-target assembly used in the experiment. The + sign in the zoomed-in figure at the right indicates the central impact point of the electron beam. This point lies on the straight line passing the centre of the target cells shown in figure 3.3.

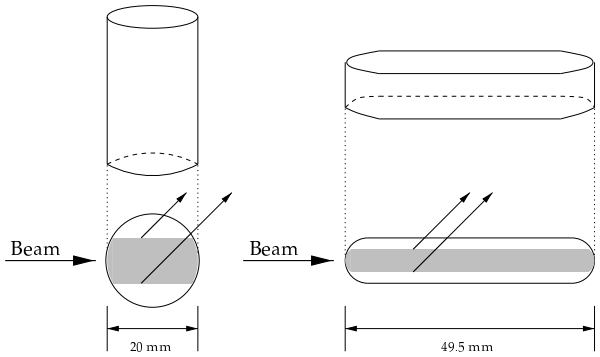

a **b**

Figure 3.3: The target cells used in the $p(e,e'\pi^+)n$ experiments: **a** – the target cell used in kinematical settings 834, 500, 219, 742 and 229, **b** – the improved target cell used in all other settings [88]. The shading indicates the approximate target volume swept by the beam wobbler. Note that the average cell path crossed by the particle is smaller in the cell of type **b** than it is in **a** although its effective thickness is larger for a factor of 49.5/20. This means that in the cell of type **b**, the average energy losses of the outgoing particles, their straggling, and spreading of angular distributions due to the multiple scattering in the hydrogen and the Havar foil, are significantly smaller than in type **a**.

The measurement of the beam current intensity

In our experiment, we used two devices to measure the electron beam current: the Förster probe and the high frequency beam monitor, both suitable for measurements of currents above

$\simeq 10\,\mu A$. Currents of lower intensities could also be measured with a photo-effect beam monitor, but only the former two methods were used in our experiment. See [89] and references [24–27] therein for further details.

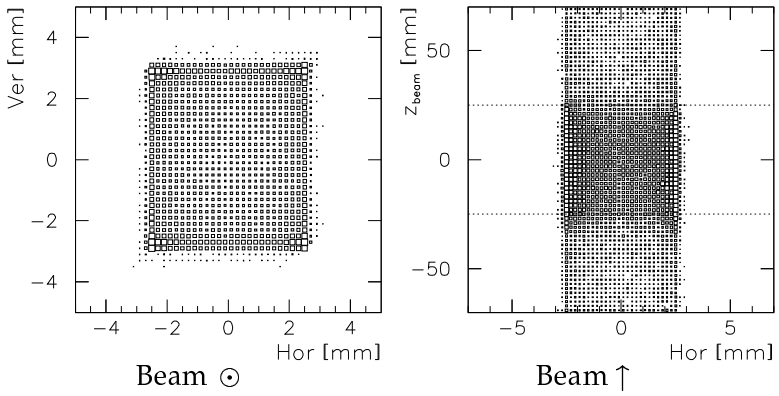

Figure 3.4: Beam wobbler data for kinematics 437: **a** – horizontal and vertical position of the beam on the target cell, **b** – horizontal wobbler position vs. reconstructed vertex along the beam line (physical boundaries of the long hydrogen target are marked by the two dotted lines). The rectangular shape of the inner part of this histogram is a measure for the quality of the wobbler calibration. The entries in the outer part correspond to the background stemming from false reconstruction of the reaction points.

Förster probe

The Förster probe consists of two toroidal coils surrounding the electron beam. The measured quantity is the induced signal in the coils which is proportional to the absolute magnetic field of the electron beam current (and, consequently, to the current itself). The absolute uncertainty of the measurement is $0.3\,\mu A$ for beam currents above $\simeq 10\,\mu A$. Since the probe is installed in the axis of the accelerating section of the third microtron, electron bunches from *all* recirculations contribute to the signal. The absolute precision of the probe is therefore $0.3\,\mu A/n$, where n is the number of the electron beam recirculations. Figure 3.5 shows a sample beam current measurement using the Förster probe.

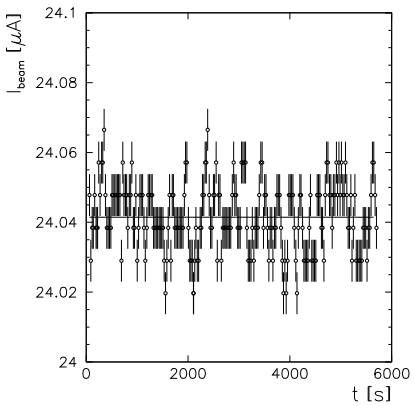

Figure 3.5: A sample measurement of the beam current during an interval of 5700 s using the Förster probe at $E_{beam} = 585\,MeV$. The absolute uncertainties of the individual data points are equal to $0.3\,\mu A/54 \simeq 0.006\,\mu A$. The constant fit to the data gives $\bar{I}_{beam} = 24.04(1 \pm 1.7 \cdot 10^{-5})\,\mu A$ with $\chi^2 = 2.6$.

High frequency beam monitor

This method of the beam current measurement is based on the effect of an electron beam exciting the TM_{010} mode of an EM wave in a HF resonator cavity. The cavity contains an antenna which extracts power from the standing wave; the extracted power is proportional to the square of the electron current and is measured with a power meter with a diode sensing head. The error of the measured signal is $\pm 0.5\,\%$ for beam currents of a few μA and rises to as much as $\pm 3\,\%$ for lower beam currents. Because the resonance curve of the HF cavity is temperature dependent, the cavity must be held at a constant temperature to a level of 1°C using water cooling. To achieve sufficient accuracy, an additional calibration curve describing the temperature dependence of the extracted power must later be implemented in the software. For these drawbacks, the HF measurement was used during our experiment for monitoring purposes, but was not used in the data analysis.

3.3 Magnetic spectrometers and detector systems

Using magnetic spectrometers and built-in detector systems, particles emerging from the target can be analysed with respect to their momenta and identified. Scintillation counters and Čerenkov detectors are used for particle identification and discrimination. The magneto-optical elements (dipole, quadrupole and sextupole magnets) in conjunction with the vertical drift chambers in the focal planes of the magneto-optical systems enable us to determine the momenta and trajectories of the particles. In coincidence experiments of the A1 Collaboration at the Nuclear Physics Institute in Mainz, three such magnetic spectrometers are used [90]. Their basic physical properties are listed in table 3.1.

Table 3.1: Nominal (design) values of parameters of spectrometers A, B and C of the A1 Collaboration. Their magnetic elements are quadrupoles (Q), sextupoles (S) and dipoles (D).

Spectrometer		A	B	C
Configuration		QSDD	D	QSDD
Maximal magnetic field density	[T]	1.51	1.50	1.40
Maximal momentum	[MeV/c]	735	870	551
Reference trajectory momentum	[MeV/c]	630	810	459
Central trajectory momentum	[MeV/c]	660	810	490
Length of the central trajectory	[m]	10.75	12.03	8.53
Target length acceptance	[mm]	50	50	50
Momentum acceptance	[%]	20	15	25
Angular acceptance				
– dispersive plane	[mrad]	± 70	± 70	± 70
– nondispersive plane	[mrad]	± 100	± 20	± 100
– solid angle	[msr]	28	5.6	28
Momentum resolution		$\leq 10^{-4}$	$\leq 10^{-4}$	$\leq 10^{-4}$
Angular resolution on target	[mrad]	≤ 3	≤ 3	≤ 3
Spatial resolution on target	[mm]	3–5	≤ 1	3–5

There are several physical requirements imposed on the spectrometers. In order to keep the measurement times low, spectrometers should have their momentum and angular acceptances as big as possible. High momentum resolution is always desirable, especially in coincidence experiments on nuclei, where closely spaced discrete nuclear states should be distinguished. Good angular resolution is crucial for an accurate reconstruction of the reaction point. For a reliable Rosenbluth separation of the cross-sections in reactions like $p(e,e'\pi^+)n$, we have to measure in as big a range of virtual photon polarisations ε (or $\varepsilon_L^\star$) as possible. To meet this demand, spectrometer B as the (primarily) electron spectrometer can be positioned at small angles with respect to the beam axis. In turn, spectrometers A and C have relatively large angular acceptances and are more suitable for the analysis of hadrons.

Magnets

In spectrometers A, B and C, the charged particles are deflected in the dispersive plane (the magnetic mid-plane of the spectrometer) mainly by the dipole magnets. In magnet optics, positional and angular deviations of a particle's trajectory from a certain reference trajectory are expressed in terms of its spatial coordinates x and y (perpendicular to the reference trajectory), Cartesian angles θ and ϕ and its momentum deviation δ. In first order of the magnet optics, the dipole magnets are the only dispersive elements. Ideally, this means that particles with equal initial coordinates but different momenta will be displaced at the exit of the magnet. On the other hand, trajectories of particles with equal momenta, but different initial angles, will be focused to the same point. In reality, in terms of transfer matrix formalism, the first order matrix elements $(x|x)$ (magnification) and $(x|\delta)$ (dispersion) are large, whereas $(x|\theta)$ is small.

The quadrupole magnets are the first magneto-optical elements following the entrance collimators of spectrometers A and C. They are non-dispersive to the first order, and couple dispersive coordinates x and θ and non-dispersive coordinates y and ϕ through $(x|x)$, $(x|\theta)$, $(\theta|x)$, $(\theta|\theta)$, $(y|y)$, $(y|\phi)$, $(\phi|y)$ and $(\phi|\phi)$ matrix elements, whereas there are no matrix elements involving δ to first order. The quadrupoles are positioned in such a way that particle trajectories are defocused in the dispersive plane and focused in the non-dispersive directions. Thereby, transversal angular acceptance of these spectrometers is significantly increased. If kinematical settings allow us to use them as hadron spectrometers, their high non-dispersive angular acceptance can play a key role in studying angular distributions of the produced hadrons. However, there is a certain trade-off involved in gaining large angular and momentum acceptances: it leads to large angular divergences (as much as $\pm 12^\circ$ with respect to the reference trajectory) of particle rays at the exit of the second dipole. Consequently, the tracking and the time-of-flight detectors positioned close to the focal planes of the spectrometers have to be relatively large.

The nonzero inclination of either the entrance or the exit pole faces with respect to the reference trajectory contributes to dispersive matrix elements involving x and θ. Quadrupole defocusing in the dispersive plane is therefore compensated by the edges of the dipole magnets, inclined with respect to the normal axis of incidence. The inclination angles are such that defocusing in the dispersive plane is minimised, whereas focusing in the non-dispersive direction remains preserved. Additionally, the edges of the dipole magnets are slightly curved, and this curvature introduces additional sextupole strengths. The sextupole magnet between the quadrupole and the first dipole with a curved entrance boundary is used to diminish spherical aberrations in the non-dispersive plane due to second-order $(x|\theta^2)$ and $(x|\phi^2)$ matrix elements.

Spectrometers A and C operate in the point-to-point imaging mode in the dispersive planes ($(x|\theta) = 0$ is necessary for high momentum resolution) and in the parallel-to-point mode in the non-dispersive planes ($(y|y) = 0$ enables high angular resolution). Relatively small spa-

tial (vertex) resolution of spectrometers A and C is compensated for by spectrometer B which operates in the point-to-point imaging mode in both planes, having a very good angular and momentum resolutions, but smaller angular and momentum acceptances (see table 3.1). The magnetic system of spectrometer B is only one dipole ('clam-shell') magnet with inclined and curved edges. Only very slight entrance and exit inclinations and curvatures were necessary to eliminate second- and higher-order aberrations (see [89, 90, 91] for details).

The magnetic field in the interior of the spectrometers is measured with built-in Hall and NMR probes. Each dipole magnet is equipped with one Hall probe and four NMR probes, each covering a certain range of field values from 0.09 to 2.1 T. Since the NMR probes in spectrometers A and C are attached to the inner walls (approximately 60 mm from the spectrometers' magnetic mid-planes), the measured values differ from the values encountered by particles in the vicinity of magnetic mid-planes. Although the corrections to the magnetic field B do not exceed $\approx 2 \cdot 10^{-4}$ T for reference fields below ≈ 1.2 T or $\approx 10^{-3}$ T for fields above ≈ 1.2 T, they were taken into account by gauging the NMR probes in terms of polynomials in B [92].

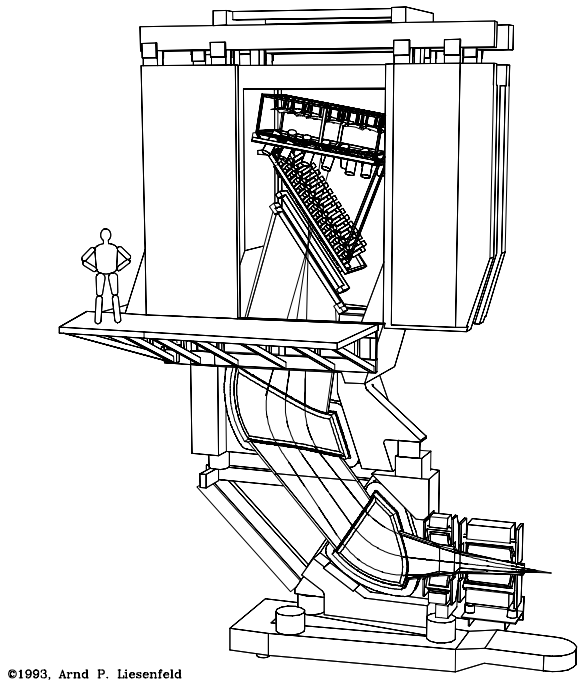

Figure 3.6: The magnetic system and the detector package of spectrometer A (the magnetic system of spectrometer C is basically the same as in spectrometer A, scaled by a factor of 13/17, whereas spectrometer B has only one dipole magnet). All three spectrometers can be rotated around a common point (in the lower right corner of the figure), above which the scattering chamber containing the target cell is installed.

The magnetic field of spectrometer B is too inhomogeneous for the NMR probes to operate (to reach the resonance, the inhomogeneities of the magnetic field density $\delta B/B$ should not exceed the level of $\simeq 2.5 \cdot 10^{-5}$). To overcome this problem, a miniature printed-circuit board quadrupole 'magnet' was placed around the NMR probe with a field gradient opposite to the dipole field gradient, effectively diminishing the local inhomogeneity to less than $\simeq 1 \cdot 10^{-5}$ [92]. The uncertainty of the field measurements with the Hall probes is much higher than the uncertainty of the NMR field measurements, which is in fact smaller than the energy spread $\Delta E/E \approx 2 \cdot 10^{-4}$ of the incoming electron beam [93].

Detectors

When charged particles traverse the spectrometer's magnetic system, they enter the detector packages. In the focal plane of the spectrometers and parallel to it, there are two pairs of vertical drift chambers, followed by two layers of scintillation counters and a Čerenkov detector at the top of the package. Figure 3.6 shows the position of the detector package installed in spectrometer A and figure 3.7 shows the same detector package in some more detail (all figures of the detector systems were made by A. Liesenfeld of the A1 Collaboration).

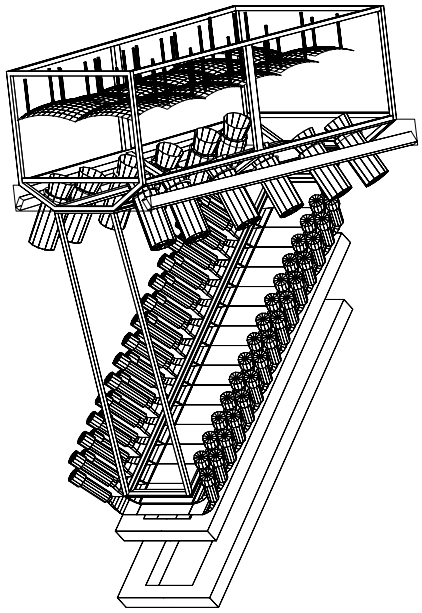

Figure 3.7: The detector system of spectrometer A (the detector system of spectrometer B is qualitatively identical). Particle trajectories are determined by two pairs of vertical drift chambers; particles are identified and distinguished by two segmented scintillation counters and the Čerenkov detector.

Vertical drift chambers

When the particles pass through the magnetic system, they traverse the focal plane. In all three spectrometers, the focal plane is tilted by an angle of about 55° with respect to the horizontal plane, and is traversed by the particles at incidence angles between 33° and 54°. The average useful area of the focal plane is approximately 185 cm × 38 cm in spectrometer A and 190 cm × 11 cm in spectrometer B. Drift chambers installed in the focal plane enable us to reconstruct the particle impact points and directions of their flight. Vertical drift chambers are most suited to this purpose: due to the characteristic configuration of the electric field, electrons from the electron avalanches drift vertically, i. e. perpendicular to the chamber plane.

Vertical drift chambers play a key role in determining the reaction point in the target cell. Four chamber layers, in which sequences of signal wires are rotated relative to one another [91, 94, 95], enable us do determine two points of the trajectory and therefore the particle flight direction. Knowing the imaging properties of the magnetic systems it is then possible to accurately reconstruct the coordinates of the particle and its momentum on target. The resolution design values from table 3.1 can be achieved with spatial resolution of the vertical drift chambers of $\leq 200\,\mu m$ in the dispersive direction and $\leq 400\,\mu m$ in the non-dispersive direction.

Scintillation counters

The scintillation counters and the Čerenkov detectors constitute the triggering system of the magnetic spectrometers. The scintillators are used to identify the particles and to distinguish physically interesting events from the unwanted background (accidental coincidences from concurrent processes, detector noise, cosmic rays and other radiation background). At the same time, scintillation counters are used in all timing tasks: they are used in determination of particles' time of flight from the target to the focal plane and to trigger, time or gate the signals from other components of the detector package and of the data acquisition system. Moreover, high quality of triggering signals from the scintillation counters is crucial for a good coincidence time resolution.

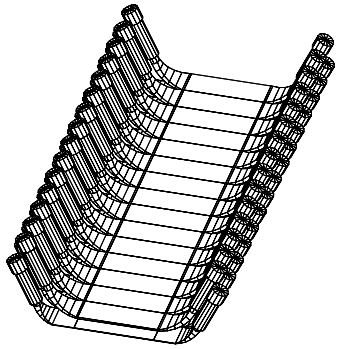

Figure 3.8: Scintillation counters of spectrometer A. The dE layer is used to distinguish protons from minimum ionising particles. The ToF layer is used to measure the time of flight.

The scintillation counter package consists of two layers, as shown in figure 3.8. The first layer (in the particle's flight direction) is the 3 mm thick dE layer, which is used to distinguish protons from minimum ionising electrons, positrons and pions. In this layer, protons generally deposit much more energy than the minimum ionising particles and the two families of particles can later be separated by appropriate cuts in the ADC spectrum. The dE layer is followed by the 10 mm thick ToF layer made of a much faster scintillation material as it is used to measure the time of flight. Both planes are segmented into paddles: light pulses from each paddle are read out by two photo-multipliers attached to the both sides of the paddle. As an exception, the narrower paddles of spectrometer B are read out only on one side. Segmentation of scintillator layers into paddles improves the timing resolution within a large detection volume since path lengths of light in the paddles is shortened.

In our experiment, the scintillation counters together with the coincidence electronics [84] are used to separate positrons and pions from protons. The scintillation counters are not suitable to further distinguish positrons from pions since in our energy range of a few 100 MeV both are minimum ionising. For this purpose, we have to use a Čerenkov detector.

Čerenkov detectors

The Čerenkov detectors are used to distinguish between electrons or positrons and pions. Since in our energy range, all these are minimum ionising particles, scintillation counters are not capable of their discrimination. In magnetic spectrometers of the A1 Collaboration, the Čerenkov detectors are placed behind the scintillator arrays. The active radiator volume is filled with Freon with an index of refraction of about $n = 1.0012$ (figure 3.9).

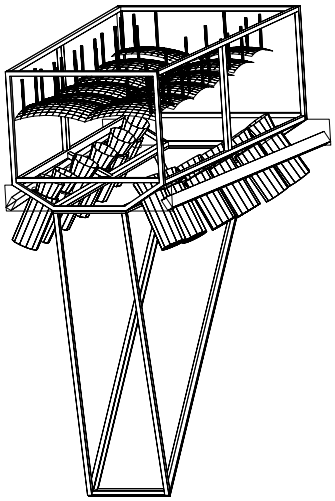

Figure 3.9: Čerenkov detector in spectrometer A. The Čerenkov radiation generated in the radiator gas (the trapezoidal active volume in the lower part of the figure) is gathered by mirrors, mounted at the top of the assembly, and deflected into photo-multipliers at its edges.

The momentum threshold for Čerenkov radiation is about 10 MeV/c for electrons or positrons and 2.4 GeV/c for pions. In our energy range, only electrons or positrons can trigger a Čerenkov signal, whereas the pions can not. Particles with $\beta n \simeq 1$ induce Čerenkov radiation directed predominantly into an angle of $\theta = \arccos 1/\beta n \simeq 0$, i. e. practically along the particle trajectory. Čerenkov light radiated from the active volume is collected by mirrors at the top of the detector assembly, and focused onto photo-cathodes of photo-multipliers at its edges.

To control the operation of the scintillation counters and the Čerenkov detectors, a special laser monitoring system was developed [96]. During the measurement, pulses of laser light can be guided by optical fibres and fed to the scintillator paddles. Incident light pulses simulate the passage of particles through the scintillator layers. These 'pseudo-events' can then be used to monitor individual parts of the detector system and of the coincidence electronics.

3.4 Electronics

After traversing the drift chambers, particles coming from the target first hit the dE scintillator plane and then the ToF plane, and finally reach the Čerenkov detectors. The physical processes in all these detectors lead to signals which constitute a part of the *raw detector data*. It is the duty of the electronic circuitry to read out, convert, convey, process and store these data. The *trigger system* complementing it is responsible for the decision on when (i. e. for which events) these actions should take place. On all three spectrometers, the local logic circuitry is done in an almost identical manner (see figure 3.10 and [84]).

Signals of the individual scintillator and Čerenkov photo-multipliers are first split into two branches. The signals from the first branch are led to the leading-edge discriminators, whereas the signals from the other branch are led via delay lines to the ADCs. These delayed signals arrive at the ADC inputs exactly at the time when the signals of the first branch will have worked their way through the rest of the circuitry and eventually generate an interrupt to trigger the digitalisation process in the ADCs and the readout sequence. On each spectrometer, the signals from the discriminators are given to the left-right coincidence units and then to the spectrometer PLU.

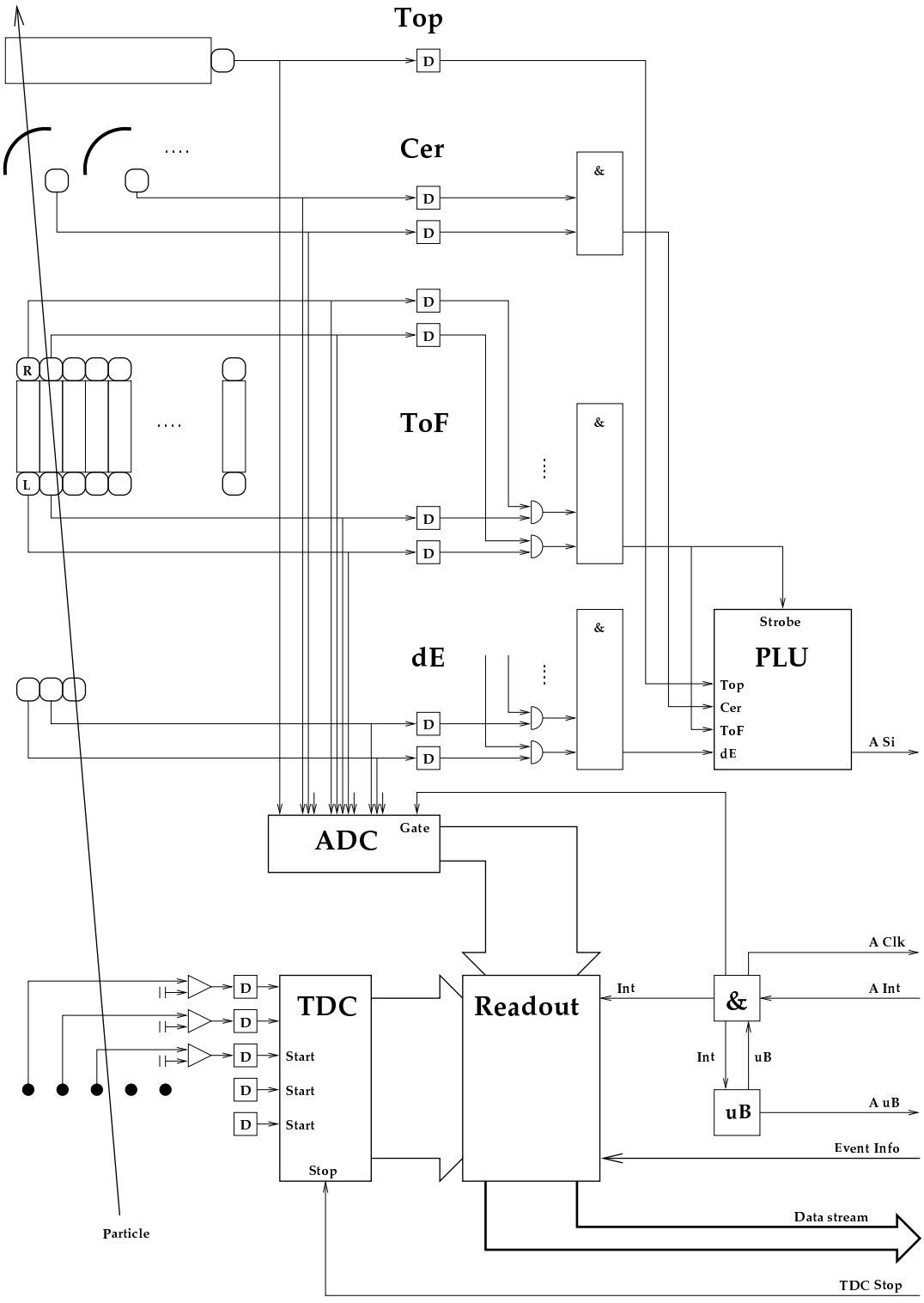

Figure 3.10: Trigger electronics of spectrometer A (similar on spectrometers B and C). A particle is shown traversing the detectors: • – VDC signal wires of all four VDC wire planes, **dE**, **ToF** – scintillator planes, **Cer** – Čerenkov detector, **Top** – top scintillator. The detector signals are handled by: **D** – leading-edge discriminators, **&** – logical units (OR, AND, or programmable gates), **PLU** – Programmable Logical Unit, **uB** – μBusy module, **ADC**s and **TDC**s. Various delay lines are not shown (see text for details).

The basis of the PLU operation is the so-called 'lookup' mechanism. At the time when the strobe signal is provided, the PLU inputs are read out and interpreted as a memory address containing the appropriate output pattern on the output. During this operation, the PLU is insensitive to its input until the unit is cleared by its sync-output. This unambiguous input-output mapping is achieved by preprogramming. In the standard operation mode, the spectrometer PLU is programmed as `de_AND_tof_OR_ch_OR_top`, meaning that coincidences between at least one paddle in the dE and at least one paddle in the ToF layer are required. In this mode, the strobe for the PLU must essentially be defined by ToF and it is critical that the ToF and the strobe signals coincide in time.

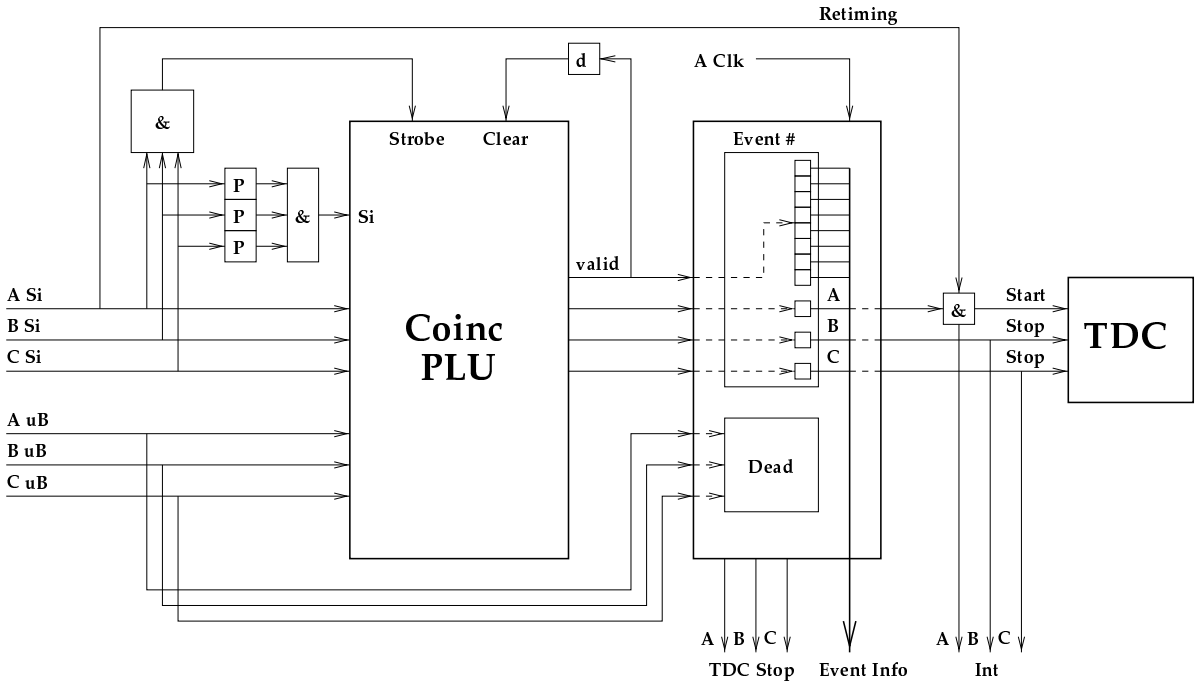

Figure 3.11: Coincidence electronics. The **Coinc PLU** is fed by single-arm signals **A Si**, **B Si** and **C Si** of spectrometers A, B and C (in addition, single-arm signals are prescaled (**P**) on the Coinc PLU input), and by signals **A uB**, **B uB** and **C uB** of µBusy modules from individual spectrometers. The event module synchronised by **A Clk** measures dead time by the **Dead** subunit, triggers A, B and C interrupts, stops the spectrometer TDCs, supplies event info in case of a valid event and starts and stops the coincidence TDC (see text for details).

After the spectrometer PLUs, and in the most general case of triple coincidences, we have three signals leaving the individual spectrometer PLUs: the *not-scaled singles* or shortly singles A, singles B, and singles C. These are led to the coincidence PLU, in addition to the *scaled singles* which first enter the prescalers where they can be optionally scaled down. The coincidence PLU (figure 3.11) also needs a strobe signal defining exactly when the input will be mapped to output. The strobe for the coincidence PLU comes from ORed signals of individual spectrometer PLUs. The timing is adjusted in such a way that Spec B wins if there was a signal from Spec B; as a consequence the timing after the coincidence PLU is determined by Spec B and the signals for Spec A and Spec C need to be *retimed* [3].

[3]Retiming (as an example we consider here only retiming for Spec A) effectively means that the not-scaled singles from Spec A have to be ANDed with the interrupt signal for Spec A. It is crucial for Spec A and Spec C signals to be retimed. In particular, the stop signal for the VDC TDCs started by the discriminated wire signals must originate

The coincidence PLU works the same way as the individual spectrometer PLUs: it uses the lookup mechanism to determine the output from the given state at its input. The output depends on how the coincidence PLU is programmed. The standard programming is `triple_w_double_sc_w_single_sc`, meaning that in general, triple coincidences, (optionally down-scaled) double coincidences and (optionally down-scaled) single events will be processed and passed on.

As soon as the coincidence PLU generates an interrupt (i. e. recognises a valid event), the event counter of the event module is incremented. At the same time, the interrupt signals and the information on the event type are distributed from the master spectrometer to slave event modules on other spectrometers involved. These interrupts actually trigger the readout process. Next, the µBusy flip-flops on the spectrometers are set; this halts further data taking while the electronics is busy. On each spectrometer involved, the interrupt signal also generates a gate for the detector ADCs and starts the ADC timer. The photo-multiplier signals from the detectors that were hit by the traversing particles, have exactly reached the ADC inputs by now, after being appropriately delayed (see above). Within the time gate opened by the interrupt, these signals are integrated and the digitised values are fed into the data stream. Similarly, the TDCs of the VDCs that were started by the discriminated signals from the signal wires, are stopped by the retimed spectrometer interrupt. In addition, there are TDCs that measure the time of flight from the dE to the ToF plane and from ToF to the Čerenkov detector, and these are also started and stopped analogously. Only when all these tasks are properly done and data acquired, the spectrometer µBusy flip-flop is reset, thereby unlocking the coincidence PLU, and further data taking is allowed.

exactly from the photo-multiplier signal belonging to the corresponding scintillator paddle. To this purpose, the Spec A and Spec C interrupts are not directly applicable; they *must* be retimed.

4

Data analysis

In this chapter I review the analysis of the data for $p(e,e'\pi^+)n$, measured at the invariant mass of $W = 1125\,\mathrm{MeV}$, at virtual photon four-momentum transfers of $q^2 = -5\,\mathrm{fm}^{-2}$ and $-7\,\mathrm{fm}^{-2}$. The data analysis effectively amounts to deducing physically relevant information pertaining to the interaction point (like particles' momenta or emission angles) from the raw data (e. g. wire chamber drift times, scintillator detector hit patterns and signal levels, and Čerenkov detector signals). From the particles' momenta, further physically relevant spectra (e. g. the missing mass or the neutron recoil energy) can be generated and used for particle identification and background reduction.

4.1 Coincidence time

The timing of a double-arm coincidence experiment employs the discriminated photo-multiplier signals of the spectrometers' scintillator detectors. The primary means used to isolate true coincident events from the data is the *coincidence time spectrum*, which should essentially contain the differences between the times of flight of the associated particles through the first and the second spectrometer. This time difference is digitised by the coincidence TDC module, which is started by one of the spectrometers and stopped by the other. In our experiment, spectrometer A was always used to start and spectrometer B to stop the TDC and the temporal sequence of the timing signals can be viewed on as in figure 4.1.

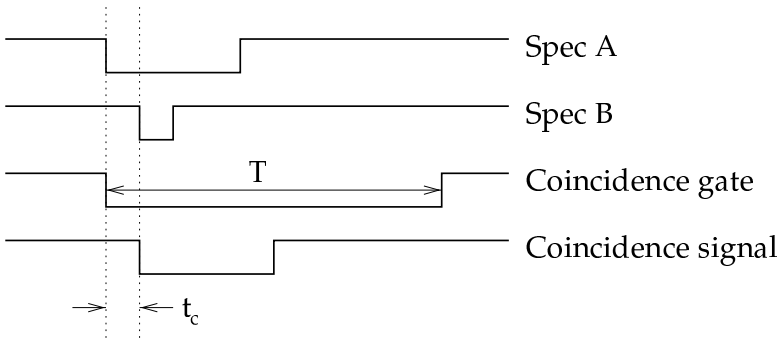

Figure 4.1: The temporal sequence of the timing signals from spectrometers A and B. The signal from spectrometer A opens the coincidence gate of width T; all signals from spectrometer B arriving within this interval (say, after t_c) trigger a coincidence signal. The value of t_c is then digitised by the TDC module.

Ideally, the difference between the time of flight of an electron through one spectrometer and the time of flight of a pion through the other spectrometer, both coming from the *same* reaction $p(e, e'\pi^+)n$, should be constant for all events. However, due to particle momentum dependence of the time of flight, there are certain deviations from a constant difference. Nevertheless, a genuine coincident pion should trigger a signal with a fixed time relation to the signal triggered by the corresponding electron, whereas an uncorrelated pion and electron should not have any particular signature. In practice, the histogram of all events in t_c (the coincidence time spectrum) therefore exhibits a peak at a certain average value of t_c corresponding to true coincidences and a continuous background of accidental coincidences, spanning the whole width of the coincidence gate. The observed width of the background of accidental coincidences is equal to the width of the coincidence gate T. For purposes of our experiment, it was set to $T = 80$ ns in order to accommodate a broad range of pions' times of flight.

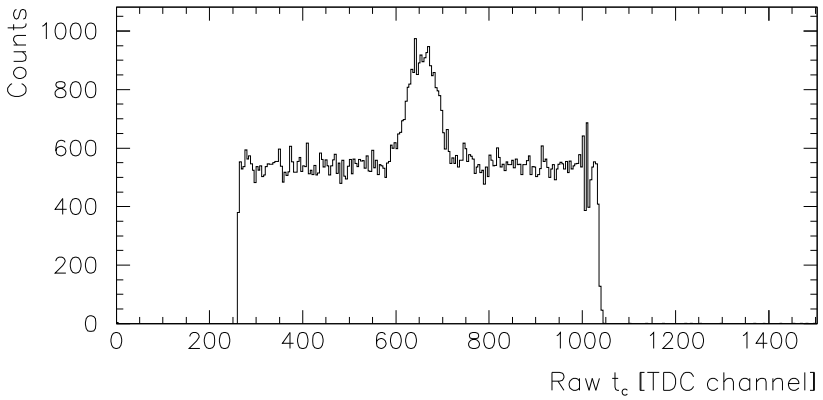

Figure 4.2: The raw coincidence time TDC spectrum for kinematics 437. One channel corresponds to 100 ps. The covered range is equal to the width of the coincidence gate, i. e. about 80 ns, and the FWHM of the peak is 6.5 ns.

The *raw* coincidence time spectrum in figure 4.2 is an accumulation of raw coincidence signals and has a large width. The observed width is mainly due to different velocities and different path lengths (and therefore varying times of flight) of particles from the target to the ToF scintillator layers. In the case of spectrometer A, for example, the path length differences can be as high as ± 1.5 m with respect to the central trajectory. The raw time peak is additionally smeared because of the processes in the scintillators (time required by light travelling from the particle impact point towards the photo-cathodes of the photo-multipliers, intrinsic resolution of the photo-multipliers) and in the detector electronics (modules, cables and delays). The broadening of the coincidence peak can be reduced by software corrections. Since the optical properties of the spectrometers are well known [91] and since the VDCs provide enough information to reconstruct the particle trajectories, the path length differences relative to the central trajectories and the corresponding 'correction' to the coincidence time can be calculated. In addition, the particle's point of impact in the scintillator paddle can be determined and corrected for.

The correction of the coincidence time due to different path lengths has an astonishing influence on the width of the coincidence peak. The effect can be demonstrated by comparing two dimensional spectra of the dispersive coordinate x in the spectrometer focal plane vs. the coincidence time without and with the time of flight correction (figure 4.3 for (228 ± 17) MeV/c pions in spectrometer B). Pions with the highest momenta reach the upper edge of the focal plane ($x \to 1000$ mm) as much as 14 ns later than the pions with the lowest momenta reaching

the lower edge ($x \to -1000\,\mathrm{mm}$). By correcting for this difference, we make the pions 'seem' as if they all passed the focal plane at almost equal times (note that such a correction also has to be done in the electron arm of the setup).

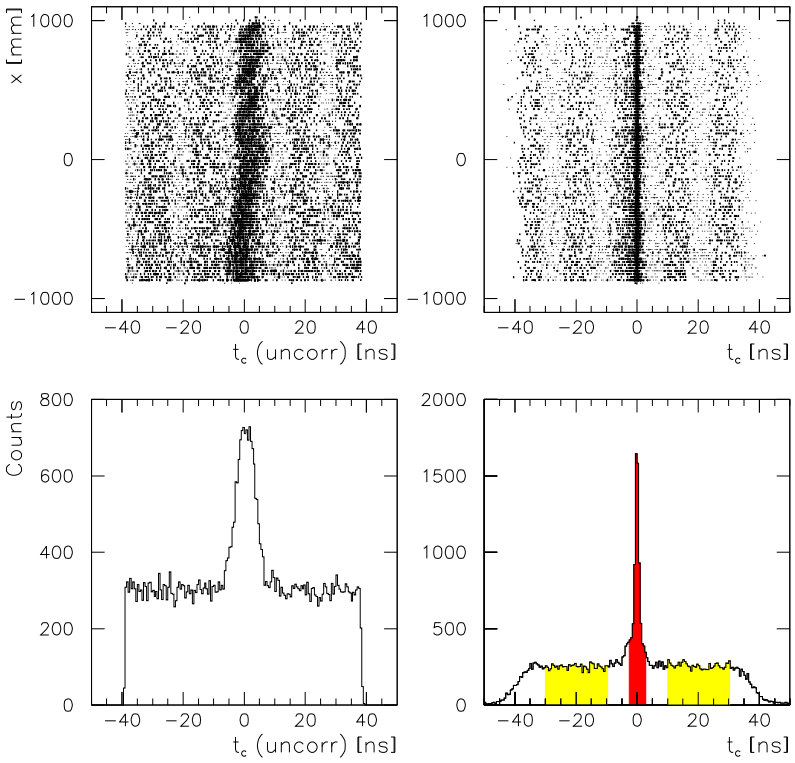

a1 a2
b1 b2

Figure 4.3: Correlation between the coincidence time and the dispersive coordinate x in the focal plane of spectrometer B in kinematics 437: **a1** – without and **a2** – with the path length difference correction. The FWHM of the corrected coincidence peak is 1.6 ns (**b2**) compared to the uncorrected width of 6.5 ns (**b1**). Note that the individual paddle time offsets were already accounted for.

It is imperative to correct the coincidence time spectrum for all described effects and thereby optimise the coincidence time resolution. Namely, as stressed in (3.1), it is necessary to keep the ratio between the true and accidental coincidences as high as possible, especially in coincidence experiments with small reaction cross-sections. Otherwise, the coincidence peak can be masked by the accidental background and the examined reaction can not be reliably isolated. As it will be shown in section 4.2, a cut in the coincidence time spectrum enables us to make a sharp separation between the true coincidences and background events.

4.2 Missing mass

Another means of identifying true coincident events and distinguishing them from accidental coincidences is the *missing energy* or the *missing mass* spectrum. In nuclear reactions of the $A(e,e'p)A-1$ type, the missing energy is defined as the energy which can not be directly measured in the coincidence experiment and is therefore "missing" in the overall energy balance. The energy and momentum conservation $E_e + E_A = E'_e + E_p + E_{A-1}$ and $\mathbf{p}_e + \mathbf{p}_A = \mathbf{p}'_e + \mathbf{p}_p + \mathbf{p}_{A-1}$ for such a reaction express that

$$E_m = E_e - E'_e - T_p - T_{A-1}\,.$$

The kinetic energy $T_p = (\mathbf{p}_p^2 + M^2)^{1/2} - M$ of the knocked-out proton is known, since we directly measure its momentum $\mathbf{p}_p$, whereas the kinetic energy of the residual nucleus with momentum $\mathbf{p}_{A-1} = \mathbf{q} - \mathbf{p}_p$ can be indirectly "measured" by

$$T_{A-1} = ((\mathbf{q} - \mathbf{p}_p)^2 + M_{A-1}^2)^{1/2} - M_{A-1} \, .$$

This description is very illustrative in the case of one proton knock-out reactions where E_m is also equal to the difference between the binding energies of the residual and the target nucleus, and equal to the sum of the separation energy of the proton in the target nucleus and the excitation energy of the residual nucleus. But in an $A(e,e'p)A-1$ process, the proton is already in the nucleus just before the knock-out, whereas in $p(e,e'\pi^+)n$, the pion may have first to be formed, and the description is not as transparent, so we defined E_m and $\mathbf{p}_m$ as the corresponding neutron quantities

$$\begin{aligned} E_m &= E_e - E_e' + M_p - E_\pi = E_n \, , \\ \mathbf{p}_m &= \mathbf{q} - \mathbf{p}_\pi = \mathbf{p}_n \, . \end{aligned}$$

In our data analysis, we therefore used an event-by-event reconstruction of the four-vectors $(E_m, \mathbf{p}_m) = (\omega + M_p - E_\pi, \mathbf{q} - \mathbf{p}_\pi)$, and the true coincidences were observed in the accumulated missing mass distribution

$$M_m \equiv (E_m^2 - |\mathbf{p}_m|^2)^{1/2} - M_n \, , \tag{4.1}$$

which was offset by $-M_n$ for practical reasons and was consequently expected to be centered around zero.

The missing mass spectrum for all coincident events of kinematics 437 without any cuts or corrections is shown in figure 4.4**a**. The signal-to-noise ratio is poor, and a cut in the coincidence time is applied to separate the true coincident events from the accidental ones. The resulting spectrum is shown in figure 4.4**b** (dark-shaded). The light-shaded spectrum corresponds to accidental coincidences and has to be subtracted.

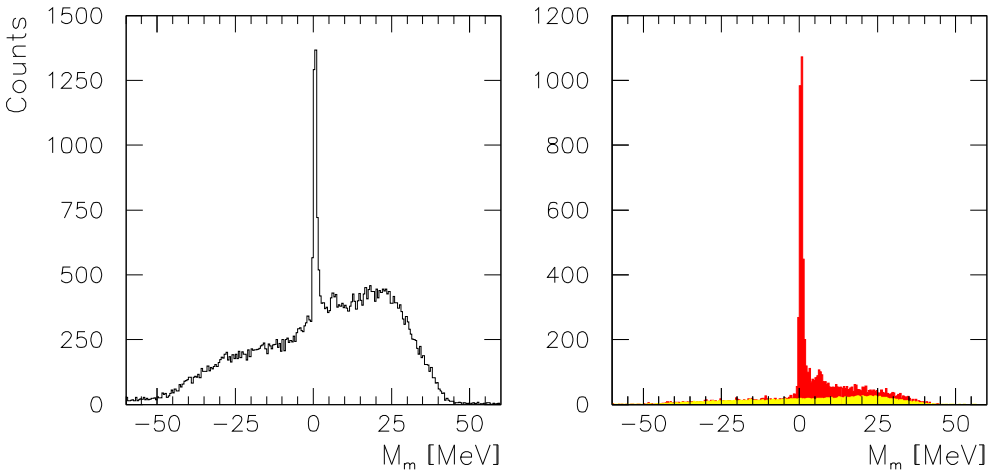

a **b**

Figure 4.4: The missing mass spectrum for kinematics 437: **a** – without any cuts, **b** – true coincidences within the $-2.5\,\text{ns} \le t_c \le 2.5\,\text{ns}$ cut (dark shading, corresponding to figure 4.3**b2**) and accidental coincidences within the $(-30\,\text{ns} \le t_c \le -10\,\text{ns}) \parallel (10\,\text{ns} \le t_c \le 30\,\text{ns})$ cut, correspondingly scaled down by a factor of $2 \times (30 - 10)/(2 \times 2.5) = 8$ (light shading in the same figure).

4.3 Further background reduction

In the measurement of $p(e, e'\pi^+)n$, three additional sorts of positively charged particles can enter the pion arm and be misidentified as pions: the *positrons* originating from the production of e^-e^+ pairs in the target, the *muons* stemming from charged pion decay in flight, and the *protons* recoiling from the $p(e, e')p$ elastic scattering.

Positron background

The positron background was eliminated by cuts in the Čerenkov detector energy spectrum. The positrons give a clear Čerenkov ADC energy signal of a very typical shape. This is illustrated by the bump in figure 4.5**b** for kinematics 648 with spectrometer B as the pion spectrometer. In this kinematics, particles with the ADC energies above 1337 (in units of ADC channels) were identified as positrons and the corresponding events were rejected.

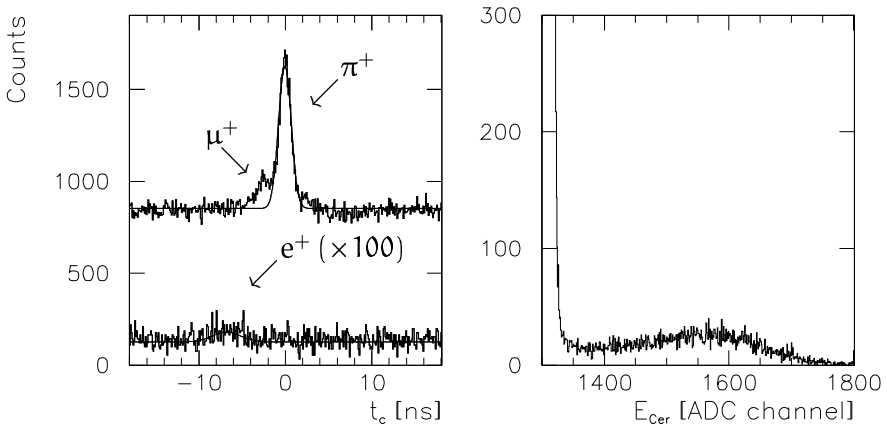

a **b**

Figure 4.5: The anatomy of a coincidence time spectrum for kinematics 648: **a**, upper histogram – no cuts, **a**, lower histogram – only events with $E_{\check{C}er} > 1337$, multiplied by 100, **b** – summed signal from the Čerenkov detector of spectrometer B (the pion spectrometer).

Particles that can be falsely identified as charged pions can in principle also partly be seen in the coincidence time spectrum. The upper histogram in figure 4.5**a** was generated without cuts, while the lower histogram (scaled by 100) contains only the events with $E_{\check{C}er} > 1337$ in the pion spectrometer (i. e. positrons). The lower histogram is faintly peaked at -6.8 ns, in agreement with the calculated $t_{ToF}(e^+) - t_{ToF}(\pi^+) \simeq -7$ ns for the average flight path through the spectrometer of 12 m and 227 MeV/c momentum. But observe that this small background is almost completely masked by the statistical fluctuations of the accidental coincidences, so that even if the positron signal were less 'flat', it can only be removed by the Čerenkov cut, and not by the cut in timing.

Muon contamination

The muon contamination, as opposed to the rather insignificant positron background, *can* be seen in the coincidence time spectrum, but it is impossible to isolate it with the time resolution we have. The left side-peak of the upper histogram in figure 4.5**a** corresponds to muons with momentum close to 227 MeV/c, for this momentum is estimated to give $t_{ToF}(\mu^+) - t_{ToF}(\pi^+) \simeq -2.5$ ns. But the muon peak and the dominating pion peak overlap and they can not be clearly

separated. The muon contamination was therefore retained within the coincidence time cut, but was later determined by a computer simulation and subtracted from other events in a procedure described in section 4.5.

Proton background

The proton background can be eliminated by a safe cut in the ADC energy spectrum of the dE scintillator layer in the pion spectrometer. The minimum ionising particles (pions, muons and positrons) deposit little energy in the scintillator material and contribute to the lower part of the energy distribution, whereas the protons deposit more energy and contribute to the upper part. The proton background was therefore removed by an appropriate cut in each kinematical setting. The sharp spikes of the energy spectrum originate from the ADC overflows in the uppermost channels of the measured range.

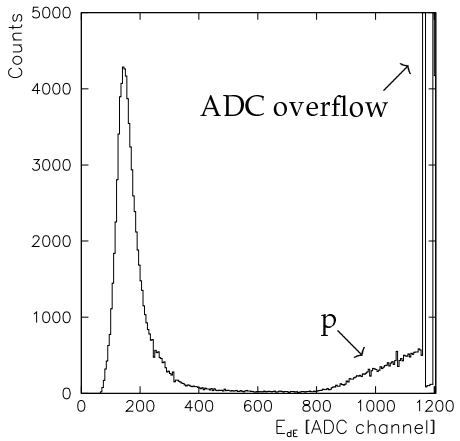

Figure 4.6: The ADC energy spectrum of the dE scintillator in spectrometer B, summed over all paddles, for kinematics 648. Protons deposit more energy in the scintillator material than the minimum ionising particles and accumulate in the upper part of the spectrum. In this example, the cut was applied at $E_{dE} = 730$.

4.4 Detector efficiencies

VDC efficiencies

There are two kinds of efficiencies that can be defined for a vertical drift chamber package, each consisting of four wire planes (see page 23 for description of the hardware). The *single wire efficiency* histogram for a VDC is generated from the 'number of wire' and the 'tagged wire' histograms. For each event, the two extreme wires (e. g. wire #100 and wire #105 of the total of 6 neighbouring wires in that event) that fired in each VDC layer are taken as reference wires. All the wires, i. e. the extreme two and the wires between them, are marked as 'tagged' and checked for hits. For the wires that fired, an entry is added at the appropriate place in the 'number of wire' histogram. The single wire efficiency histogram is obtained by dividing the accumulated 'number of wire' histogram by the accumulated 'tagged wire' histogram. Figure 4.7 is an example of a single wire efficiency histogram for the x1 layer of spectrometer A (for kinematics 437) with an average at 95.46 % (typically, average single wire efficiencies better than 85 % could be achieved for the x layers, and better than 95 % for the s layers).

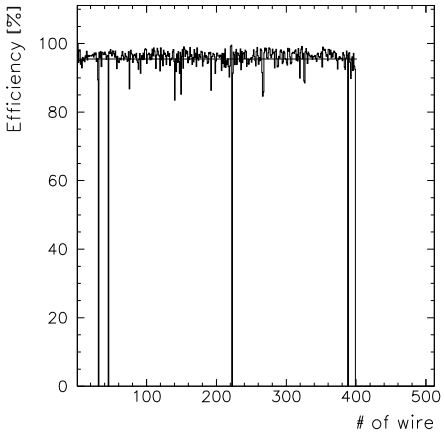

Figure 4.7: The single wire efficiency histogram for the x1 layer of spectrometer A (kinematics 437). The holes in channels #32, #46, #223 and #389 correspond to wires without any response.

If the VDC layers acted as independent detectors, a single layer efficiency of 95 % for all four layers would mean an overall VDC efficiency of only $(95\,\%)^4 \simeq 81\,\%$. However, the VDC's *overall efficiency* is defined as the ratio of all those events for which the particle trajectory could be successfully reconstructed, to all events that passed the VDC layers. To safely reconstruct the trajectory of a particle, at least three wires in the x-layers (x1 and/or x2) and at least three wires in the s-layers (s1 and/or s2) should fire. Trajectories can therefore not be reconstructed (or can be only inaccurately estimated) for events in which this 'joint' multiplicity lies below 6, and only such events diminish the overall efficiencies of the VDCs.

It is worthwhile to note that even if average single-wire efficiencies for one of the paired $(x1, x2)$ or $(s1, s2)$ layers drop to as much as 70 %, the overall efficiency of the drift chamber does not deteriorate significantly since the complementary layer usually supplies the relevant wire information. On the other hand, events with small multiplicities in a single layer or events in which a whole layer failed to respond, can have a very poor trajectory reconstruction.

For all settings but 219, 500 and 834 (where an overall VDC efficiency of 100 % was assumed), the overall efficiencies were determined from the measured single-wire efficiencies by a computer simulation. The chamber layers of given efficiencies (e. g. that in figure 4.7) were 'scanned' by particles impinging at different dispersive coordinates x and dispersive angles θ, which were both varied in accordance with the measured distributions. The overall efficiency was then determined by dividing the number of events that met the '3 + 3' criterion, with the total number of simulated events. As it has been expected, these efficiencies were always very close to 100 %, and are listed in table 4.1.

Table 4.1: Overall efficiencies of the vertical drift chambers of spectrometers A and B. For settings 219, 500 and 834 [84], the overall efficiencies were estimated to be 100 %. For all other settings, the efficiencies were determined by a computer simulation (see text for details).

Kinematics	229	437	742	259	457	648
$\varepsilon_{\mathrm{VDC\_A}}$	98.82 %	99.86 %	99.63 %	99.79 %	99.89 %	99.87 %
$\varepsilon_{\mathrm{VDC\_B}}$	99.70 %	99.93 %	99.99 %	99.92 %	99.94 %	99.94 %

Scintillator detector efficiencies

The efficiencies of the scintillator detectors were investigated in [84], where the three-detector method had been used to determine the efficiency of the dE layer (with the VDCs and the ToF layer as reference detectors) and of the ToF layer (with the dE layer and the Čerenkov detector acting as reference detectors) of each spectrometer. The sensitive area of the scintillator layers was 'scanned' by elastically scattered electrons, and only events lying within the target and nominal spectrometer acceptances were used for normalisation. Table 4.2 summarises the results.

Table 4.2: Efficiencies of the scintillator detectors of spectrometers A and B. In the present analysis, the overall efficiency was $\varepsilon_{\text{scint}} = 99.53\,\% \times 99.18\,\% = 98.71\,\%$.

Layer	dE	ToF	Overall
$\varepsilon_{\text{scint\_A}}$	$99.75\,\% \pm 0.01\,\%$	$99.78\,\% \pm 0.06\,\%$	$99.53\,\% \pm 0.07\,\%$
$\varepsilon_{\text{scint\_B}}$	$99.70\,\% \pm 0.01\,\%$	$99.48\,\% \pm 0.50\,\%$	$99.18\,\% \pm 0.51\,\%$

The small overall efficiency deteriorations of 0.47 % for spectrometer A and 0.82 % for spectrometer B originate entirely in the imperfect junctions of the paddle pairs (see figure 3.8) and can not be eliminated without overlapping paddles in each plane. However, overlapping was avoided since it would lower the reliability of the particle identification using energy loss.

Čerenkov detector efficiencies

Only electrons trigger a signal in the Čerenkov detectors (cf. subsection 3.3), so that the Čerenkov efficiency for the detection of electrons is equal to $N_{\text{det}}/N_{\text{s}}$, where N_{det} is the number of electrons actually seen by the detector and N_{s} is the number of electrons that traversed it and had energies large enough to cause the Čerenkov effect. The veto efficiency, on the other hand, equals $1 - N_{\text{det}}/N_{\text{sn}}$, where N_{sn} is the number of particles traversing the detector which should *not* cause the Čerenkov effect, and N_{det} is the number of particles that were nevertheless seen by the detector. The efficiencies of the Čerenkov detectors were tuned to have at least eight photoelectrons reaching the first dynode of one of the photo-multipliers per event, and were studied in [86] applying the three-detector method with the ToF scintillators at the lower side and the Top scintillators on the upper side of the Čerenkov counters. The results are shown in table 4.3.

Coincidence efficiency

The coincidence efficiency of a double coincidence experiment can be defined as the ratio of the $H(e,e'p)$ coincidence cross-section to the $H(e,e')$ elastic scattering (inclusive) cross-section. If both reactions are measured at equal kinematical conditions, the cross-sections should be equal. In other words, the coincidence efficiency measures the ability of the event-builder to combine, synchronise, and process two completely independent spectrometer data streams. This was studied in detail in a previous work [84], and we used the value of $\varepsilon_{\text{coinc}} = 0.996$ quoted there. The systematical uncertainty of the overall detector (VDCs, scintillator counters and Čerenkov detectors) and coincidence efficiency was estimated to be 1 % for all settings [84].

Table 4.3: Efficiencies of the Čerenkov detectors of spectrometer A and B for the identification of electrons and for veto operation (pions). For details of the analysis, see [86]. In our measurement, the Čerenkov detectors were not used as an active part of the trigger-system, but only in the off-line analysis.

Particles	Electrons	Veto (pions)
ε_{Cer_A}	99.98 %	100.00 %
ε_{Cer_B}	99.97 %	100.00 %

4.5 Correction factors

Dead time correction

The overall dead time of a coincidence setup originates in individual dead times of the detectors, readout and trigger electronics, and data acquisition software. In our experiment, the major contribution to the overall dead time comes from the software, by far exceeding the intrinsic detector dead times. The dead time correction factor for a coincidence measurement with spectrometers A and B can be expressed as $K_{dead} = 1/(1 - \varepsilon_{dead})$, where

$$\varepsilon_{dead} = \frac{t_{dead}}{t_{run}} = \frac{t_{dA} + t_{dB} - t_{dAB}}{t_{run}} + \frac{n_A t_{tA} + n_B t_{tB} - n_{AB} t_{tAB}}{t_{run}} . \tag{4.2}$$

The t_{dA}, t_{dB} and t_{dAB} in the first term of 4.2 denote the data acquisition dead times of the individual spectrometers and of the coincidence setup, respectively. The second contribution corresponds to the trigger electronics (mostly due to the coincidence PLU module) dead times of $t_{tA} = t_{tB} = t_{tC} = 90$ ns *per event* (settings 437, 648, 457 and 259; in all other settings, 500 ns) for each of the single events n_A and n_B or coincident events n_{AB}. Overall dead times t_{dead} and total run-times t_{run} for all measured runs are listed in table 4.4. The systematical uncertainty of the dead time correction is 0.5 % [84].

Table 4.4: Overall dead times t_{dead}, total run-times t_{run} (all in [s]), ε_{dead} and K_{dead} for all measured settings. Note that the entry for setting 834 [84] corresponds only to the measurement parallel to q.

Kinematics	219	500	834	229	437	742	259	457	648
t_{dead}	1991	1051	610	1992	623	735	2837	1536	2234
t_{run}	86494	48628	20215	99950	44926	19403	159744	109716	48534
ε_{dead}	0.023	0.022	0.030	0.020	0.014	0.038	0.018	0.014	0.046
K_{dead}	1.024	1.022	1.031	1.020	1.014	1.039	1.018	1.014	1.048

Pion decay correction

By far the largest correction factor to the measured number of events originates in the charged pion decay $\pi^+ \rightarrow \mu^+ \nu_\mu$ in flight from the target to the detectors. The decay follows the simple

exponential law

$$\frac{N_\pi^{det}}{N_\pi^{tg}} = e^{-s/l_\pi} \equiv \frac{1}{K_{decay}}, \tag{4.3}$$

where $l_\pi = (E_\pi/m_\pi c^2)\tau_\pi\beta_\pi c = (p_\pi/m_\pi c)\tau_\pi c$ is the pion decay length, with the pion lifetime (in the frame where the pion is at rest) of $\tau_\pi = 26.03$ ns ([24], p. 321). This amounts to $l_\pi \simeq 11$ m for a typical pion momentum of $p_\pi = 200\,\mathrm{MeV/c}$, meaning that during their flight through e. g. spectrometer B with the reference trajectory length of $L_{ref} = 12.03$m, two thirds of pions decay (the situation is not much more favourable in spectrometer A with $L_{ref} = 10.75$m). The scintillator planes are then hit by the remaining pions and by the fraction of the muons that were not stopped in the collimator slits or internally in the spectrometer walls.

The problem is that muons with momenta very close to the pion momenta can not be distinguished from the pions by either time of flight differences or differences in the ADC spectrum of the scintillators. The muons represent a certain contamination of the pions, which can only be determined by a computer simulation. We used the RAYTRACE computer code [97] for tracing particle rays through optical systems that was later upgraded for pion decay [98].

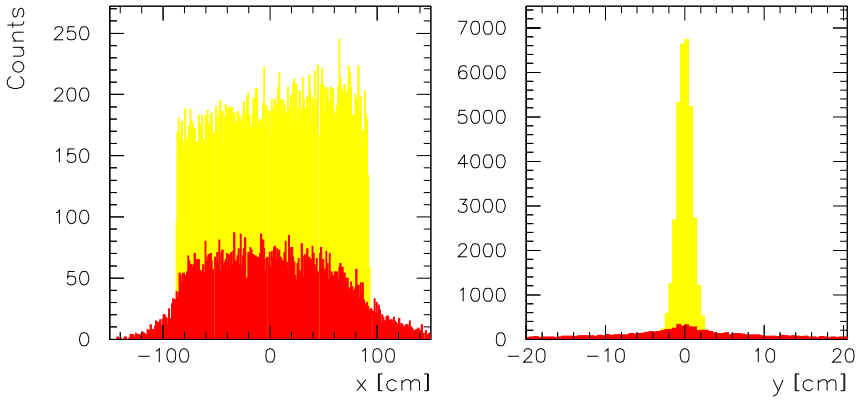

a **b**

Figure 4.8: Muon contamination in the focal plane of spectrometer B in kinematics 457: **a** – in the dispersive coordinate x, **b** – in the non-dispersive coordinate y. The light shaded histograms correspond to the pions, and the dark shaded ones to the muons from the pion decay.

Figure 4.8 shows the simulated distributions of pions and muons from the pion decays, in the dispersive focal-plane coordinate x and in the non-dispersive coordinate y of spectrometer B with the central momentum of 227 MeV/c (the distribution in the dispersive angle θ roughly resembles that in x, whereas the distribution in the non-dispersive angle ϕ looks similar to that in y). In a previous work [84], the pion decay correction was determined in two steps of the simulation. First, initial pion rays were randomly and uniformly distributed over the spectrometer acceptance and transported to the focal plane, allowing pions to decay underway. Cuts were then applied in the four focal plane distributions (x, θ, y and ϕ) that corresponded to pions; the muon contamination R_μ in the focal plane was then identified with the remaining muons surviving all four cuts, i. e. $R_\mu \equiv N_\mu/(N_\pi + N_\mu)$. This contamination was then subtracted from the number of detected coincident events. The result was then multiplied by the correction factor K_{decay}, obtained from (4.3) with $s = L_{ref}$.

In this work, a more accurate approach is attempted, largely mandated by the use of the extended liquid hydrogen target and motivated by improved means of particle tracing and backtracing. Again we first randomly generated a sample of pion rays originating at the target, but with linear and angular distributions corresponding to the actual extension of the target and

to the beam wobbling amplitudes actually used in the experiment. All the particles reaching the focal plane, the pions as well as the muons, were then back-traced to the target. A sample result of a back-tracing procedure is shown in figure 4.9 for kinematics 457, showing original pion distributions, back-traced pion distributions, and back-traced muon distributions in four target coordinates. The cuts can then be applied *at the target*. The ratio K_{decay} of the number of the pions that survived the cut, to the original number of pions, reduced for the muon contamination R_μ within the cuts, was finally interpreted as the total pion decay correction factor. Table 4.5 summarises the correction factors for all measured kinematical settings. The systematical uncertainty of $(1 - R_\mu)K_{decay}$ was estimated to be 1.6 % for settings 834 and 500, 1.8 % for setting 219, 0.6 % for setting 229, and 0.5 % for all other settings.

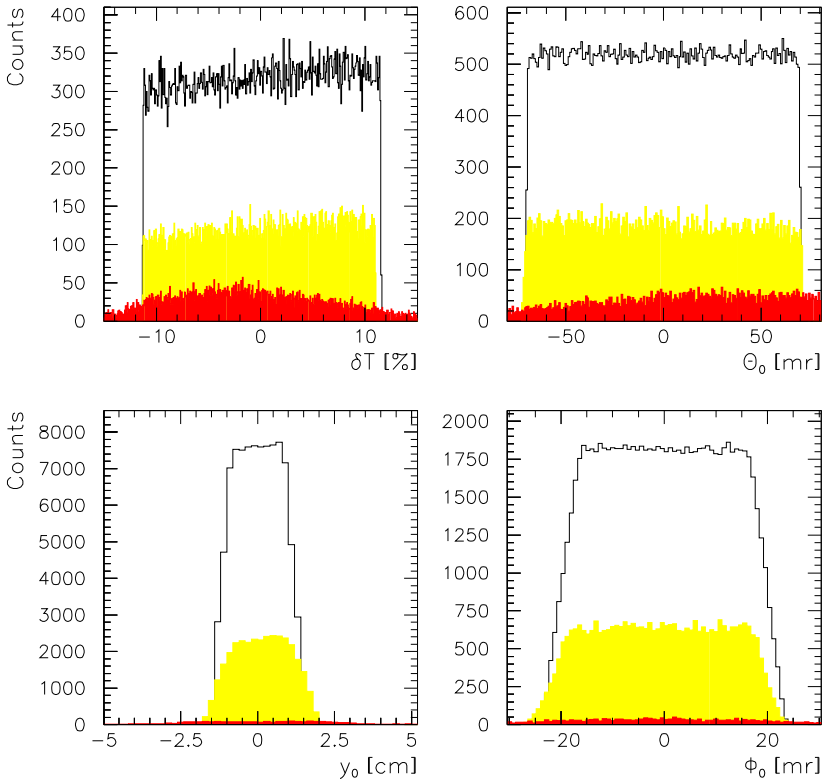

Figure 4.9: Pion and muon distributions after back-tracing the particles from the focal plane of spectrometer B back to the target (kinematics 457, extended target with a wobbled beam), in: **a** – kinetic energy deviation $\delta T \equiv (T - T_{ref})/T_{ref}$, **b** – dispersive angle on target, **c** – vertex on target, and **d** – non-dispersive angle on target. Unshaded histograms correspond to pion rays entering the simulation, light shaded histograms to back-traced pions, and dark shaded histograms to back-traced muons.

Radiation loss corrections

The electrons and the pions of the $p(e, e'\pi^+)n$ reaction interact with the target protons and with the electron clouds of the target atoms, and thereby lose a fraction of their energy by radiating additional real or virtual photons. Since these *radiation losses* can not be directly measured, the reconstructed energy transfer, momentum transfer, missing mass and related distributions become distorted: they exhibit *radiative tails*, populated by events in which some of the particles involved lost a part of their energy. Three mechanisms of energy losses are

involved in the $p(e, e'\pi^+)n$ reaction: internal Bremsstrahlung, external Bremsstrahlung, and target ionisation (see Appendix D for details).

Table 4.5: Simulated muon contamination R_μ and the pion decay correction factors K_{decay} for all measured settings. Note that in settings 219, 500 and 834, the total correction factor $(1 - R_\mu)K_{decay}$ was determined from the simulated pion and muon distributions in the focal plane, whereas for all other settings, it was extracted from the same distributions back-traced to the target.

Kinematics	219	500	834	229	437	742	259	457	648
R_μ	0.072	0.148	0.148	0.010	0.017	0.111	0.017	0.018	0.018
K_{decay}	3.116	2.953	2.891	2.910	2.909	2.512	2.668	2.660	2.674

The energy loss correction can be done by counting the number of events $N(\Delta M_m)$ within a certain interval ΔM_m above the peak of the background-free spectrum of $M_m - M_n$ and multiplying it by the correction factor $K_{rad}(\Delta M_m) = K_{Schw}(\Delta M_m)\, K_{brems}(\Delta M_m)\, K_{Land}(\Delta M_m)$ corresponding to the 'cut-off' energy ΔM_m. The $N(\Delta M_m)\, K_{rad}(\Delta M_m)$ is then interpreted as the 'true' number of coincident events, i. e. events that would have been observed, had there been no energy losses. This approach was followed by [84] for settings 834, 500 and 219. In the energy ranges of our experiment, the electrons lose their energy almost exclusively by Schwinger radiation. Bremsstrahlung of pions is further suppressed by a factor of m_e^2/m_π^2 and may be neglected. The pions only lose energy through ionisation losses, but for our kinematical settings and typical cut-off energies of $\sim 10\,\mathrm{MeV}$, the correction factors are close to 1. Energy losses due to Landau straggling can be neglected for target thicknesses smaller than 0.05 of the target material's radiation length. The overall correction factor K_{rad} was 1.227 for setting 834, 1.182 for 500, and 1.156 for 219 [84], and its systematical uncertainty was estimated to be 2 %.

But the problem is that the energy losses of the particles do not map trivially to the corresponding changes in the missing mass, since M_m (4.1) is a non-linear function of E_e, E'_e and E_π. For example, it is obvious that an incoming electron's energy loss of 10 MeV, which is also 'inherited' by the exchanged virtual photon, will not necessarily correspond to a shift of 10 MeV in the distribution of M_m. We therefore incorporated the radiative correction into the acceptance simulation (see subsection 4.7 for details). The advantage of this approach is the possibility to properly handle the particles' energy losses in the target and in the variety of other materials of entrance and exit foils. In addition, beam wobbling amplitudes were equal to those actually used in the experiment, so that the detector acceptances were consistently folded into the radiative tails. The systematical uncertainty of the radiative loss correction was estimated to be 3.9 % (setting 259), 2.8 % (457, 742), 2.6 % (437), 1.2 % (229), and 1.0 % (648).

4.6 Luminosity

The integrated luminosity is defined as the product of the number of target nuclei per unit surface N_t and the number of electrons N_e impinging on the target in a time span T

$$N_e = \frac{Q_{tot}}{e_0} = \frac{1}{e_0}\int_0^T I_e dt\,.$$

Determining the integrated luminosity therefore effectively amounts to measuring the integral charge accumulated on the target. The beam current is measured with the probes described

in section 3.2, and the elapsed time information is kept in the run-time and real-time scalers controlled by the μBusy module; during data taking, these scalers are read out and their values directly entered into the data stream. To calculate the number of target nuclei per unit surface from a given target density ρ and average target length $\overline{x}$, we use

$$N_t = \frac{\rho\,\overline{x}\,N_A}{A},$$

where N_A is the Avogadro number and A is the mass number. Because the beam wobbler was used at all times during our experiment, illuminating different portions of the target for different deflection amplitudes (see figure 3.3), the target length has to be averaged over these amplitudes. Table 4.6 shows the values determined for the two target cell types.

Table 4.6: Average target cell length $\overline{x}$, target density ρ and the number of target nuclei per unit surface N_t for two types of LH_2 target cells used in the experiment († $A = 2.000$; †† $A = 1.008$.)

Kinematics	$(219,500,834)^\dagger$	$(229,742)^{\dagger\dagger}$	$(437,259,457,648)^{\dagger\dagger}$
$\overline{x}$ [cm]	1.868±0.5 %	1.868±0.5 %	4.886±0.3 %
ρ [g/cm^3]	0.1374±0.5 %	0.0708±0.5 %	0.0708±0.5 %
N_t [10^{22}/cm^2]	7.731±0.7 %	7.730±0.7 %	20.67±0.6 %

In the coincidence experiment we performed, the data streams of individual spectrometers were combined into a single event stream in the final stage of the data acquisition system (see figure 4.10 for an illustration of the time sequence of spectrometer data streams as seen by the acquisition software).

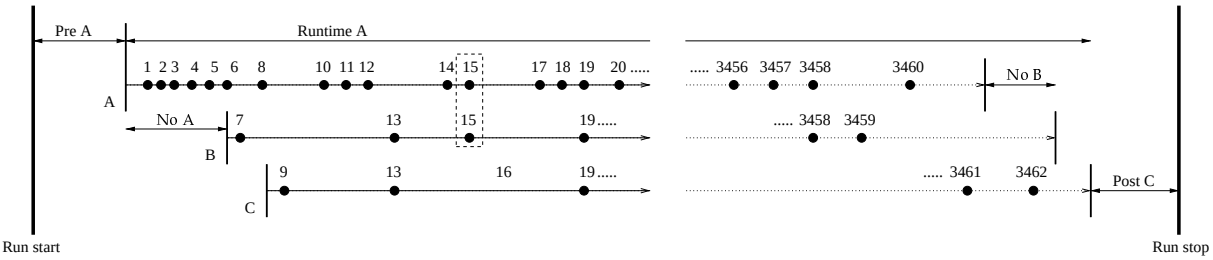

Figure 4.10: Spectrometer data streams in an experiment utilising three spectrometers. Bullets represent single events and numbers represent their sequential numbers. For example, events #15 and #3458 are AB coincidences, and event #19 is an ABC coincidence. Only the time period during which spectrometer A's and spectrometer B's data streams overlap can be used for the evaluation of luminosity in an AB coincidence experiment.

The time intervals called 'Pre A' and 'Post C' in the figure, during which the actual data taking has not started or finished yet, are irrelevant. But the differences between the starts and stops of the individual spectrometer data streams ('No A' and 'No B' in the figure), *are* important to the luminosity calculation for an AB-coincidence experiment. Since there can obviously be no coincident events during these (relatively short) acquisition starting and stopping procedures' dead times, only the time when spectrometer streams 'overlap' may be used for the luminosity calculation. Correspondingly, only those events from the data stream may be used in the

analysis that fit into the time window after the 'No A' and before the 'No B'. The average electron beam currents, the total accumulated charges and integrated luminosities for all measured settings, and their systematical uncertainties are listed in table 4.7.

Table 4.7: Average electron beam currents $\bar{I}_e$, total accumulated charges Q_{tot} and integrated luminosities L for all measured settings (the entry for setting 834 [84] corresponds only to the measurement parallel to $\mathbf{q}$). Note that for settings 437, 259, 457 and 648, $L \neq N_t Q_{tot}/e_0$ since the small corrections due to the data acquisition dead times mentioned above have already been taken into account. The systematical uncertainties of Q_{tot} and L originate in the uncertainties of the Förster probes and in the fluctuations of the target density.

Kinematics	$\bar{I}_e$ [μA]	Q_{tot} [As]	L [10^{41}/cm^2]
219	33.6	3.106±0.5 %	14.985±0.9 %
500	33.5	1.628±0.5 %	7.855±0.9 %
834	14.3	0.2899±1.1 %	1.399±1.3 %
229	33.9	3.824±0.3 %	18.451±0.6 %
437	19.5	0.8716±0.03 %	11.368±0.5 %
742	21.8	0.4783±0.5 %	2.308±0.7 %
259	23.1	3.662±0.02 %	47.768±0.5 %
457	16.8	1.843±0.03 %	24.043±0.5 %
648	25.1	1.215±0.01 %	15.844±0.5 %

4.7 Spectrometer acceptances

When two spectrometers are used in a coincidence experiment, the ranges of the kinematical variables they cover (the so-called *nominal spectrometer acceptances* as given for instance in table 3.1) are in general much smaller than the ranges of the same variables that occur at the target. Specific geometries and experimental conditions (different spectrometer angles, collimators, scattering cell types, beam wobbling, or imperfect detector efficiencies) and the energy-momentum constraints of the reaction being studied further narrow the kinematical 'slit' in which coincidence events can be observed. Unfortunately, this 'slit' is almost impossible to calculate analytically since the mapping of the box-like nominal acceptances to the actual distribution of the events as seen by the spectrometers is very complex. The only possibility to determine the actual acceptance is to use a computer simulation. Single-arm events are generated at the target in kinematical ranges exceeding the nominal spectrometer acceptances, and individual particle rays are checked for momentum and angles at the spectrometers. For a sufficiently large number of tries, the ratio between the accepted coincidence events N and the events generated at the target N_{tg} approaches the ratio of the actual acceptance to the nominal acceptance. In the case of $p(e,e'\pi^+)n$,

$$\int_{\Delta E'_e\,\Delta\Omega'_e\,\Delta\Omega_\pi} dE'_e\,d\Omega'_e\,d\Omega_\pi = \frac{N}{N_{tg}}\,\Delta E'_e\,\Delta\Omega'_e\,\Delta\Omega_\pi\,. \tag{4.4}$$

The acceptance integral reflects only the geometry of the setup and energy-momentum conservation, but does not have any further physical content, and has to be divided out from the observed spectra. In the analysis of our experiment, the particles' radiation losses, the calcula-

tion of the virtual photon flux Γ_v and the frame transformation $d\Omega_\pi \rightarrow d\Omega^\star_\pi$ implied in the step from (2.2) to (2.3) were also included in the acceptance simulation.

First, a valid reaction point is randomly generated according to the beam wobbling amplitudes equal to those used in the experiment. When the reaction point is known, the length of the path (and the corresponding energy loss) of the incoming electron through the target cell can be calculated. Second, the scattered electron is generated. One randomly selects its dispersive and non-dispersive angle from ranges $\Delta\Omega'_e = \Delta \sin\theta'_e \, \Delta\phi'_e$ that slightly exceed the nominal angular acceptance of the electron spectrometer, and a value of q^2 from a sufficiently broad interval, so that the momentum of the scattered electron (which can be calculated from the angles and from q^2) lies within $\Delta E'_e$. One then checks whether the outgoing electron passes the collimator: if it does, the length of its path through the target cell is calculated and a corresponding energy loss is forced. If the momentum of the electron still fits into the momentum bite of the spectrometer, one has a *valid electron*; in all other circumstances, the event is rejected.

The calculation now proceeds in the centre-of-mass frame. If the scattered electron was accepted, the virtual photon flux Γ_v is calculated from the *energy-loss–subtracted* E_e, E'_e and q^2, and the event is weighted by $\Gamma_v \Delta E'_e \, \Delta\Omega'_e$ times $\Delta\Omega^\star_n \equiv \Delta\Omega^\star_\pi = \Delta \sin\theta^\star_\pi \, \Delta\phi^\star_\pi$ and normalised to the total number of tries (this very last step can be done at any point). Since the four-vectors of the photon and the target proton are known, the magnitudes of the CMS three-momenta in $\mathbf{p}^\star \equiv \mathbf{p}^\star_n + \mathbf{p}^\star_\pi = 0$ can be calculated from the $\gamma_v + p \rightarrow n + \pi^+$ kinematics. Finally, the spherical angles of the *neutron* are randomly selected, the neutron is boosted from the centre-of-mass frame to the laboratory frame, and the pion four vector is calculated from $\mathbf{p}_n$. If the outgoing pion then passes the collimator, the length of its path through the target cell is calculated and a corresponding energy loss is forced. If the momentum of the pion fits into the momentum bite of the spectrometer, one has a *valid coincidence event*, which receives an additional weight due to vertex corrections (see appendix D for details). In all other circumstances, the whole event is rejected. To be able to compare the simulated particle distributions to the ones obtained from the analysis program, the energy losses of the event are corrected for in the last step of the simulation. The results of the simulation are summarised in table 4.8.

Table 4.8: The acceptance integral (4.4), expressed in the centre-of-mass frame of the final hadrons, in units of $[10^{-9}\mathrm{sr}^2]$ for the measurements at $q^2 = -0.195$ and $-0.273\,\mathrm{GeV}^2/c^2$. The energy losses of the particles involved were included in the simulation: the (50) value includes all events in the simulated missing mass spectrum, whereas the (10) value implies a $M_m \leq 10\,\mathrm{MeV}$ cut actually used in the analysis. For the calculation of the acceptance integral at $q^2 = -0.117\,\mathrm{GeV}^2/c^2$, where a different procedure has been adopted to handle the particles' energy losses, refer to [84].

Kinematics	229	437	742	259	457	648
$\int \Gamma_v dE'_e \, d\Omega'_e \, d\Omega^\star_\pi$ (50)	0.7308	1.6339	5.9777	0.7826	1.4803	3.0083
$\int \Gamma_v dE'_e \, d\Omega'_e \, d\Omega^\star_\pi$ (10)	0.7245	1.5319	5.5835	0.7426	1.3638	2.7192

4.8 The differential cross-section

To determine the reaction cross-section (2.2) for $p(e, e'\pi^+)n$, we count all 'true' events (i. e. background free pion-electron coincident events) and normalise their number to the luminosity and to the acceptance covered by the spectrometer setup. The 'true' number of events N_{true} is isolated from the measured number of events N_{exp} by eliminating the background N_{bg} (through

subtraction of accidental coincidences and performing cuts to dispose of the remaining background), and by applying the correction factors described in sections 4.3 to 4.5,

$$N_{true} = (N_{exp} - N_{bg})\,(1 - R_\mu) K_{decay}\, K_{dead}\, \frac{1}{\varepsilon_{VDC}\,\varepsilon_{scint}\,\varepsilon_{Cer}\,\varepsilon_{coinc}} .$$

The luminosity $L = N_t Q_{tot}/e_0$ is determined from the properties of the target and from the measurement of the total accumulated charge, as described in section 4.6. The sole quantity that can exclusively be obtained by a computer simulation, is the actual physical detection volume available to the particles in the final state. The cross-section, averaged over the nominal acceptance na $\equiv \Delta E'_e\,\Delta\Omega'_e\,\Delta\Omega_\pi$, is then

$$\left.\frac{d\sigma}{dE'_e\,d\Omega'_e\,d\Omega_\pi}\right|_{na} = \frac{N_{true}}{L \int_{na} dE'_e\,d\Omega'_e\,d\Omega_\pi} .$$

Since the reaction cross-section for $p(e,e'\pi^+)n$ also assumes a factorised form (2.3), the physically relevant differential cross-section $d\sigma/d\Omega^\star_\pi$ can be calculated from

$$\frac{d\sigma}{d\Omega^\star_\pi} = \frac{N_{true}}{L \int_{na} \Gamma_v J_\pi\, dE'_e\,d\Omega'_e\,d\Omega_\pi} . \tag{4.5}$$

As indicated in (4.5) and discussed in section 4.7, the virtual photon flux factor Γ_v and the Jacobian determinant J_π were directly included in the acceptance calculation, in which each accepted event is appropriately weighted. The measured cross-sections are listed in table 4.9.

Results and analysis

Table 4.9: Measured centre-of-mass cross-sections for the $p(e,e'\pi^+)n$ reaction at $W = 1125\,\mathrm{MeV}$ and four-momentum transfers q^2 of -0.117 (settings 219, 500, 834), -0.195 (229, 437, 742), and $-0.273\,\mathrm{GeV}^2/c^2$ (259, 457, 648). See also table 2.1.

Kinematics	$d\sigma/d\Omega^\star_\pi$ [μb/sr]	Stat. error [μb/sr]	Syst. error [μb/sr]
219	5.96	0.14 (2.3%)	0.19 (3.2%)
500	8.40	0.11 (1.3%)	0.31 (3.7%)
834	11.14	0.08 (0.7%)	0.41 (3.7%)
229	4.69	0.10 (2.2%)	0.08 (1.8%)
437	5.61	0.10 (1.8%)	0.16 (2.9%)
742	7.73	0.12 (1.6%)	0.24 (3.1%)
259	3.55	0.05 (1.5%)	0.15 (4.1%)
457	4.16	0.06 (1.4%)	0.13 (3.1%)
648	5.13	0.06 (1.1%)	0.09 (1.7%)

Since all measurements were performed in parallel kinematics, the interference cross-sections vanish, and the transverse and the longitudinal cross-sections could be separated by applying the Rosenbluth method to data points at constant q^2, but various εs (see section 2.2). The slopes and the y-axis intercepts of the straight-line fits of cross-sections from (2.5) were identified with the longitudinal and the transverse cross-sections, respectively. Figures 4.11 and 4.12 show the results of the fits and the results for the separated transverse and longitudinal cross-sections in dependence of q^2, including the predictions of the models of Drechsel and Tiator (DT) ([38], section 5.2) and of Drechsel, Hanstein, Kamalov and Tiator (DHKT) ([39], appendix E).

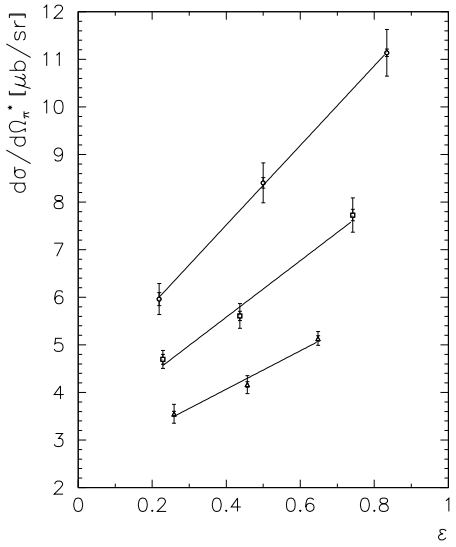

q^2 [GeV^2/c^2]	$d\sigma_T/d\Omega^*_\pi$ [μb/sr]	$(-q^2/\omega^{*2})\, d\sigma_L/d\Omega^*_\pi$ [μb/sr]
−0.117	4.160 ± 0.165	8.394 ± 0.254
−0.195	3.208 ± 0.149	5.933 ± 0.307
−0.273	2.452 ± 0.094	4.038 ± 0.201

Figure 4.11: Least-squares straight-line fits to the measured cross sections at constant values of q^2 as functions of the virtual photon polarisation ε. The slopes of the fits are proportional to the longitudinal, and the y-axis intercepts of the fits to the transverse cross-sections (see (2.5)). The smaller error bars correspond to statistical, the larger ones to the sum of statistical and systematical uncertainties.

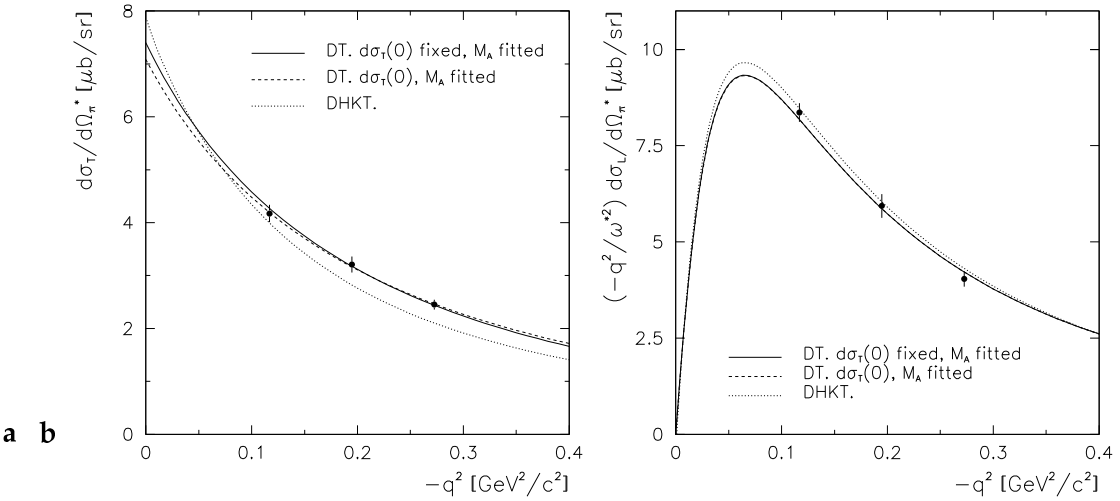

Figure 4.12: Separated **a** – transverse and **b** – longitudinal cross-sections at $W = 1125\,\mathrm{MeV}$, together with the q^2-dependence predicted by the DT and DHKT models. Full curves: DT model fit to the data points with $d\sigma_T(0)$ fixed by photo-production data (see also figure 5.3) and M_A as the fit parameter; dashed curves: DT model fit with $d\sigma_T(0)$ as the second fit parameter; dotted curves: DHKT model.

In the analysis of the q^2-dependence of the cross-sections, resorting to an effective Lagrangian model was inevitable, since the values of q^2 and W in the experiment were still too high for the current development stage of the χPT. The DT model we used in the analysis is a gauge-invariant model for charged pion electro-production in the region below the Δ-resonance. In this model, the procedure of gauge-invariance restoration influences only the longitudinal cross-section, whereas the transverse part containing the axial form factor remains unaffected. The q^2-dependence of the form factor (or the corresponding value of M_A) can hence be extracted from the fit of the calculated transverse cross-section to the experimental data with an enhanced sensitivity. Two approaches were attempted.

In the first approach, only the axial mass was varied, whereas the cut-off energy of the pion (monopole) form factor was set to $\Lambda_\pi = 0.682\,\mathrm{GeV}$. The value of $d\sigma_T$ at $q^2 = 0$ was fixed to 7.4 μb/sr, indicated by the photo-production dispersion analysis of [101]. In the second approach, we used the same value of Λ_π, but treated $d\sigma_T(0)$ as an independent fit variable, yielding the value of $d\sigma_T(0) = (7.05 \pm 0.54)\,\mu\mathrm{b/sr}$. In both methods, the resulting best-fit parameters for the transverse part were then used in the fit of the longitudinal part.

Using the first and preferred method, we find $M_A = (1.073 \pm 0.016)\,\mathrm{GeV}$, corresponding to $\langle r_A^2\rangle^{1/2} = (0.637 \pm 0.010)\,\mathrm{fm}$. From the longitudinal part, we obtain $\Lambda_\pi = (0.673 \pm 0.018)\,\mathrm{GeV}$, corresponding to $\langle r_\pi^2\rangle^{1/2} = (0.718 \pm 0.019)\,\mathrm{fm}$. Using the second method, we get $M_A = (1.105 \pm 0.059)\,\mathrm{GeV}$ or $\langle r_A^2\rangle^{1/2} = (0.618 \pm 0.033)\,\mathrm{fm}$, and $\Lambda_\pi = (0.685 \pm 0.019)\,\mathrm{GeV}$ or $\langle r_\pi^2\rangle^{1/2} = (0.706 \pm 0.019)\,\mathrm{fm}$. The results indicate that our extracted value of $M_A = (1.073 \pm 0.016)\,\mathrm{GeV}$ is $(0.056 \pm 0.028)\,\mathrm{GeV}$ larger than the axial mass $M_A = (1.017 \pm 0.023)\,\mathrm{GeV}$ known from neutrino scattering experiments. Our value essentially overlaps with the scaled-error weighted average $M_A = (1.068 \pm 0.017)\,\mathrm{GeV}$ of all older pion electro-production experiments. If we append it to the database, the weighted average increases to $M_A = (1.070 \pm 0.012)\,\mathrm{GeV}$ (see the corresponding figure 7.1), and the 'axial mass discrepancy' becomes $\Delta M_A = (0.053 \pm 0.026)\,\mathrm{GeV}$.

5

Extracting $G_A(q^2)$ from experiment

The theoretical fits in figure 4.12 are meeting points of experimental data and theoretical models, and exploit the q^2-dependence of the cross-section to probe the matrix element of the model axial current and, equivalently, the axial form factor.

In the past few decades, the knowledge on the q^2-behaviour of the axial form factor emerged from an interplay between experimental improvements and gradual sophistication of theoretical models. But apart from the uncertainties related to the estimates of centre-of-mass motion and recoil effects (which will be referred to in the next chapter), these models were facing another correction problem. Early attempts to describe low energy photo-production of massless charged pions can be traced back to the Kroll-Ruderman formula (2.8). Their result was subsequently extended to virtual photons by Nambu, Lurié and Shrauner [73, 74], who calculated the isospin-odd electric dipole amplitude at threshold (2.9). Expanded to the order of q^2,

$$E_{0+}^{(-),\,\mathrm{NLS}}(m_\pi = 0, q^2) = \frac{e g_A}{8\pi f_\pi}\left\{1 + \frac{q^2}{6}\langle r_A^2\rangle + \frac{q^2}{4M^2}\left[\kappa_v + \frac{1}{2}\right] + \mathcal{O}(q^3)\right\}, \tag{5.1}$$

where κ_v is the isovector anomalous magnetic moment of the nucleon (see also section 5.3). (In turn, the longitudinal s-wave multipole $L_{0+}^{(-)}$ additionally appearing in electro-production contains the isoscalar anomalous magnetic moment and the pion form factor $F_\pi(q^2)$.) This result can be used to extract the axial radius r_A from experimental data on threshold pion electroproduction. Namely, since in the immediate vicinity of the threshold only s-wave multipoles contribute to the cross-section (2.3), it can be expressed in a simplified form

$$\frac{Q_\gamma^\star}{|\mathbf{p}_\pi^\star|}\frac{d\sigma_v}{d\Omega_\pi^\star} = a_0 + \varepsilon_L^\star a_0' = |E_{0+}|^2 + \varepsilon_L^\star |L_{0+}|^2 \tag{5.2}$$

according to (B.10) and (B.11) [4]. For the $p(e,e'\pi^+)n$ reaction, $E_{0+}^{(-)}$ is the dominant multipole containing $\langle r_A^2\rangle$. The experimental value for the threshold cross-section was therefore obtained by extrapolation from a range of energies W down to threshold $W = M + m_\pi$, and $\langle r_A^2\rangle$ could be isolated from the q^2-slope of the cross-section using (5.1) and (5.2). The problem is that (5.1) was also formulated for unphysical pions with zero four-momentum (and therefore zero mass), and to be able to confront the experiment, it had to be extrapolated into the physical region with $m_\pi \neq 0$ and $\mathbf{p}_\pi \neq 0$. There were several attempts to tackle this problem.

[4] When a specific physical channel is considered, appropriate isospin combination of the multipoles appear in (5.2) (see appendix C for the definitions).

5.1 Early theories

Furlan, Paver and Verzegnassi (FPV) were among the first authors who tried to extend (5.1) to physical pions. Their method was based on current algebra and on the approach of [117], in which the generic physical reaction amplitude $F(\nu = p_p p_\pi, u = p_\pi^2 = m_\pi^2)$ was derived from the soft-pion amplitude $F(0,0)$ by means of a dispersion relation

$$F(\nu, m_\pi^2) = F(0,0) + \frac{m_\pi^2}{\pi} \int_\gamma du' \, \frac{\mathrm{Im}\, F(u')}{u'(u' - m_\pi^2)} \,,$$

where the integration path γ lies in the (ν, u)-plane. Such dispersion relations are a means to use analytical continuations of the physical amplitudes into the complex plane in order to be able to connect them to other observables (e. g. to connect $\mathrm{Im}\, F(u')$ to the total cross-section using the optical theorem [103]). It was hoped that the integration could be performed in such a way that the dispersion corrections would be small. It was shown [75, 76, 77, 6] that the corrections to the transverse multipole (5.1)

$$E_{0+}^{(-),\,\mathrm{FPV}}(m_\pi, q^2) = E_{0+}^{(-),\,\mathrm{NLS}}(0, q^2) + \delta E_{0+}^{(-)}(m_\pi, q^2)$$

which vanish for $m_\pi \to 0$, show up at a level of 10 to 30 % at the most. The prospects were much worse for the corrections to the longitudinal multipoles L_{0+}, and at that time, this triggered further experimental efforts to accurately separate the electro-production cross-sections at threshold and extract $G_A(q^2)$ from the transverse part.

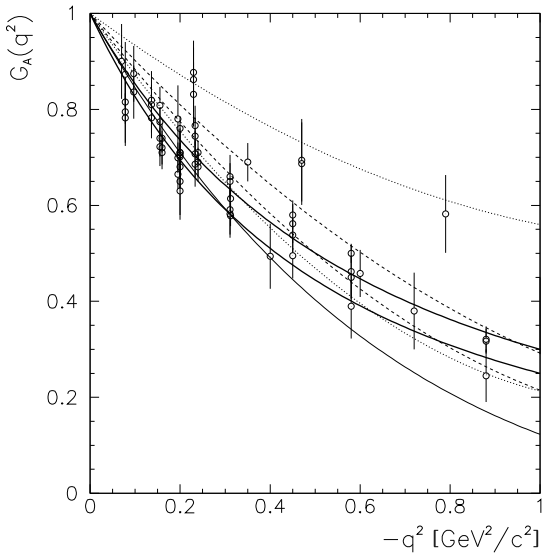

Figure 5.1: Available experimental data for $G_A(q^2)$, extracted from pion electro-production experiments in the vicinity of the pion production threshold. Note that in experiments where more theoretical models (FPV, BNR, DR) were used to extract G_A, all results are shown in the figure. The curves show predictions of some of the quark models: MIT bag model or the Cloudy bag model (thin full curve), model with a confining potential of the form $\sim r^3$ without CMS corrections (upper dashed line) and with CMS corrections (lower dashed line) [115], Skyrme model (upper dotted line), and Skyrme model with vector mesons (lower dotted line) [118, 119]. The upper and the lower thick full curves correspond to dipole parameterisations of $G_A(q^2)$ with $M_A = 1.10$ and $1.00\,\mathrm{GeV}$, respectively. Experimental data are from [26, 28, 29, 30, 31, 32, 33, 35, 37].

Sound objections to the FPV approach were risen by Benfatto, Nicolò, and Rossi (BNR), who claimed that the mass extrapolation of the amplitudes could not be trusted, and that the dis-

persive corrections do not necessarily remain small [80, 81]. To diminish the problem, they separated the total electro-production amplitude into a term that was expected to be well-behaved under mass extrapolation, and into a 'Born' term. For the first term, the FPV result was essentially kept, whereas the second term was fixed by gauge invariance. The drawback of the BNR theory, as pointed out by [117], was that in addition to the basic current algebra commutators, a specific phenomenological Lagrangian had to be chosen to describe the Born terms, where the pion charge form factor $F_\pi(q^2)$ had to be introduced.

Another approach was adopted by Dombey and Read (DR) [78, 79] who noted that the dispersion relations used in the description of pion electro-production were incompatible with the requirements of current algebra. Although it seems natural to expect that the threshold E_{0+} amplitude for charged pion electro-production can be identified with the s or u-channel nucleon pole terms, and hence depends on the proton charge form factor, current algebra asserts that the *axial* form factor is the most important. The mismatch could be traced back to the fact that dispersion calculations used the pseudo-scalar πNN coupling, whereas current algebra used the pseudo-vector coupling meeting the requirement of PCAC and directly leading to a contact (or *seagull*) term for $\gamma_v N \to N'\pi$ upon minimal substitution. This term could be identified with the part of the current algebra amplitude containing $G_A(q^2)$. The extrapolation from the soft-pion limit to the physical region occurs through this correspondence, and $G_A(q^2)$ remains the relevant form factor.

5.2 The DT model

The DT model of Drechsel and Tiator [38, 85] we used in the extraction of $G_A(q^2)$ from our experimental data is based on the effective Lagrangian models of [40, 41]. It is an earlier and simplified version of the unitary isobar model discussed in appendix E.

The electro-production amplitude is treated in two parts: the part which describes the coupling of the virtual photon to the nucleon or to the pion, and the part which describes the πNN vertex. The πNN vertex is more involved, since it embodies the strong interaction part of the electro-production process. At low energies, it can be well described by the pseudo-vector (PV) coupling

$$\mathcal{L}^{PV}_{\pi NN} = -\frac{f}{m_\pi}\overline{\psi}\gamma_5\gamma_\mu\boldsymbol{\tau}\partial^\mu\boldsymbol{\pi}\psi$$

which also reproduces PCAC and is consistent with the low-energy theorems and chiral perturbation theory [8] to the leading order. In the one-photon approximation, the total electro-production amplitude is a coherent sum of the non-resonant Born terms and the resonant terms with nucleon and meson resonances in the intermediate states (figure 5.2), where form factors are inserted at the photon-hadron vertices.

The problem is that the gauge invariance of the electro-magnetic current $q^\mu J_\mu = 0$, inherent to the PV coupling, can only be maintained if the pion and the axial-vector form factors are set equal to the Dirac isovector form factor, $G_A(q^2) = F_\pi(q^2) = F_1^v(q^2) \equiv 1/(1 - q^2/\Lambda_d^2)^2$. Insertion of form factors with different q^2-behaviours spoils the gauge invariance (i. e. the current conservation), and it is crucial to cure that. Gauge invariance can be restored by including additional gauge terms in the hadronic current

$$J^\mu \to J^\mu - \frac{q^\mu\, J\cdot q}{q^2}\,,$$

where the subtracted term is purely longitudinal since according to figure 2.2, $q = (\omega, 0, 0, |\mathbf{q}|)$. The subtraction effectively modifies only the longitudinal part of the cross-section and, corre-

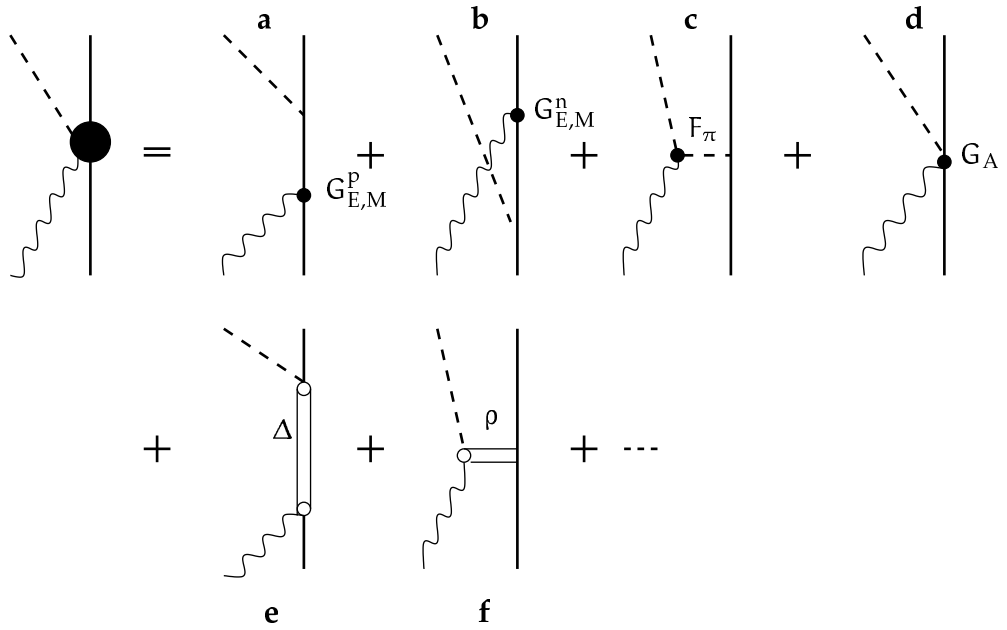

Figure 5.2: Decomposition of the total charged pion electro-production amplitude into non-resonant Born terms: **a** – s-channel term, **b** – u-channel term, **c** – t-channel (pion pole) term, **d** – contact (seagull) term, and resonant terms: **e** – s-channel Δ-exchange term, **f** – vector meson exchange term. The full circles in **a**, **b**, **c** and **d** indicate the insertions of the appropriate form factors, and ellipses stand for inclusions of higher resonances. The contact term containing the axial form factor $G_A(q^2)$ follows directly from the pseudo-vector coupling upon minimal substitution.

spondingly, influences the weight of the pion-pole term and the extracted value of Λ_π parameterising the monopole pion form factor

$$F_\pi(q^2) = 1/(1 - q^2/\Lambda_\pi^2) \,.$$

This procedure does not affect the transverse part of the cross-section. This allows us to apply form factors with different q^2-dependencies: we used the cut-off parameter of $\Lambda_d = 0.843\,\mathrm{GeV}$ for the dipole isovector Dirac form factors, whereas the cut-off parameters of the dipole $G_A(q^2)$ and of the monopole $F_\pi(q^2)$ form factors were fitted to the transverse and to the longitudinal cross-sections, respectively, as described on page 46. The Δ-resonance exchange term is by itself gauge-invariant, $q^\mu J^\Delta_\mu = 0$. In this sense, the parameterisation of the form factor of the $\gamma N\Delta$ vertex is irrelevant to the determination of $G_A(q^2)$.

The value of $d\sigma_T$ at $q^2 = 0$ was fixed by extrapolating our transverse cross-section (i. e. the $E_{0+}(n\pi^+)$ amplitude) to the photo-production angular distribution $d\sigma/d\Omega^\star_\pi$ at $\theta_\pi = 0°$. Due to the lack of reliable near-threshold data for charged pion photo-production, the multipole analyses maintained by the SAID group [99] (figure 5.3) are rather imprecise in this energy region and could not be used to this purpose. We used a value of 7.4 μb/sr, strongly favoured by the photo-production dispersion analysis of [101]. The corresponding value of E_{0+} is also well supported by the studies of the GDH sum rule [102] and by the Kroll-Ruderman theorem.

Due to the cancellations between the terms including only $l \geq 1$ partial waves and interference terms with the s-wave amplitude E_{0+}, the model transverse cross-section is predominantly sensitive to the $E_{0+}(n\pi^+)$ amplitude and therefore to $G_A(q^2)$ or, if the dipole parameterisation (1.1) is used, to M_A. In the case of the longitudinal cross-section, the sensitivity on the corresponding open quantity, the pion form factor, is more intricate. The s-waves contribute only 10 % to the longitudinal part, and the pion form factor appears only at the order of

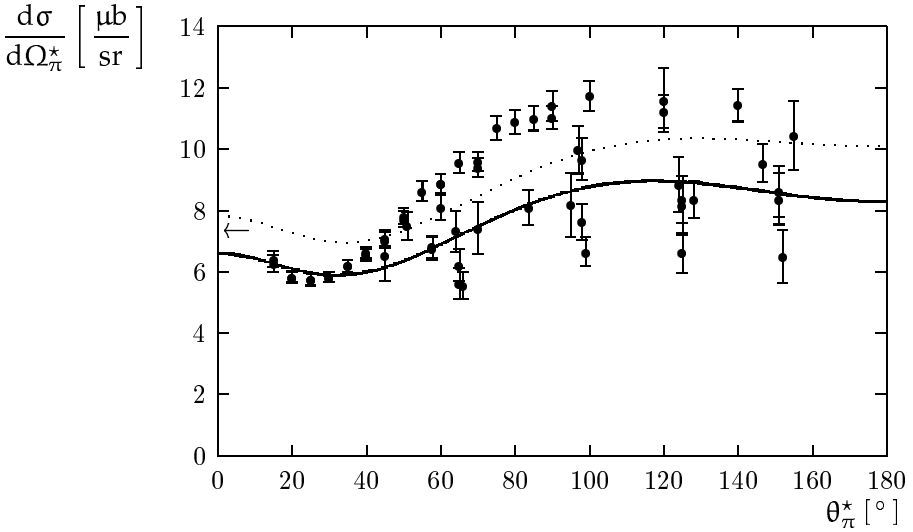

Figure 5.3: Determination of the transverse pion electro-production cross-section at the origin from pion photo-production data by extrapolating the multipole analyses of angular distributions to 0°. Only those entries of the SAID database [99] corresponding to $1100\,\text{MeV} < W < 1150\,\text{MeV}$ were used. The full curve is the result of the SAID multipole analysis, and the dotted curve is the prediction of the DHKT model described in appendix E. Note, however, that the SAID result was not used in our analysis for lack of reliable data and systematical uncertainties of the SAID multipole analysis in the threshold region (e. g. questionable treatment of multipoles in the vicinity of the charged and neutral pion thresholds). The value of $d\sigma(0) = 7.4\,\mu b/sr$ we used was obtained from the multipole analyses of [101] and is indicated by the arrow.

$\mathcal{O}(\mu^2, \mu q^2/M^2)$ in the $L_{0+}(n\pi^+)$ amplitude. However, the complete $d\sigma_L$ containing also higher partial waves is quite sensitive to $F_\pi(q^2)$ and to the corresponding cut-off parameter Λ_π. As the higher partial waves are not well known yet, and since restoring the gauge invariance of the model involves the longitudinal part of the current, the analysis of the pion form factor can not be as reliable as the one of the axial form factor. The results of the model fit to the experimental data have been presented already at the end of chapter 4.

5.3 Chiral perturbation theory

Chiral perturbation theory (χPT) is one of the most elaborated low-energy effective field theories approximating QCD in its low-energy domain, where colour confinement makes the hadrons, not quarks and gluons, the relevant and in fact the only observable degrees of freedom [8]. In this regime, the existence of pions (and other Goldstone bosons) reflects the spontaneous symmetry breaking of the vacuum, and the pions provide the connection to QCD. Since the interaction of the Goldstone bosons is weak at low energies, the observables can be calculated perturbatively using an expansion in small masses and momenta. Comparing the results of our measurements with the predictions of χPT would be a most important test of the theory.

Regrettably, the four-momentum transfers as well as the invariant mass in our $p(e, e'\pi^+)n$ experiment were still too high for its currently developed abilities. However, the difference in the axial mass parameter ΔM_A confirmed by our measurement can nevertheless be used to test the χPT through its prediction for the threshold s-wave amplitude E_{0+}. The crucial feature of the χPT applied here is that corrections to the amplitude in the chiral limit ($m_\pi = 0$) can be calculated systematically and model-independently, thus avoiding all obstacles and pitfalls of mass extrapolation in the FPV, BNR and DR models.

The χPT asserts that already at the order of $\mathcal{O}(q^2)$, the NLS result for the threshold amplitude (5.1) *has to be* updated due to processes involving pion loops [82]. Contrary to the case of the Goldberger-Treiman discrepancy discussed in section 2.2, these contributions do not vanish, and generate a new q^2-dependent term in the isospin-odd electric dipole amplitude

$$E_{0+}^{(-),\chi PT}(m_\pi, q^2) = \frac{eg_A}{8\pi f_\pi}\left\{1 + \frac{q^2}{6}\langle r_A^2\rangle + \frac{q^2}{4M^2}\left[\kappa_v + \frac{1}{2}\right] + \frac{q^2}{128 f_\pi^2}\left[1 - \frac{12}{\pi^2}\right] + \mathcal{O}(p^3)\right\}, \quad (5.3)$$

where p is a generic small momentum or meson mass. For transparency, chiral logarithm terms of the order of $\mathcal{O}(m_\pi^2, \ln m_\pi^2)$ and a recoil correction $-m_\pi/M$ were left out in this expression, since they play a minor role in determining $G_A(q^2)$. Also note that the isovector anomalous magnetic moment κ_v appears in (5.3) and in (5.1) instead of the q^2-dependent magnetic form factor, since in the consistent chiral power-counting of the χPT, these form factor effects are of the order of $\mathcal{O}(q^3)$ and have to be dropped.

One has to be aware of the fact that the new $q^2(1 - 12/\pi^2)/128 f_\pi^2$ term is a genuine one-loop contribution that can not be cancelled by higher loop contributions, and that this result is completely model-independent. Higher loop corrections are suppressed by powers of m_π/M and $m_\pi^2/16\pi^2 f_\pi^2$ and are expected to be small (however, investigations concerning this point are underway [8]). At any rate, the $\mathcal{O}(q^2)$ correction has an important consequence for the extraction of r_A from pion electro-production data. It effectively reduces the mean-square axial radius,

$$\langle r_A^2\rangle \to \langle r_A^2\rangle + \frac{3}{64 f_\pi^2}\left(1 - \frac{12}{\pi^2}\right). \quad (5.4)$$

The correction term in (5.4) has a value of $-0.046\,\mathrm{fm}^2$, which is a $-10\,\%$ correction to a typical value of $\langle r_A^2\rangle = 0.45\,\mathrm{fm}^2$. Correspondingly, the axial mass $M_A = \sqrt{12}/\langle r_A^2\rangle^{1/2}$ would appear to be about 5 % larger in electro-production than in neutrino scattering, in agreement with the observed ΔM_A.

6

Calculation of the nucleon axial form factor

In the discussion of any scattering of relativistic electrons off the nucleon as a composite hadronic system, the structure of the nucleon plays a crucial role. In fact, the corresponding point-interaction currents are modified. A simple and direct, yet fruitful, way to circumvent the explicit consideration of the effect is to introduce *form factors* multiplying various components of these currents. For example, the electro-magnetic form factors obtained in elastic electron scattering (or their equivalents, the electro-magnetic root-mean-square radii) reveal that the nucleons have a finite extension. Similarly, in the analysis of our measured data from $p(e, e'\pi^+)n$, we determined the q^2-dependence of one of the less known form factors, called the *axial form factor*, which carries the information about the structure of the nucleon axial-vector current.

Determination of the form factors in an explicit microscopical approach is, however, a theoretical task which generally requires quite complicated techniques. Prompted in addition by the 'axial mass discrepancy' discussed in section 2.2, we were motivated to calculate the axial form factor $G_A(q^2)$ in the framework of two chiral soliton models of the nucleon which are of our special interest: the linear σ-model (LSM) and the chromodielectric model (CDM). The LSM is characterised by an extraordinary strong pion cloud surrounding the valence quark core, while a prominent feature of the CDM is a QCD-inspired, dynamically generated binding field for quarks.

Since similar technical issues emerge in the evaluation of the axial coupling constant g_A (which is nothing but the axial form factor taken at $q^2 = 0$), the first part of this chapter is dedicated to g_A and reviews some common theoretical concepts and models used to calculate it, while the second part concentrates on the calculation of $G_A(q^2)$ in the LSM and the CDM, taking care of the proper consideration of centre-of-mass and recoil corrections.

6.1 The axial-vector coupling constant

6.1.1 g_A in the NRQM

The axial coupling constant g_A of the nucleon $|N\rangle$ can be defined by

$$g_A \langle N | \sigma^N \tfrac{1}{2}\tau_3^N | N \rangle = \int d^3\mathbf{r} \left\langle \{3q\}_N \middle| \hat{\mathbf{A}}^3(0,\mathbf{r}) \middle| \{3q\}_N \right\rangle , \tag{6.1}$$

where $\hat{A}^{\mu j}(x) = \overline{\psi}(x)\gamma^\mu\gamma_5\frac{1}{2}\tau_j\psi(x)$ is the quark-level axial current operator, σ and τ are the usual Pauli matrices, and $|\{3q\}_N\rangle$ is the three-quark nucleon wave-function, generally formed from space, isospin, spin, and colour parts. In the non-relativistic constituent quark model

(NRQM), the matrix element on the RHS of (6.1) is evaluated between states represented by free, plane-wave Dirac spinors, in the non-relativistic limit, so (6.1) reduces to

$$g_A \langle N | \sigma^N \tau_3^N | N \rangle = \left\langle \{3q\}_N \left| \sum_{i=1}^{3} \sigma(i)\tau_3(i) \right| \{3q\}_N \right\rangle ,$$

where on the LHS, the spin and isospin operators act on nucleonic degrees of freedom and on the RHS, on the quark degrees of freedom. Since the total spin-isospin wave-function $|\{3q\}_N\rangle$ is symmetric with respect to an interchange of any two quarks, the expectation value can be calculated only for one quark and multiplied by 3. For $|\{3q\}_N\rangle = |p\uparrow\rangle$, we get $g_A \cdot 1 = 3 \cdot \frac{5}{9}$ or

$$g_A^{NRQM} = \frac{5}{3} , \tag{6.2}$$

about 32% above the current average experimental value of $g_A(0) = 1.2670 \pm 0.0035$ [25].

6.1.2 g_A in the MIT bag and in models with a scalar confining potential

In the MIT bag model [104, 105], the $\psi(x)$ represents the solution of the Dirac equation for a massless quark moving freely in an infinitely deep, spherically symmetric potential well (also called a *bag*) of radius R. With

$$\psi(x) = \frac{1}{\sqrt{4\pi}} \begin{pmatrix} f(r) \\ i\sigma\hat{r}g(r) \end{pmatrix} \xi_{\text{spin-isospin}} ,$$

the solutions for components are $f(r) = \mathcal{N} E j_0(Er)$ and $g(r) = -\mathcal{N} E j_1(Er)$, where $\mathcal{N}$ is the normalisation constant fixed by the conservation of probability, $\int_0^R (f^2 + g^2)\, r^2\, dr = 1$. In the lowest quark radial state, $E = E_0$ with $\omega_0 \equiv E_0 R \simeq 2.0428$. The axial current $\hat{A}^{\mu j}(x) = \overline{\psi}(x)\gamma^\mu\gamma_5 \frac{1}{2}\tau_j \psi(x)\Theta(R - r)$ differs from zero only in the interior of the bag, and we get

$$g_A^{MIT} = \frac{5}{3}\int_0^R dr\, r^2 \left[f^2(r) - \frac{1}{3} g^2(r) \right] = \frac{5}{9}\frac{\omega_0}{\omega_0 - 1} \simeq 1.09 , \tag{6.3}$$

about 14% below the experimental value. Models with confining potentials (or, equivalently, with the mass term $M(r)$) of the form $M(r) = Cr^n$ and the integration range correspondingly extended to ∞, give values remarkably close to the experimental value: $n = 2$ gives $g_A = 1.26$ and $n = 3$ gives $g_A = 1.21$ [106].

One of the inherent difficulties in the calculation of g_A in the framework of quark models is the *spurious centre-of-mass motion*. But with the exception of the non-relativistic version of the harmonic oscillator quark model, the centre-of-mass motion can not be explicitly separated from the relative motion of the quarks, and corrections are mostly only approximate. Centre-of-mass corrections to the order of $\mathcal{O}(p^2)$ can be incorporated into the MIT bag model or into any relativistic quark model invoking Dirac-like wave-functions containing upper and lower components f and g by using the wave-packet formalism suggested in [107]. For the matrix element of the $n \to p$ axial-vector transition current one obtains

$$g_A^{MIT,\mathcal{O}(p^2)} \left[1 - \frac{\langle \mathbf{p}^2 \rangle}{3 m_n m_p} \left(\frac{1}{4} + \frac{3}{8}\frac{m_n}{m_p} + \frac{3}{8}\frac{m_p}{m_n} \right) \right] = \frac{5}{3}\int_0^R dr\, r^2 \left[f^2(r) - \frac{1}{3} g^2(r) \right]$$

instead of (6.3), where typical $\langle \mathbf{p}^2 \rangle$ is of the order of $0.1\,\text{GeV}^2$. The problem in this procedure is that once a certain momentum $\mathbf{P}$ is projected out of the three-quark wave-function $|\mathbf{p}_1\mathbf{p}_2\mathbf{p}_3\rangle$

[108], the resulting wave-function does become translationally invariant in the sense that the centre-of-mass moves as an $\exp(i\mathbf{P}\mathbf{r})$ plane wave, but the Lorentz invariance, and therefore the conservation of the electro-magnetic current, are spoiled. The reason is that the lower spinor components are not treated properly by such projection. The technique is therefore limited to conditions in which the nucleon as a whole moves non-relativistically, i. e. to cases where $|\mathbf{P}|^2 \ll 4M^2$. In the quark model with the $M(r) = Cr^n$ scalar potential, the centre-of-mass corrections yield $\Delta g_A = -0.05$ for the quadratic and $\Delta g_A = -0.06$ for the cubic potential [106].

6.1.3 The role of pions in g_A

Apart from the problems inherent to the linear momentum projection, the potential quark models suffer from another serious drawback. Models in which relativistic quarks are bound only by a scalar field violate the chiral symmetry of QCD for massless quarks. As a single quark reflects at the bag boundary, its momentum reverses sign, whereas its spin remains unchanged, i. e. the quark wave-function is not an eigenfunction of helicity [5]. In other words, the solution of the equation of motion does not reflect the chiral symmetry of the underlying Lagrangian. The extent to which chiral symmetry is broken is measured by the divergence of the quark axial current

$$\partial_\mu \widehat{A}^{\mu j}(x) = \partial_\mu \left[\overline{\psi}(x)\gamma^\mu\gamma_5 \frac{\tau_j}{2}\psi(x) \right] = \begin{cases} i\overline{\psi}\gamma_5\tau_j\psi\, \frac{1}{2}\delta(R-r) & \text{(MIT bag model)}, \\ i\overline{\psi}\gamma_5\tau_j\psi\, M(r) & \text{(scalar confining potential)}, \end{cases}$$

where j is the isospin index. In *chiral bag models*, in which the interior and the exterior of the bag maintain two distinct realisations of chiral symmetry, the non-vanishing divergence of the axial current is interpreted as the source function of the pion field. The pions compensate the helicity change of the quarks impinging on the bag boundary, and are therefore a vital ingredient of these models, restoring the chiral symmetry of the original Lagrangian. The pion field is introduced phenomenologically as an elementary field, without any reference to its quark-antiquark structure.

In the earlier versions of chiral bag models, the pions appear exclusively outside the bag [109, 110, 111] and couple to the quarks only at the bag's surface. The 'pionised' varieties of the model with a scalar confining potential [106] or various versions of the *cloudy bag model* (CBM) [112, 113, 114] eliminate this unnatural division and allow the pions and quarks to interact throughout the object's volume. The flow of the axial-vector current continues at the boundary of the quark core, and contains the additional pion contribution

$$\widehat{A}^{\mu j}(x) = \overline{\psi}(x)\gamma^\mu\gamma_5\tfrac{1}{2}\tau_j\psi(x)M(r) + f_\pi\partial^\mu\pi_j(x) \tag{6.4}$$

(for the CBM, $M(r)$ is replaced by $\Theta(R-r)$). The pion field satisfies the Klein-Gordon equation in which the divergence of the axial current of the quark core acts as the source term

$$(\nabla^2 - m_\pi^2)\,\pi_j(\mathbf{r}) = \frac{M(r)}{f_\pi}\, i\overline{\psi}(r)\gamma_5\tau_j\psi(\mathbf{r}),$$

and where the operators of $\pi_j(\mathbf{r}) = -\boldsymbol{\sigma}\hat{\mathbf{r}}\,\tau_j\,\phi(r)$ (the role of the $\boldsymbol{\sigma}\hat{\mathbf{r}}$ operator is to endow the pion field operator with a negative parity) should be taken between nucleon spin and isospin states. For small r, $\phi(r)$ is linear in r, whereas asymptotically, it is given by the Yukawa form

[5] In the MIT bag model, for instance, the confining boundary condition requires that $\overline{\psi}\psi = 0$ and $n_\mu\overline{\psi}\gamma^\mu\psi = 0$ at the bag boundary, where n_μ is an outward normal four-vector.

$\phi(r) \sim (1+m_\pi r)\exp(-m_\pi r)/r^2$. This has an important consequence for the pionic contribution to the axial coupling constant defined by

$$g_A^{(\pi)} \langle N | \sigma^N \tfrac{1}{2}\tau_3^N | N \rangle = f_\pi \int d^3\mathbf{r} \langle N | \nabla [\boldsymbol{\sigma}\hat{\mathbf{r}}\phi(r)] \boldsymbol{\tau} | N \rangle ,$$

analogously to (6.1). Using the identity $\nabla [\boldsymbol{\sigma}\hat{\mathbf{r}}\phi(r)] = \hat{\mathbf{r}}(\boldsymbol{\sigma}\hat{\mathbf{r}})\phi'(r) + [\boldsymbol{\sigma} - \hat{\mathbf{r}}(\boldsymbol{\sigma}\hat{\mathbf{r}})]\phi(r)/r$ we obtain the surprising result

$$\begin{aligned} g_A^{(q)} &= g_A^{(q),\,MIT} , \\ g_A^{(\pi)} &= \frac{5}{3}\frac{8\pi}{3} f_\pi \int_0^\infty dr\, r^2 \left[\phi'(r) + \frac{2\phi(r)}{r} \right] = \frac{5}{3}\frac{8\pi}{3} f_\pi\, r^2 \phi(r) \Big|_0^\infty = 0 , \end{aligned}$$

i. e. the g_A is determined by the quark core alone, whereas the pionic contribution is zero due to the vanishing of the pion field at $r = 0$ and $r = \infty$ (the same argument applies to the CBM, with $f(r)$ and $g(r)$ in the quark part replaced by $j_0(\omega_0 r/R)$ and $j_1(\omega_0 r/R)$, respectively). The reason for this behaviour is the linear dependence of the axial current (6.4) on the pion field $\pi(x)$. Higher-order corrections in powers of π are expected to be small: for instance, if the Weinberg representation of the pion field [115] $\boldsymbol{\pi} \to \boldsymbol{\pi}/(1 + \boldsymbol{\pi}^2/f_\pi^2)^{-1/2}$ is used and the corresponding pion part of the axial current

$$\hat{A}^{\mu j\,(\pi)}(x) = \frac{f_\pi}{1 + \boldsymbol{\pi}^2/f_\pi^2}\, \partial^\mu \pi_j(x)$$

is expanded in terms of $\boldsymbol{\pi}$, the contribution of the π^3 term to $g_A^{(\pi)}$ turns out to be negligible. The situation is essentially different in models in which the $f_\pi \partial^\mu \pi_j(x)$ term in the axial current is replaced by $\sigma(x)\partial^\mu \pi_j(x) - \pi_j(x)\partial^\mu \sigma(x)$, where $\sigma(x)$ is allowed to vary in space. In these *chiral soliton models* the nucleon is described in terms of a quark core coupled to the meson cloud in which the σ and the π fields appear symmetrically as chiral partners. In the chiral soliton models, the basic ingredients are represented by interacting dynamical fields constrained by the equations of motion, contrary to the potential models in which parameters are fixed in advance. One of the prices we have to pay for this liberty is the value of g_A which generally overestimates the experimental value, typically by 30 or 40 %.

6.1.4 g_A in the LSM and the CDM

The constraints of chiral symmetry in the world of hadrons composed of light quarks have a firm theoretical and phenomenological background. If the masses of the u and d quarks were zero, the left-handed and right-handed components of the quark fields in QCD would decouple and maintain separate 'left' and 'right' invariances, and QCD would possess a *chiral* $SU(2)_L \times SU(2)_R$ (or, equivalently, $SU(2)_V \times SU(2)_A$) symmetry [6]. Even with the $m_u = m_d \neq 0$, the chiral SU(2) remains a fairly accurate symmetry of QCD, which nevertheless does not emerge in the energy spectrum of the physical hadrons: there is no parity doubling among the lowest-lying hadron states. What we do observe is that the masses in the multiplets (e. g. of (π^+, π^0, π^-) or (p, n) are nearly equal. We can therefore conclude that the chiral SU(2) is *broken* to the vectorial isospin $SU(2)_V$ (in other words, the $SU(2)_A$ remains *hidden*).

The LSM and the CDM are characteristic representatives of phenomenological quark soliton models of the nucleon implementing the concept of chiral symmetry and containing the

[6] With the inclusion of the s quarks, these extend to $SU(3)_L \times SU(3)_R$ or $SU(3)_V \times SU(3)_A$.

mechanism of its breakdown at the quark level (see appendix F for the basics of the models). In these models, the nucleon is described in terms of a core consisting of three u/d valence quarks coupled to σ-meson and pion fields. The axial current operator has the form

$$\hat{A}^{\mu j}(x) = \sum_a \overline{\psi}_a(x)\gamma^\mu\gamma_5\tfrac{1}{2}\tau_j\psi_a(x) + \sigma(x)\partial^\mu\pi_j(x) - \pi_j(x)\partial^\mu\sigma(x)\,, \tag{6.5}$$

where $\psi(x)$ are the quark spinors and the $\sigma(x)$ and the $\pi(x)$ fields represent the σ-mesons and pions. Only quarks in the lowest radial mode with $l = 0$ and with a particular spin-isospin combination $(|u\downarrow\rangle - |d\uparrow\rangle)/\sqrt{2}$ are considered, and the mesons are introduced in terms of coherent states (see appendix G for details).

In the LSM and the CDM, the model states $|\psi_{hh}\rangle = |B\rangle \otimes |\Sigma\rangle \otimes |\Pi\rangle$ ('hh' stands for 'hedgehog') in which the bare quark core $|B\rangle$ is coupled to the cloud of σ-mesons $|\Sigma\rangle$ and pions $|\Pi\rangle$ (see (G.5)), do not correspond to physical states, since spin and isospin are not good quantum numbers: the meson part of the baryon wave-function is a superposition of the meson vacuum and components with one, two, or more mesons, and the quark part is also a superposition of a three-quark state with the quantum numbers of the nucleon, and the three-quark state with the quantum numbers of the Δ. In other words, the model wave-function emerges as a soliton which is neither an eigenstate of angular momentum nor isospin, and therefore breaks the rotational (spin and isospin) invariance of the Lagrangian. Although the expectation value of the angular momentum operator $\hat{J}$ between hedgehog states vanishes, we have

$$\langle\psi_{hh}| : \hat{J}^2 : |\psi_{hh}\rangle \neq 0\,.$$

The *physical* model states of the nucleon and the Δ can be derived from the model states $|\psi_{hh}\rangle$ by means of the Peierls-Yoccoz projection [116]

$$|JTMM_T\rangle = \hat{P}^{JT}_{MM_T}|\psi_{hh}\rangle\,,$$

where $\hat{P}^{JT}_{MM_T}$ is the projection operator yielding a state of definite spin and isospin. Because of the grand-spin symmetry of the hedgehog state (see appendix G), only one of the projections onto spin J or isospin T is sufficient, since a projection onto J automatically projects also onto $T = J$, and vice versa. The projector which projects a state with angular momentum J and isospin $T = J$ from the hedgehog is given by

$$\hat{P}^{JT}_{MM_T} = (-1)^{J+M_T}\frac{2J+1}{8\pi^2}\int d^3\Omega\, \mathcal{D}^{*J}_{M,-M_T}(\Omega)\,R(\Omega)\,, \tag{6.6}$$

where $\Omega = (\alpha,\beta,\gamma)$ are the Euler angles, $\mathcal{D}^J_{M,K}(\Omega)$ are the Wigner functions and $R(\Omega)$ is the rotation operator. We consider only states with $M = -M_T$ and use the shorthand notation $\hat{P}^{JJ}_{M,-M} \equiv \hat{P}_{JM}$, where $\hat{P}^{JJ\dagger}_{M,-M} = \hat{P}^{JJ}_{-M,M}$. The projected baryon states obtained in this projection can now be used in the calculation of physical observables. The expectation value corresponding to an arbitrary operator $\hat{\mathcal{O}}$ is

$$\langle JTMM_T|\,\hat{\mathcal{O}}\,|JTMM_T\rangle = \langle\psi_{hh}\hat{P}^\dagger_{JM}\,|\,\hat{\mathcal{O}}\,|\,\hat{P}_{JM}\psi_{hh}\rangle\,.$$

Thus to calculate g_A in the LSM or the CDM, one has to evaluate the expectation value of (6.5) between nucleon states, i. e.

$$g_A = 2\int d^3\mathbf{r}\left\langle \tfrac{1}{2}\tfrac{1}{2}\tfrac{1}{2}\tfrac{1}{2}\right| : \hat{A}^{33}(\mathbf{r}) : \left|\tfrac{1}{2}\tfrac{1}{2}\tfrac{1}{2}\tfrac{1}{2}\right\rangle.$$

In both models, the resulting expressions for the quark and the pion contribution to the axial coupling constant have the same algebraic form

$$g_A^{(q)} = \left[\frac{5}{3} - \frac{4N_\pi}{27}\left(2 - \frac{F_{3/2}}{F_{1/2}}\right)\right] \int dr\, r^2\, (u^2 - \tfrac{1}{3}v^2)\,, \tag{6.7}$$

$$g_A^{(m)} = -\frac{16\pi}{9} \int dr\, r^2\, \phi \frac{d\sigma}{dr}\,, \tag{6.8}$$

where N_π is the calculated number of pions before the projection and $F_{1/2}$ and $F_{3/2}$ are the overlaps of the unprojected and the projected nucleon states (see appendix G). The factors in front of the integrals originate in the spin/isospin structure of the model wave-function and are fixed. The radial functions $u(r)$, $v(r)$, $\sigma(r)$ and $\phi(r)$ (see (G.1), (G.3) and (G.4) for their definitions) depend on the choice of the quark-meson coupling constant g, and are determined variationally. In the LSM, a typical result with $g = 5.0$ is $g_A = g_A^{(q)} + g_A^{(m)} = 0.961 + 0.823 = 1.783$. In the CDM, where the pion field is relatively weak since the quarks are basically bound by the χ field alone, we obtain $g_A = g_A^{(q)} + g_A^{(m)} = 1.270 + 0.232 = 1.502$ with a typical coupling constant of $\sqrt{g m_\chi} = 0.2\,\mathrm{GeV}$.

6.2 Definition of $G_A(q^2)$

Formally, the axial-vector form factor is defined as the coefficient of the axial-vector term in the general Lorentz decomposition [7] of the matrix element

$$\langle N_f(p_f)\,|\,\hat{\mathbf{A}}^j(0)\,|\,N_i(p_i)\rangle = \overline{u}_f(p_f)\left[G_A(q^2)\,\boldsymbol{\gamma} + \frac{G_P(q^2)}{2M}\,\mathbf{q} + \frac{G_T(q^2)}{2M}\sum_{i=1}^{3} i\sigma^{i\nu} q_\nu \hat{\boldsymbol{e}}_i\right]\gamma_5 \frac{\tau_j}{2}\, u_i(p_i)$$

of the space part of the axial-vector current $\mathbf{A}^j$, where j is the isospin index, $q = p_i - p_f$ is the four-momentum transfer, and the spinors u_i and u_f satisfy the Dirac equation. Here $G_A(q^2) = g_A(q^2)/g_A(0)$ is the *axial-vector* form factor, $G_P(q^2)$ is the *induced pseudo-scalar*, and $G_T(q^2)$ is the *pseudo-tensor* form factor (see also appendix A). Requiring that the axial current is Hermitian and that its matrix element is invariant with respect to time reversal, we get $G_T = 0$. This equation is the starting point for all model calculations of the axial form factor: its RHS is fixed by the Lorentz and Dirac properties of the nucleon spinors, whereas the model wave-functions and the model axial current operator enter on its LHS.

6.3 $G_A(q^2)$ in the MIT bag and in models with a scalar confining potential

For a nucleon consisting of a core of three point-like u and d quarks confined in a scalar potential, expression (6.3) can easily be generalised to $q^2 \neq 0$. Without centre-of-mass corrections, we obtain

$$G_A(q^2) = \frac{5}{3}\int_0^\infty dr\, r^2 \left[j_0(qr)\left[f^2(r) - g^2(r)\right] + \frac{2j_1(qr)}{qr} f^2(r)\right],$$

where $f(r)$ and $g(r)$ are the upper and lower components of the spinor that solves the Dirac equation for massless quarks in the confining potential $M(r)$. In the MIT bag model where the

[7] It can be shown [121] that 12 different independent Lorentz axial-vectors can be constructed from the pertaining four-vectors $q = (p_i - p_f)$ and $(p_i + p_f)$, and from the matrices γ^μ, γ_5 and $\sigma^{\mu\nu} \equiv (i/2)\,[\gamma^\mu, \gamma^\nu]$. Using the properties of the γ-matrices and the Dirac equation, the number of independent axial-vectors reduces to 3: $\boldsymbol{\gamma}\gamma_5$, $\mathbf{q}\gamma_5$ and $\sigma^{i\nu} q_\nu \hat{\boldsymbol{e}}_i$, which are also used here (see also (A.1)).

single quark wave-function is completely determined by its eigenenergy ω_0 (and also in the CBM, where the same holds and where the pion contribution to $G_A(q^2)$ vanishes just as it did in g_A), the result is even simpler

$$G_A(q^2) = \frac{3}{2}\frac{1}{j_0^2(\omega_0)}\int_0^R dr\, r^2 \left[j_0(qr)\left[j_0^2(x) - j_1^2(x)\right] + \frac{2j_1(qr)}{qr}\, j_1^2(x)\right],$$

where $x = \omega_0 r/R$. Attempts to eliminate the centre-of-mass motion and to account for recoil effects in $G_A(q^2)$ face the same problems as for the g_A. When corrections are applied [115], the general trend is to bring the calculated q^2-dependence into a much better agreement with the experiment (see figure 5.1).

6.4 $G_A(q^2)$ in the LSM and the CDM

The most convenient reference frame to calculate the nucleon form factors in the LSM and the CDM is the hadron Breit frame in which the momenta of the target and the recoil nucleon are anti-parallel and equal in magnitude,

$$\begin{aligned} p_i &= (E, -\tfrac{1}{2}\mathbf{q}), \\ p_f &= (E, +\tfrac{1}{2}\mathbf{q}), \\ E &= (\tfrac{1}{4}|\mathbf{q}|^2 + M^2)^{1/2}, \end{aligned}$$

and therefore $q = (0, \mathbf{q})$, i. e. the energy transfer is zero and $q^2 = -|\,\mathbf{q}\,|^2$. In this frame, the general expression for the axial current matrix element reduces to

$$\langle N_f(\tfrac{1}{2}\mathbf{q})\,|\,\hat{\mathbf{A}}^j(0)\,|\,N_i(-\tfrac{1}{2}\mathbf{q})\rangle = \chi_f^\dagger \left\{ \frac{E}{M}\boldsymbol{\sigma}_T\, G_A(q^2) + \left[G_A(q^2) - \frac{|\mathbf{q}|^2}{4M^2}\, G_P(q^2)\right]\boldsymbol{\sigma}_L \right\} \frac{\tau_j}{2}\,\chi_i\,, \quad (6.9)$$

where $\boldsymbol{\sigma}_L = \hat{\mathbf{q}}(\boldsymbol{\sigma}\hat{\mathbf{q}})$, $\boldsymbol{\sigma}_T = \boldsymbol{\sigma} - \hat{\mathbf{q}}(\boldsymbol{\sigma}\hat{\mathbf{q}})$, and $\hat{\mathbf{q}} \equiv \mathbf{q}/|\mathbf{q}|$. We use the stationarity and the translational invariance of the current $\hat{A}^{\mu j}(0) = \exp(-ix\hat{P})\hat{A}^{\mu j}(x)\exp(+ix\hat{P})$ to get

$$\langle N_f(\tfrac{1}{2}\mathbf{q})\,|\,\hat{\mathbf{A}}^j(0)\,|\,N_i(-\tfrac{1}{2}\mathbf{q})\rangle = e^{iqr}\langle N_f(\tfrac{1}{2}\mathbf{q})\,|\,\hat{\mathbf{A}}^j(\mathbf{r})\,|\,N_i(-\tfrac{1}{2}\mathbf{q})\rangle\,.$$

The static approximation

The static approximation with $\frac{1}{2}|\mathbf{q}| \ll M$ is the easiest way to proceed [120]. Since the plane-wave states $|\,N(\mathbf{q})\rangle$ are normalised as

$$\langle N_f(\mathbf{q}')\,|\,N_i(\mathbf{q})\rangle = (2\pi)^3\delta^{(3)}(\mathbf{q}'-\mathbf{q})\,\frac{E}{M}\,\delta_{fi}\,,$$

whereas $\langle JTMM_T\,|\,JTMM_T\rangle = 1$, we can make the correspondence

$$|\,N(\mathbf{q})\rangle \simeq |\,N(0)\rangle \to [\,(2\pi)^3\delta^{(3)}(0)\,]^{1/2}\,|\,JTMM_T\rangle\,. \quad (6.10)$$

From (6.9) we then obtain

$$\langle \chi_f\,|\,\boldsymbol{\sigma}\tfrac{1}{2}\tau_3\,|\,\chi_i\rangle\,\frac{E}{M}G_A(q^2) = \int d^3\mathbf{r}\, e^{iqr}\left\langle JTMM_T\,\middle|\,\hat{\mathbf{A}}^j(\mathbf{r})\,\middle|\,JTMM_T\right\rangle. \quad (6.11)$$

Multiplying this expression from the left by $\hat{\mathbf{q}} \times (\hat{\mathbf{q}} \times$, expanding the exponential in terms of the spherical harmonics $\exp(i\mathbf{q}\mathbf{r}) = 4\pi \sum_{lm} i^l j_l(qr) Y_{lm}(\hat{\mathbf{r}}) Y^*_{lm}(\hat{\mathbf{q}})$ and then integrating over the directions of $\mathbf{q}$, we find

$$G_A(q^2) = \frac{2M}{E} \int d^3\mathbf{r} \left[j_0(|\mathbf{q}|r) \left\langle JTMM_T \right| : \hat{A}^{33}(\mathbf{r}) : \left| JTMM_T \right\rangle - \sqrt{2\pi}\, j_2(|\mathbf{q}|r) \left[Y_2 \otimes \left\langle JTMM_T \right| : \hat{\mathbf{A}}^3(\mathbf{r}) : \left| JTMM_T \right\rangle \right]_{10} \right] . \quad (6.12)$$

The second term in (6.12) is the zero component of a vector obtained by coupling the vector $\hat{\mathbf{A}}^3$ to the spherical harmonic of rank two. The bulk of the calculation is hidden in the evaluation of the expectation value of the space part of the axial current operator (6.5) between projected hedgehog states $|JTMM_T\rangle$, but can be done in a straightforward manner exploiting the properties of the hedgehog ansatz. The result for the axial form factor in the LSM or the CDM without centre-of-mass or recoil corrections finally is

$$G_A(q^2) = \frac{2M}{E} \int_0^\infty dr\, r^2 \left[j_0(qr) f_0(qr) + j_2(qr) f_2(qr) \right] ,$$

where $f_0 = f_0^{(q)} + f_0^{(m)}$, $f_2 = f_2^{(q)} + f_2^{(m)}$ and

$$\begin{aligned} f_0^{(q)} &= \left[\frac{5}{6} - \frac{2N_\pi}{27} \left(2 - \frac{F_{3/2}}{F_{1/2}} \right) \right] \left[u^2 - \frac{v^2}{3} \right] , \\ f_2^{(q)} &= \left[\frac{5}{6} - \frac{2N_\pi}{27} \left(2 - \frac{F_{3/2}}{F_{1/2}} \right) \right] \frac{2v^2}{3} , \\ f_0^{(m)} &= -\frac{4\pi}{9} \phi \frac{d\sigma}{dr} + \frac{4\pi}{9} \sigma \left(\frac{d}{dr} + \frac{2}{r} \right) \phi , \\ f_2^{(m)} &= -\frac{4\pi}{9} \phi \frac{d\sigma}{dr} + \frac{4\pi}{9} \sigma \left(\frac{d}{dr} - \frac{1}{r} \right) \phi , \end{aligned}$$

where $u(r)$ and $v(r)$ are the radial parts of the quark spinor and $\phi(r)$ and $\sigma(r)$ are the meson radial fields (see (G.1), (G.3) and (G.4) for their definitions). In the limit $q \to 0$, $j_0(qr) \to 1$, $j_2(qr) \to 0$, $E \to M$, and since the first and the second term of $f_0^{(m)}$ are equal, these results reduce to the expressions for the axial coupling constant (6.8).

Linear momentum projection

We saw in subsection 6.1.4 that the model state $|\psi_{hh}\rangle$ is not an eigenstate of angular momentum or isospin. Furthermore, the hedgehog soliton is a localised object and is therefore not an eigenstate of linear momentum either: even though $\langle \psi_{hh}| : \hat{\mathbf{P}} : |\psi_{hh}\rangle = 0$ due to the symmetry of the soliton, the expectation value of $\hat{P}^2$ differs from zero,

$$\langle \psi_{hh}| : \hat{\mathbf{P}}^2 : |\psi_{hh}\rangle \neq 0 ,$$

and breaks the translational invariance of the Lagrangian. Variational solutions therefore contain spurious centre-of-mass motion which contributes to the energy of the soliton and alters the 'intrinsic' values of the physical observables (for example, increases the charge radii) and, therefore, has to be eliminated. Moreover, treatment of recoil in the calculation of the axial form factor requires states of definite linear momentum. Below I describe how the translational and

rotational invariances of both models are restored in a combined spin/isospin-momentum projection procedure, following the computational techniques developed by [123], and present our calculation of $G_A(q^2)$ in which the centre-of-mass motion and recoil effects are excluded.

The projector which projects a state with angular momentum J and isospin $T = J$ from the hedgehog state (G.5) is given by (6.6). In turn, the linear momentum projector is given by

$$\widehat{P}_{\mathbf{q}} = \frac{1}{(2\pi)^3} \int d^3\mathbf{a}\, e^{i\mathbf{a}\mathbf{q}} \widehat{U}(\mathbf{a}) \,, \tag{6.13}$$

where $\widehat{U}(\mathbf{a}) = \exp(-i\mathbf{a}\widehat{\mathbf{P}})$ is the translation operator, $\mathbf{a}$ is the displacement vector and $\widehat{\mathbf{P}}$ is the operator of linear momentum. The physical nucleon at rest can be obtained by applying consecutively the spin/isospin projection operator and the projector onto linear momentum $\mathbf{q} = 0$ to the model wave-function $|\psi_{hh}\rangle$. Since $\widehat{P}_{JM}$ and $\widehat{P}_{\mathbf{q}=0}$ commute [122, 123], we have

$$|\, JJMM_T, \mathbf{q} = 0\rangle = \widehat{P}_{\mathbf{q}=0}\widehat{P}_{JM}\,|\,\psi_{hh}\rangle = \widehat{P}_{JM}\widehat{P}_{\mathbf{q}=0}\,|\,\psi_{hh}\rangle \,.$$

But to calculate physical observables free of centre-of-mass motion and recoil effects, the model states have to be eigenstates of angular momentum, isospin and of a *finite* linear momentum $\mathbf{q} \neq 0$. One way to achieve this is to boost the spin/isospin-eigenstate $\widehat{P}_{\mathbf{q}=0}\widehat{P}_{JM}|\psi_{hh}\rangle$ from its rest frame to a frame moving with a finite velocity. Such a fully relativistic, Lorentz-invariant boosting procedure which preserves the energy-momentum relation $E^2(\mathbf{q}) = M^2 + |\mathbf{q}|^2$ has been proposed and elaborated [124], but when applied to chiral solitons, its technical obstacles become prohibitive. We therefore approximated the exact boosting procedure by the Peierls-Yoccoz projection of a spin/isospin eigenstate $|\,JTMM_T\rangle$ onto $\mathbf{q} \neq 0$ using (6.13). Analogously to (6.10), the model wave-function is now given by

$$|\,N(\mathbf{q})\rangle \to [\,(2\pi)^3\delta^{(3)}(0)\,]^{1/2} \sqrt{\frac{E}{M}}\, \frac{\widehat{P}_{\mathbf{q}}|\,\psi_{JM}\rangle}{\langle \widehat{P}_{\mathbf{q}}\psi_{JM}|\,\widehat{P}_{\mathbf{q}}\psi_{JM}\rangle^{1/2}} \,, \tag{6.14}$$

where the square roots are just normalisation factors and $|\,\psi_{JM}\rangle \equiv |\,JTMM_T\rangle = \widehat{P}_{JM}|\psi_{hh}\rangle$. The angular and linear momentum projectors do not commute anymore, and their ordering as imposed in (6.14) should be respected. Furthermore, since the $\exp(-i\mathbf{a}(\mathbf{q} - \widehat{\mathbf{P}}))$-type of projection onto a finite momentum is not Lorentz-invariant, the energy-momentum relation now resembles the non-relativistic expansion of $E(\mathbf{q})$ and has the form

$$E(\mathbf{q}) = M + \frac{|\mathbf{q}|^2}{2M^*} + \mathcal{O}(q^4) \,,$$

where

$$M^* = \frac{3\int d^3\mathbf{a}\,\langle\psi_{hh}\,|\,\widehat{U}(\mathbf{a})\,|\,\psi_{hh}\rangle}{\int d^3\mathbf{a}\,a^2\,\langle\widehat{U}(-\tfrac{1}{2}\mathbf{a})\psi_{hh}\,|\,M - :\widehat{H}:\,|\,\widehat{U}(+\tfrac{1}{2}\mathbf{a})\psi_{hh}\rangle} \,.$$

The insertion of states with definite linear momenta takes place in the step preceding (6.12). Instead of $|\,JTMM_T\rangle$, the states (6.14) are plugged into (6.11). As it was done before, the resulting expression is multiplied from the left by $\hat{\mathbf{q}}\times(\hat{\mathbf{q}}\times$, the exponential is expanded in terms of the spherical harmonics, and we get

$$\begin{aligned}
G_A(q^2) &= -\frac{3}{8\pi}\frac{2M}{E}\frac{E}{M}\frac{1}{\mathcal{N}}\int d\hat{\mathbf{q}}\,\Big\langle \widehat{P}_{\mathbf{q}/2}\psi_{JT}\Big|\,\Big[\,\hat{\mathbf{q}}\times(\hat{\mathbf{q}}\times\hat{\mathbf{A}}^3(0))\,\Big]_3\,\Big|\,\widehat{P}_{-\mathbf{q}/2}\psi_{JT}\Big\rangle \\
&= -\frac{6}{8\pi}\frac{1}{\mathcal{N}}\int d^3\mathbf{b}'\,d^3\mathbf{b}\,d\hat{\mathbf{q}}\,\Big[\,\hat{\mathbf{q}}\times\Big(\hat{\mathbf{q}}\times\Big\langle\psi_{JT}\hat{U}^\dagger(\mathbf{b}')\hat{\mathbf{A}}^3(0)\hat{U}(\mathbf{b})\psi_{JT}\Big\rangle\Big)\,\Big]_3\, e^{i(\mathbf{b}+\mathbf{b}')\mathbf{q}/2} \\
&= -\frac{6}{8\pi}\frac{1}{\mathcal{N}}\int d^3\mathbf{b}'\,d^3\mathbf{b}\,d\hat{\mathbf{q}}\,\Big[\,\hat{\mathbf{q}}\times\Big(\hat{\mathbf{q}}\times\Big\langle\psi_{JT}\hat{\mathbf{A}}^3(\mathbf{b}')\hat{U}(\mathbf{b}-\mathbf{b}')\psi_{JT}\Big\rangle\Big)\,\Big]_3\, e^{i(\mathbf{b}+\mathbf{b}')\mathbf{q}/2} \,,
\end{aligned}$$

where we have used the relation

$$\hat{U}^\dagger(\mathbf{b}')\hat{\mathbf{A}}^3(0)\hat{U}(\mathbf{b}) = \hat{U}^\dagger(\mathbf{b}')\hat{\mathbf{A}}^3(0)\hat{U}(\mathbf{b}')\hat{U}^\dagger(\mathbf{b}')\hat{U}(\mathbf{b}) = \hat{\mathbf{A}}^3(\mathbf{b}')\hat{U}(\mathbf{b}-\mathbf{b}')$$

in the last step and where we have denoted $\mathcal{N} = \langle \hat{P}_{\mathbf{q}/2}\psi_{JT} \,|\, \hat{P}_{-\mathbf{q}/2}\psi_{JT}\rangle$. We now integrate over all directions of $\mathbf{q}$ and make the variable substitution $\mathbf{z} = \mathbf{b} - \mathbf{b}'$ and $\mathbf{y} = \mathbf{b}'$, so that $\mathbf{b} + \mathbf{b}' = 2\mathbf{y} + \mathbf{z}$. We get

$$\begin{aligned} G_A(q^2) = \frac{2}{\mathcal{N}}\Bigg[& \int d^3\mathbf{y}\, d^3\mathbf{z} \left\langle \psi_{JT} \,\middle|\, \hat{A}^{33}(\mathbf{y})\hat{U}(\mathbf{z}) \,\middle|\, \psi_{JT}\right\rangle j_0\Big(\Big|\, \mathbf{y} + \tfrac{1}{2}\mathbf{z} \,\Big|\, q\Big) \\ & - \sqrt{2\pi}\sum_m C^{10}_{2-m1m} \int d^3\mathbf{y}\, d^3\mathbf{z} \left\langle \psi_{JT} \,\middle|\, \hat{A}^{3m}(\mathbf{y}) Y_{2-m}(2\hat{\mathbf{y}} + \hat{\mathbf{z}})\hat{U}(\mathbf{z}) \,\middle|\, \psi_{JT}\right\rangle j_2\Big(\Big|\, \mathbf{y} + \tfrac{1}{2}\mathbf{z} \,\Big|\, q\Big)\Bigg]. \end{aligned}$$

The crucial step now is to commute the projector $\hat{P}^{JT}_{MM}$ contained in the spin/isospin-projected states $\langle\psi_{JT}| = \langle\psi_{hh}\hat{P}^{JT\dagger}_{MM}|$ to the right of the operator

$$\begin{aligned} \hat{\mathcal{A}}^{33}(\mathbf{y},\mathbf{z}) \equiv & \quad \hat{A}^{33}(\mathbf{y})\, j_0\Big(\Big|\, \mathbf{y} + \tfrac{1}{2}\mathbf{z} \,\Big|\, q\Big) \\ & - \sqrt{2\pi}\sum_m C^{10}_{2-m1m}\, \hat{A}^{3m}(\mathbf{y})\, Y_{2-m}(2\hat{\mathbf{y}} + \hat{\mathbf{z}})\, j_2\Big(\Big|\, \mathbf{y} + \tfrac{1}{2}\mathbf{z} \,\Big|\, q\Big), \end{aligned}$$

premonitioning the fact that the expectation values of the form

$$\langle \hat{U}(-\tfrac{1}{2}\mathbf{a})\psi_{hh} \,|\, \hat{A}^{3Q}(\mathbf{r}) \,|\, \hat{U}(\tfrac{1}{2}\mathbf{a})R(\Omega)\psi_{hh}\rangle$$

can be calculated for the hedgehog state in a relatively straightforward manner. In particular, they can be analytically integrated over the directions of $\mathbf{a}$ [123]. The commutation relation can be proven by expanding the spherical Bessel functions j_0 and j_2 in powers of their arguments $(z^2 + 4\mathbf{y}\mathbf{z} + 4y^2)$ and demonstrating that the integrals of the form

$$\int d^3\mathbf{y}\, d^3\mathbf{z}\, (z^2 + 4\mathbf{y}\mathbf{z} + 4y^2)^n\, [\,\hat{U}(\mathbf{z}), R(\Omega)\,]\, \hat{\mathcal{O}}(\mathbf{y})$$

and

$$\int d^3\mathbf{y}\, d^3\mathbf{z}\, (z^2 + 4\mathbf{y}\mathbf{z} + 4y^2)^n\, [\,\hat{U}(\mathbf{z}), R(\Omega)\,]\, Y_{2-m}(2\hat{\mathbf{y}} + \hat{\mathbf{z}})\, \hat{\mathcal{O}}(\mathbf{y})$$

vanish if operators $\hat{\mathcal{O}}$ possess certain tensorial properties. This was done by [123] for the case of the isoscalar component of the electro-magnetic current (which is a vector), but similar arguments apply to the axial current (which is a vector and isovector). So *under this particular integration*, we are allowed to commute rotation and translation operators even when $Y_{2-m}(2\hat{\mathbf{y}}+\hat{\mathbf{z}})$ is present. The angular momentum projector can then be commuted through $\hat{\mathcal{A}}^{33}$ using

$$\hat{P}^{JT}_{MM}\hat{\mathcal{A}}^{33}\,\hat{P}^{JT}_{MM} = \sum_{Q=-1}^{1} C_Q\, \hat{\mathcal{A}}^{3Q}\,\hat{P}^{JT}_{M-Q,M},$$

where

$$C_Q = (2T+1)\begin{pmatrix} T & 1 & T \\ -M & 0 & M \end{pmatrix}\begin{pmatrix} T & 1 & T \\ -M & Q & M-Q \end{pmatrix}.$$

Eliminating centre-of-mass motion and recoil effects

Reverting to the variables $\mathbf{a}$ and $\mathbf{r}$ using $\mathbf{b} = \mathbf{r} - \frac{1}{2}\mathbf{a}$ and $\mathbf{b}' = \mathbf{r} + \frac{1}{2}\mathbf{a}$, the expression for the axial form factor can be cast into the form

$$\begin{aligned} G_A(q^2) = \frac{2}{\mathcal{N}} \Bigg[& \sum_{Q=-1}^{1} C_Q \int d^3\mathbf{r}\, d^3\mathbf{a}\, d^3\Omega\, \mathcal{D}^{*\frac{1}{2}}_{\mp\frac{1}{2}-Q,\mp\frac{1}{2}}(\Omega)\, j_0(qr) \\ & \cdot \Big\langle \hat{U}(-\tfrac{1}{2}\mathbf{a})\psi_{hh} \Big| \hat{A}^{3Q}(\mathbf{r}) \Big| \hat{U}(\tfrac{1}{2}\mathbf{a})R(\Omega)\psi_{hh} \Big\rangle \\ & - \sqrt{2\pi} \sum_{Q=-1}^{1} C_Q \int d^3\mathbf{r}\, d^3\mathbf{a}\, d^3\Omega\, \mathcal{D}^{*\frac{1}{2}}_{\mp\frac{1}{2}-Q,\mp\frac{1}{2}}(\Omega)\, j_2(qr) \\ & \cdot \Big\langle \hat{U}(-\tfrac{1}{2}\mathbf{a})\psi_{hh} \Big| \Big[Y_2(\hat{\mathbf{r}}) \otimes \hat{\mathbf{A}}^{Q} \Big]_{10} \Big| \hat{U}(\tfrac{1}{2}\mathbf{a})R(\Omega)\psi_{hh} \Big\rangle \Bigg], \end{aligned} \tag{6.15}$$

where

$$\mathcal{N} = \int d^3\mathbf{a}\, d^3\Omega\, \mathcal{D}^{*\frac{1}{2}}_{\frac{1}{2},\frac{1}{2}}(\Omega)\, j_0\Big(\frac{qa}{2}\Big) \Big\langle \psi_{hh} \Big| \hat{U}(\mathbf{a})\, R(\Omega) \Big| \psi_{hh} \Big\rangle$$

and $\mathcal{D}$ are the usual Wigner functions. The $-$ signs in the $\mathcal{D}$-functions refer to the quark contribution, whereas the $+$ signs refer to the meson contribution. With the $(\mathbf{r}, \mathbf{a})$ notation, the formalism becomes more transparent: the elimination of the centre-of-mass motion and recoil is embodied in the centre-of-mass coordinate $\mathbf{r}$ and in the relative Breit coordinates $\pm\frac{1}{2}\mathbf{a}$, both of which are integrated over. The integration over the Euler angles and over the azimuthal angles of $\mathbf{a}$ and $\mathbf{r}$ can be done analytically, whereas the integrals over their polar angles and magnitudes have to be performed numerically. The quark and pion contributions to $G_A(q^2)$ can be given in terms of integrals of radial functions $u(r_\pm)$ and $v(r_\pm)$, and double Fourier transforms of $\phi(r)$ and $\sigma(r)$ (obtained in the self-consistent variational calculation), with arguments

$$r_\pm \equiv \Big| \mathbf{r} \pm \tfrac{1}{2}\mathbf{a} \Big| = \Big[r^2 + \frac{a^2}{4} \pm |\mathbf{a}|\,|\mathbf{r}|\, x \Big]^{1/2}, \tag{6.16}$$

where x is the relative angle between $\mathbf{r}$ and $\mathbf{a}$ (see appendix H for the details of the calculation).

Results and discussion

In our analysis of experimental data, we extracted the value of the axial mass parameter M_A from the measured cross-sections, where the dipole parameterisation (1.1) of the axial form factor has been used. Here we discuss the q^2-dependence of the *calculated* axial form factor. In order to make a meaningful comparison between them, the calculated form factor $g_A(q^2)$ should be 'normalised' to 1 at $q^2 = 0$, i. e. divided by the axial coupling constant $g_A(0)$ (see also the definition in section 6.2). In the framework of the LSM, we have calculated the form factor $g_A(q^2)$ in two distinct cases.

In the first approach, we used the conventional variation-after-projection method (VAP) applying only *angular* momentum projection to generate the radial quark and meson fields in a self-consistent calculation with the quark-meson coupling constant set to $g = 5.0$. When the appropriate set of integro-differential equations [116] for the fields is solved, the resulting fields minimise the energy of the projected $J = T = 1/2$ state (but not the energy of the unprojected hedgehog state). These fields are then used to evaluate the matrix element of the axial current

(see figure 6.1**a**). In the calculation without centre-of-mass and recoil corrections (ANG), we reproduce the characteristically large value of

$$g_A(0) = g_A^{(q)}(0) + g_A^{(m)}(0) = 0.961 + 0.823 = 1.783$$

at $q^2 = 0$ (similar values were obtained in a less general approach by [123]). This value is a very typical result for the LSM: the quark contribution by itself makes up for about 75 % of the experimental value of $g_A(0)$; the meson contribution, however, is large and spoils this relatively good agreement making the total $g_A(0)$ much too large. If linear momentum projection is applied in the calculation of the matrix element, i. e. when the centre-of-mass and recoil corrections are included (ANG+LIN), the quark contribution at $q^2 = 0$ increases for about $\Delta g_A^{(q)}(0) = +0.11$, but the meson contribution decreases for about $\Delta g_A^{(m)}(0) = -0.13$, so that

$$g_A(0) = 1.075 + 0.688 = 1.764\,.$$

Thus, the net effect on the total $g_A(0)$ is again negligible. Regardless of the technique applied, the absolute value of $g_A(0)$ is about 40 % above the experimental value.

Partially, the reason for this discrepancy might originate in the intrinsic inconsistencies of the LSM and similar effective models in which quarks are coupled to point-like pions with no underlying quark-antiquark structure. In such approximative approaches, the pions are treated as independent degrees of freedom (apart from being coupled to quarks), and some extent of double-counting is difficult to avoid. An attempted explanation that the quark-antiquark polarisation of the Dirac sea is effectively absorbed by the kinetic energy of the mesons, has also been proven erroneous (see [123], p. 91). Furthermore, the cancellation of $\Delta g_A^{(q)}$ and $\Delta g_A^{(m)}$ originating in the removal of the centre-of-mass effects, is present even at $q^2 \neq 0$. Within $0 \leq q^2 \leq 1\,\mathrm{GeV}^2$, the $g_A(q^2)$ calculated in the VAP approach using ANG does not differ from the ANG + LIN values by more than 12 %.

Quantitatively, a somewhat different behaviour of the axial form factor is observed in the second approach in which the radial quark and meson fields are obtained from a classical mean-field calculation. This amounts to solving a set of differential field equations without performing any angular or linear momentum projection *during* the generation of fields. At his point, we considered two sub-cases. First we took $g = 5.0$, and a single *angular* momentum projection on $J = T = 1/2$ was carried out before the calculation of the total baryon energy and other observables (VBP). In the second case (VBP+), an additional *linear* momentum projection on $q = 0$ was applied, and the coupling constant g was adjusted to reproduce the value of the total baryon energy to the experimentally observed nucleon mass ($g = 4.1$). The resulting radial fields were again used to evaluate the matrix element (see figure 6.1**b**) using either ANG or ANG + LIN. An obvious feature of this approach with the mean-field calculation is (in both sub-cases) a significantly weaker pion tail yielding a relatively small pion contribution to g_A. Without centre-of-mass and recoil corrections, we obtain

$$g_A(0) = 1.290 + 0.318 = 1.608\,,$$

whereas with the corrections included, we get

$$g_A(0) = 1.407 + 0.241 = 1.648\,.$$

We observe that the cancellation of the quark and the meson shifts in $g_A(q^2)$ is not as prominent, and the $g_A(q^2)$ calculated using ANG differs by $0.04 - 0.09$ (on the absolute scale) from the ANG + LIN values for $0 \leq q^2 \leq 1\,\mathrm{GeV}^2$.

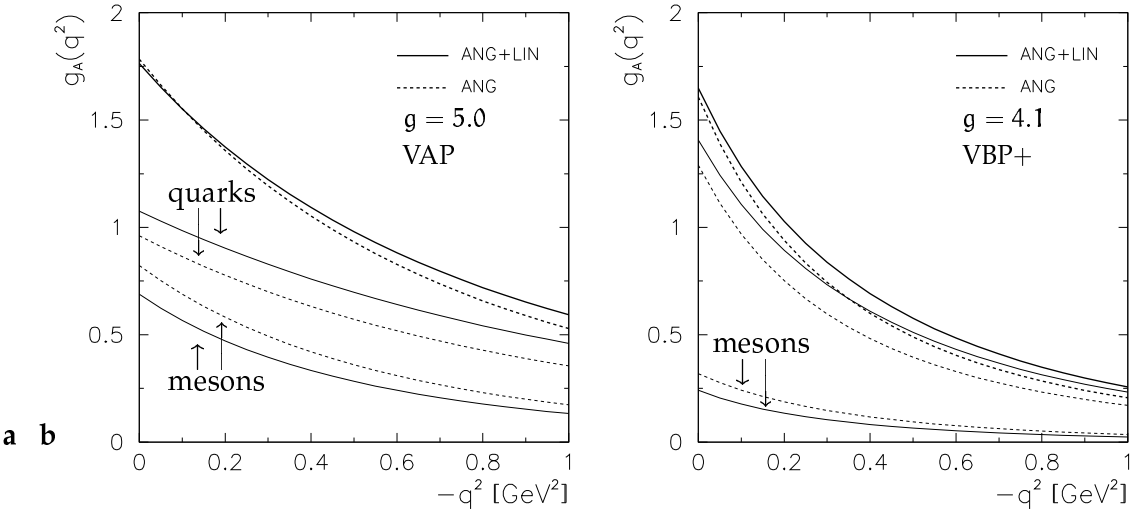

Figure 6.1: The q^2-dependence of the quark and the meson part (thin curves), and of the total axial form factor $g_A(q^2)$ (thick curves) in the LSM, without centre-of-mass and recoil corrections to the matrix element (dashed curves), and with corrections (full curves). The results were obtained **a** (VAP) – with $g = 5.0$, by using angular momentum projection for the self-consistent calculation of radial fields, **b** (VBP+) – with $g = 4.1$, by using the classical mean-field approximation to calculate the fields, and with the angular and linear momentum-projected total baryon energy fitted to reproduce the observed nucleon mass. The VBP sub-case is very similar to (VBP+), so it has been omitted for clarity.

Both approaches call for a rather obvious improvement: to include the linear momentum projection in the very determination of the radial fields. But in doing so, the variational procedure becomes very complicated and technically infeasible. At the moment, the only way to proceed was therefore to solve the equations of motion for the radial fields within some reasonable approximation *excluding linear momentum projection*, and to use these fields in the calculation of selected observables using ANG or ANG + LIN.

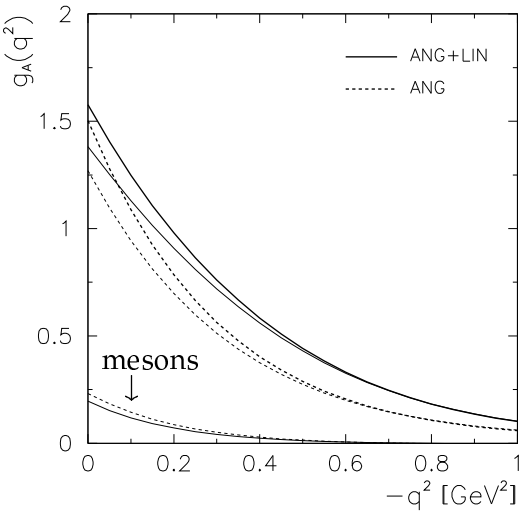

Figure 6.2: The q^2-dependence of the quark and the meson part (thin curves), and of the total axial form factor $g_A(q^2)$ (thick curves) in the CDM, without centre-of-mass and recoil corrections to the matrix element (dashed curves), and including corrections (full curves). The results were obtained with $\sqrt{g m_\chi} = 0.2\,\mathrm{GeV}$, by using VAP and angular momentum projection for the calculation of the fields.

In the CDM, the pion field is relatively weak since the quarks are basically confined by the χ field alone. Only the 'single minimum' quadratic potential for the confining field was considered since the 'double minimum' quartic form appearing in other studies with this model yields an unrealistic equation of state for quark matter [125]. We used the standard VAP in the CDM, and with a typical coupling constant of $\sqrt{gm_\chi} = 0.2\,\mathrm{GeV}$, we get

$$g_A = 1.270 + 0.232 = 1.502$$

if the matrix element is calculated without centre-of-mass and recoil corrections, and

$$g_A = 1.381 + 0.196 = 1.578$$

with these corrections included (similar values were obtained in a less general approach by [123]). At $q^2 \neq 0$, the rapid fall-off of the pion contribution resembles that of the LSM with the radial fields optimised for ANG + LIN, whereas the bulk of the q^2-dependence (as well as magnitude) of the form factor is again carried by the quark core. Within $0 \leq q^2 \leq 1\,\mathrm{GeV}^2$ (see figure 6.2), the corrections are as large as 0.20 on the absolute scale.

Figure 6.3 shows the results for the axial form factor for both models.

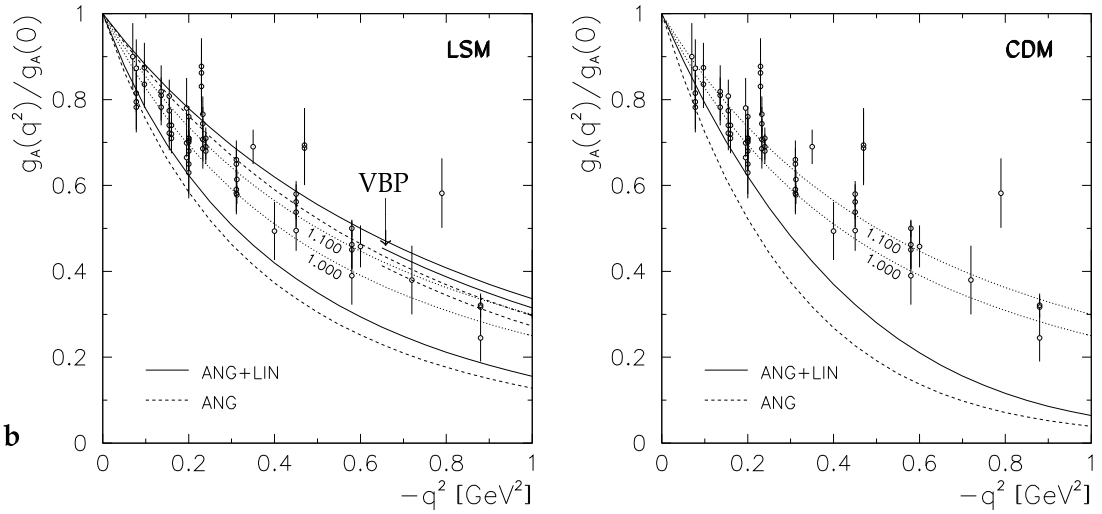

Figure 6.3: The axial form factor $G_A(q^2) = g_A(q^2)/g_A(0)$ **a** – in the LSM, using VAP and angular momentum projection to calculate the radial fields (upper pair of curves), or using the classical mean-field approximation (VBP+: lower pair and VBP: incomplete curves qualitatively similar to VBP+), and **b** – the CDM, in comparison to experimental data (for references to the data, see caption to figure 5.1). The dotted curves corresponding to the dipole parameterisations (1.1) with $M_A = 1.000\,\mathrm{GeV}$ and $M_A = 1.100\,\mathrm{GeV}$ are plotted for orientation.

7

Summary and outlook

We have measured the electro-production of positively charged pions on the proton at the invariant mass of $W = 1125\,\mathrm{MeV}$ and at four-momentum transfers of $q^2 = -0.195\,(\mathrm{GeV/c})^2$ and $-0.273\,(\mathrm{GeV/c})^2$. With these measurements, combined with our previous experiment at $q^2 = -0.117\,(\mathrm{GeV/c})^2$ [85], we completed our project to study the q^2-dependence of the transverse and the longitudinal cross-sections, separated by the Rosenbluth technique for each q^2. The statistical uncertainties were between 0.7 and 2.3 %, an improvement of an order of magnitude over [5], and the systematical uncertainties were estimated to be between 1.7 and 4.1 %. The latter are expected even to improve in the future experiments.

An effective Lagrangian model with pseudo-vector πNN coupling allowed us to extract the 'axial mass' parameter of the nucleon axial form factor from the transverse cross-section in a nearly model-independent way. Our extracted value of $M_A = (1.073 \pm 0.016)\,\mathrm{GeV}$ is $(0.056 \pm 0.028)\,\mathrm{GeV}$ larger than the axial mass $M_A = (1.017 \pm 0.023)\,\mathrm{GeV}$ known from neutrino scattering experiments. It essentially overlaps with the scaled-error weighted average $M_A = (1.068 \pm 0.017)\,\mathrm{GeV}$ of older pion electro-production experiments (figure 1.2), and if it is appended to the database, the weighted average increases to $M_A = (1.070 \pm 0.012)\,\mathrm{GeV}$ (figure 7.1).

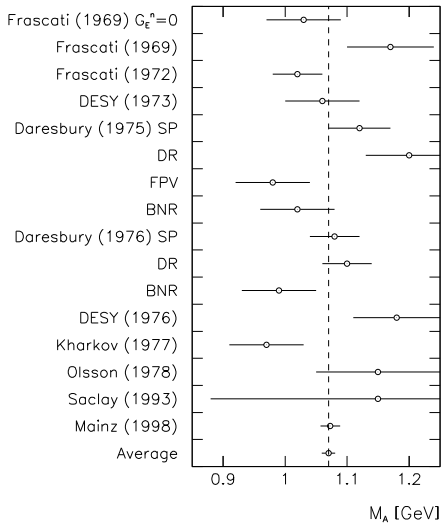

Figure 7.1: Axial mass M_A as extracted from charged pion electro-production experiments, including our measurement. The new weighted average, including the error-scaling procedure suggested by the Particle Data Group ([25], p. 9), is $M_A = (1.070 \pm 0.012)\,\mathrm{GeV}$.

The 'axial mass discrepancy' then becomes $\Delta M_A = (0.053 \pm 0.026)\,\mathrm{GeV}$. This value of ΔM_A is in perfect agreement with the prediction derived from χPT, $\Delta M_A = 0.056\,\mathrm{GeV}$. This strongly supports the hypothesis that processes involving pion loops modify the threshold $E_{0+}^{(-)}$ amplitude by about $\simeq 10\,\%$ at the order $\mathcal{O}(q^2)$. We conclude that the $\simeq 5\,\%$ discrepancy between the axial radii extracted from pion electro-production and (anti)neutrino scattering experiments is superficial and can be resolved by these corrections. Nevertheless, further work is needed on the theoretical as well as the experimental side: in particular, higher-loop corrections of the order m_π/M and $m_\pi^2/16\pi^2 f_\pi^2$ to the χPT result will soon have to be confronted by even more accurate measurements of the A1 Collaboration, particularly by measurements of $p(e, e'\pi^+)n$ closer to threshold and utilising the new short-orbit spectrometer [126, 127] optimised for the detection of slow pions.

Our value for the charge radius of the pion $\langle r_\pi^2\rangle^{1/2} = (0.718 \pm 0.019)\,\mathrm{fm}$, extracted from the longitudinal part of the cross-section using the DT model, deviates slightly from the values of $\langle r_\pi^2\rangle^{1/2} = (0.657 \pm 0.012)\,\mathrm{fm}$ and $(0.666 \pm 0.035)\,\mathrm{fm}$ obtained from measurements of $\pi^\pm e \to \pi^\pm e$ elastic scattering [128, 129]. The discrepancy can be ascribed to the vicinity of the pion pole and to the relatively poor convergence of the partial wave series in the DT model. Moreover, the sensitivity of $d\sigma_L$ on $F_\pi(q^2)$ diminishes for low Q^2, so that further measurements at higher Q^2 would be necessary to analyse its q^2-dependence.

We have calculated the axial form factor in the framework of two chiral quark models of the nucleon: the linear σ-model (LSM) and the chiral chromodielectric model (CDM). The main aim of the calculation was to study the effect of removing the spurious centre-of-mass and recoil nucleon motion from the matrix element of the axial current, and to study to what extent the axial form factor depends on the pion cloud surrounding the valence quark core.

Due to the relatively weak pion cloud in the CDM, the value of the axial coupling constant is closer to the experimental value than in the LSM, but the normalised axial form factor falls off too rapidly, even though the centre-of-mass and recoil corrections bring the model calculation into a much better agreement with the data. Both observables are dominated only by the quark core.

In the LSM, which possesses a relatively strong pion cloud, two approaches have been attempted. If the radial fields were obtained by excluding the spurious effects from the total baryon energy, the calculated form factor slightly underestimates the data, and also mostly depends on the quark core. If the fields were obtained by the conventional variation-after-projection method, the sensitivity of the form factor to the pion cloud increases, so that the quark core and the pion cloud play quantitatively comparable roles in the magnitude of the axial coupling constant as well as in the q^2-dependence of the axial form factor. In this case, the calculation overestimates the data by about $10\,\%$. In both approaches, the radial fields used in the calculation of observables were obtained by solving the equations of motion, ignoring linear momentum projection. An obvious improvement of our evaluation would require including the linear momentum projection in the variational calculation itself, but the technical complications of the procedure were beyond the scope of this work.

A

Extracting M_A from (anti)neutrino scattering experiments

The extraction of M_A from (anti)neutrino scattering experiments relies on the quasi-elastic picture of the scattering process, meaning that (anti)neutrinos interact only with individual nucleons (or quarks) within the target molecule whereas its remaining nucleons (or quarks) simply witness the event. The underlying elementary flavour-changing processes are $\nu_l + d \to l^- + u$ and $\overline{\nu}_l + u \to l^+ + d$, where $l = e, \mu$. So for the liquid hydrogen target, for example, one directly measures the $\overline{\nu}_\mu + p \to \mu^+ + n$ amplitude, whereas a reaction on a deuteron, say $\nu_\mu + d \to \mu^- + p + p_{\text{witness}}$, is in fact a measure for the $\nu_\mu + n \to \mu^- + p$ process.

These lepton-quark charged current interactions are mediated by the $W^\pm$ bosons, but at neutrino energies well below the $W^\pm$ resonance, they can be sufficiently accurately described by the effective Fermi interaction of the pure leptonic $V - A$ current and the weak hadronic current. The weak hadronic current also has a vector and an axial component, but strong interactions distort the pure $V - A$ form and one has to introduce weak form factors for individual contributions to the current. The most general form of the weak hadronic current is

$$\begin{aligned}\langle N'(p') \,|\, \hat{J}^w_\mu \,|\, N(p) \rangle \;=\; & \\ \cos\theta_C \, \overline{u}_{N'}(p') \Big[& \; f_1(q^2)\gamma_\mu \;\; + \frac{i f_2(q^2)}{2M}\, \sigma_{\mu\nu} q^\nu \;\; + \frac{f_3(q^2)}{2M} q_\mu \\ & + \; g_1(q^2)\gamma_\mu\gamma_5 + \frac{i g_2(q^2)}{2M}\, \sigma_{\mu\nu}\gamma_5 q^\nu + \frac{g_3(q^2)}{2M}\gamma_5 q_\mu \Big] \, u_N(p) \,, \end{aligned} \qquad \text{(A.1)}$$

where the vector part of the current has been decomposed into the *vector*, *weak magnetism* and *induced scalar* terms, and the axial part of the current into the *axial-vector*, *pseudo-tensor* and *induced pseudo-scalar* terms. For simplicity, we set $M_p = M_n \equiv M$. The weak form factors f_i and g_i are functions of q^2, where $q = p - p'$.

The electro-magnetic current is a pure vector current and can also be decomposed into the *electric*, *magnetic* and *induced scalar* terms

$$\langle N(p') \,|\, \hat{J}^{EM}_\mu \,|\, N(p) \rangle = \overline{u}_N(p') \Big[F_1^N(q^2)\gamma_\mu + \frac{i F_2^N(q^2)}{2M}\, \sigma_{\mu\nu} q^\nu + \frac{F_3^N(q^2)}{2M} q_\mu \Big] \, u_N(p) \,. \qquad \text{(A.2)}$$

Conservation of the electro-magnetic current $\partial^\mu J^{EM}_\mu = 0$ immediately gives $F_3^N = 0$ by virtue of the Dirac equation $\overline{u}_N \not{q} u_N = \overline{u}_N (\not{p} - \not{p}') u_N = (M - M)\overline{u}_N u_N = 0$. In addition, T-invariance of the electro-magnetic amplitude requires the F_1^N and F_2^N to be real. The Dirac-Pauli electric and magnetic form factors F_1 and F_2 are normalised to the nucleons' charges and anomalous magnetic moments, i. e. $F_1^p(0) = 1$, $F_1^n(0) = 0$, $F_2^p(0) = \kappa_p = 1.79$, and $F_2^n(0) = \kappa_n = -1.91$.

In theoretical interpretation of the neutrino scattering data one extensively uses the conserved vector current (CVC) hypothesis [130]. The CVC hypothesis states that since the electromagnetic current (which is a vector current) is conserved, the *vector part* of the weak hadron current should also be conserved. This statement is based on the observation that in the $q^2 \to 0$ limit, the isovector component of the electro-magnetic current

$$\langle N' | \hat{J}_\mu^{EM,V} | N \rangle = \overline{u} [F_1^p(0) - F_1^n(0)] \gamma_\mu \tfrac{1}{2}\tau_3 u = \overline{u}' \gamma_\mu \tfrac{1}{2}\tau_3 u$$

and the combinations

$$\begin{aligned} \langle p | \hat{J}_\mu^{w,1} + i\hat{J}_\mu^{w,2} | n \rangle &= \overline{u}' \gamma_\mu \tfrac{1}{2}\tau_+ u \,, \\ \langle n | \hat{J}_\mu^{w,1} - i\hat{J}_\mu^{w,2} | p \rangle &= \overline{u}' \gamma_\mu \tfrac{1}{2}\tau_- u \,, \end{aligned}$$

of the $SU(3)$ current octet members $J_\mu^{w,i}$ belong to the same isotriplet of currents. This means that we can identify

$$\begin{aligned} f_1(q^2) &= F_1^p(q^2) - F_1^n(q^2) \longrightarrow 1 \,, \\ f_2(q^2) &= F_2^p(q^2) - F_2^n(q^2) \longrightarrow \kappa_p - \kappa_n \,, \\ f_3(q^2) &= F_3^{p,n}(q^2) \equiv 0 \,. \end{aligned} \tag{A.3}$$

Note that the question of how fundamental CVC is can be rephrased by asking how badly the chiral $SU(3)$ invariance of QCD (as discussed at the beginning of subsection 6.1.4) is broken. In other words, if $SU(3)_A$ remains hidden, CVC is valid to the level of validity of $SU(3)_V$.

One further expects that the g_2 and g_3 form factors either vanish or are relatively small [131], so that the weak amplitude finally contains only f_1, f_2 and $g_1 \equiv G_A$. It has the form (the $+$ sign corresponds to neutrino and the $-$ sign to anti-neutrino scattering)

$$\frac{d\sigma^{\nu,\overline{\nu}}}{dQ^2} = \frac{M^2 G_w^2 \cos^2\theta_C}{8\pi E_{\nu,\overline{\nu}}^2} \left[A(q^2) \pm B(q^2) \frac{(s-u)}{M} + C(q^2) \frac{(s-u)^2}{M^2} \right] , \tag{A.4}$$

where G_w is the weak coupling constant determined from muon decay, θ_C is the Cabibbo angle and $q^2 = -Q^2 = (E_{\nu,\overline{\nu}} - E_\mu)^2 - (|\mathbf{p}_{\nu,\overline{\nu}}| - |\mathbf{p}_l|)^2$ is the four-momentum transfer. The coefficients $A(q^2)$, $B(q^2)$ and $C(q^2)$ (see [9] for explicit expressions) multiplying the invariants $s - u = 4ME_{\nu,\overline{\nu}} + q^2 - m_l^2$ and $(s-u)^2$ are scalar functions of q^2, and they contain the Dirac-Pauli form factors $F_1(q^2)$, $F_2(q^2)$ and the weak axial-vector form factor $G_A(q^2)$. The Dirac-Pauli form factors can be substituted by the physically more meaningful Sachs form factors according to

$$G_E^{p,n}(q^2) = F_1^{p,n}(q^2) + \frac{q^2}{4M^2} F_2^{p,n}(q^2) \,, \tag{A.5}$$

$$G_M^{p,n}(q^2) = F_1^{p,n}(q^2) + F_2^{p,n}(q^2) \,. \tag{A.6}$$

The Sachs form factors are usually written in their 'scaled' (and recently [132] argued against) dipole fall-off forms

$$G_E^p(q^2) = \frac{G_M^p(q^2)}{1+\kappa_p} = \frac{G_M^n(q^2)}{\kappa_n} = \frac{1}{(1 - q^2/M_v^2)^2} \,, \tag{A.7}$$

$$G_E^n(q^2) = 0 \,, \tag{A.8}$$

in which κ_p and κ_n are proton and neutron anomalous magnetic moments. These form factors are well known and were measured to a high precision in many inclusive (e, e') scattering experiments [133] and the best fit to the data gives the 'dipole mass' of $M_v^2 \simeq 0.71\,(\mathrm{GeV})^2$. The axial form factor $G_A(q^2)$ then remains the only unknown quantity and can be fitted to the measured cross-section (A.4).

B

Multipole expansion

In the conventions of Bjorken and Drell [45], the matrix element of the scattering matrix for $N(e,e'\pi)N'$ is

$$S_{fi} = \delta_{fi} - i\,(2\pi)^4 \delta^{(4)}(p_e + p_i - p'_e - p_f - p_\pi)\,\mathcal{M}_{fi}\,.$$

The invariant matrix element $\mathcal{M}_{fi}$ is equal to the scalar product of the photon polarisation four-vector and the expectation value of the hadronic electro-magnetic transition current operator $\widehat{J}^\mu$, times $-i$. The most general form of the transition current is

$$\widehat{J}^\mu = \Big(a_1\widetilde{\gamma}^\mu + a_2\widetilde{P}^\mu + a_3 p_\pi^\mu\Big)\gamma_5 + \Big(a_4\widetilde{\gamma}^\mu + a_5\widetilde{P}^\mu + a_6 p_\pi^\mu\Big)\gamma_5 \not{q}\,, \tag{B.1}$$

where $P \equiv \frac{1}{2}(p_i + p_f)$ and $\widetilde{x}^\mu \equiv x^\mu - (\gamma\cdot q/q^2)\,q^\mu$. The decomposition of the invariant matrix element along (B.1) is not unique. The matrix element of the current can generally be written as a sum of products of *Dirac operators* M_j and *invariant amplitudes* A_j, evaluated between the initial and the final nucleon bispinor [134, 135]

$$\mathcal{M}_{fi} = -i\,\epsilon_\mu\,\langle N'(p',s')\,|\,\widehat{J}^\mu\,|\,N(p,s)\rangle = \overline{u}_f(p',s')\sum_{j=1}^{6} A_j(s,t,u,q^2)\,M_j\,u_i(p,s)\,, \tag{B.2}$$

which is in accordance with (2.1). As soon as a certain choice for the invariant operators M_j is made, the amplitudes A_j are unambiguously fixed, and (B.1) is just a particular (gauge-invariant) way of doing this: the invariant operators M_j in this case can be obtained by contracting the operators in (B.1) with $-i\,\epsilon_\mu$. But there are other possibilities as well. In general, the operators M_j should contain combinations of four-vectors pertinent to the physical process: the four-momenta of the particles, the polarisation four-vector of the virtual photon, and the Dirac matrices. It goes without saying that the choice of M_j has to be consistent with requirements of Lorentz and gauge invariance, conservation of parity and constraints of the Dirac equation. The amplitudes A_j are functions of the Mandelstam variables

$$\begin{aligned} s &= (p_i + q)^2 = (p_f + p_\pi)^2 = W^2\,,\\ t &= (q - p_\pi)^2 = (p_i - p_f)^2\,,\\ u &= (q - p_f)^2 = (p_i - p_\pi)^2 \end{aligned}$$

and of the four-momentum transfer q^2 (for $p(e,e'\pi^+)n$, the relation $s + t + u = 2M^2 + m_\pi^2 + q^2$ constrains the number of independent variables to three). The invariants can then be constructed from the momentum four-vectors p_i, p_f, q, p_π, the photon polarisation four-vector ϵ and the set of four Dirac matrices γ. The only independent invariants containing γ matrices

are $\not{\epsilon}$ and $\not{k}$, since both $\not{p}_i$ and $\not{p}_f$ can be eliminated using the Dirac equation $(\not{p}_i - M)u(p_i) = 0$ or $\overline{u}(p_f)(\not{p}_f - M) = 0$ on both sides of the matrix element (B.2). Due to the conservation of energy and momentum, $\not{p}_\pi$ can be replaced by $\not{p}_i + \not{q} - \not{p}_f$. This leaves us with the invariants $\frac{1}{2}(p_i+p_f)\cdot q \equiv P\cdot q$, $p_\pi\cdot\epsilon$ and $q\cdot\epsilon$ (apart from $\not{\epsilon}$, the latter two are the only invariants containing ϵ).

There are some additional constraints on the form of the overall electro-production amplitude. The pion electro-production formalism is based on the assumption that only a single photon is exchanged between the electron and the nucleon, so that the amplitude must be proportional to ϵ_μ. Gauge invariance further requires that $M_{fi} \to 0$ if ϵ_μ is replaced by q_μ. This requirement is met by assigning $M_{fi} \propto F^{\mu\nu} \equiv \epsilon^\mu q^\nu - \epsilon^\nu q^\mu$. The produced pion has a negative intrinsic parity, so the amplitude has to be proportional to γ_5. One of further possible choices for the invariant electro-production operators is then [135]

$$\begin{aligned}
M_1 &= \tfrac{1}{2} i\gamma_5(\not{\epsilon}\not{q} - \not{q}\not{\epsilon}) ,\\
M_2 &= i\gamma_5(P\cdot\epsilon\,(2p_\pi\cdot q - q^2) - P\cdot q\,(2p_\pi\cdot\epsilon - q\cdot\epsilon)) ,\\
M_3 &= i\gamma_5(\not{\epsilon}\,p_\pi\cdot q - \not{q}\,p_\pi\cdot\epsilon) ,\\
M_4 &= 2i\gamma_5(\not{\epsilon}\,P\cdot q - \not{q}\,P\cdot\epsilon) - iM\gamma_5(\not{\epsilon}\not{q} - \not{q}\not{\epsilon}) ,\\
M_5 &= i\gamma_5(q\cdot\epsilon\,p_\pi\cdot q - p_\pi\cdot\epsilon\,q^2) ,\\
M_6 &= i\gamma_5(q\cdot\epsilon\,\not{q} - \not{\epsilon}\,q^2) .
\end{aligned}$$

In photo-production, the number of independent invariants is reduced from 6 to 4, since $q^2 = 0$ and $\epsilon\cdot q = 0$. The conventional choice then is [134]

$$\begin{aligned}
M_1 &= i\gamma_5\not{\epsilon}\not{q} ,\\
M_2 &= 2i\gamma_5(P\cdot\epsilon\,p_\pi\cdot q - P\cdot q\,p_\pi\cdot\epsilon) ,\\
M_3 &= i\gamma_5(\not{\epsilon}\,p_\pi\cdot q - \not{q}\,p_\pi\cdot\epsilon) ,\\
M_4 &= 2i\gamma_5(\not{\epsilon}\,P\cdot q - \not{q}\,P\cdot\epsilon - M\not{\epsilon}\not{q}) .
\end{aligned}$$

The amplitude $\mathcal{M}_{fi}$ can now be reduced to its two-component form. In this step, the expectation value of the sum of the invariant operators between the initial and final nucleon bispinors $u(\mathbf{p}_i, s)$ and $\overline{u}(\mathbf{p}_f, s')$ is replaced by the expectation value of the spin operators, sandwiched between the Pauli spinors $|\,s\rangle$ and $|\,s'\rangle$. We define

$$\mathcal{M}_{fi} = \frac{4\pi W}{M}\,\langle s'\,|\,\mathcal{F}\,|\,s\rangle ,$$

so that

$$\begin{aligned}
\mathcal{F} = {} & i\,\boldsymbol{\sigma}\cdot\boldsymbol{\epsilon}\,\mathcal{F}_1 + \frac{\boldsymbol{\sigma}\cdot\mathbf{p}^\star_\pi\,\boldsymbol{\sigma}\cdot\mathbf{q}^\star\times\boldsymbol{\epsilon}}{|\mathbf{p}^\star_\pi|\,|\mathbf{q}^\star|}\,\mathcal{F}_2 + i\,\frac{\boldsymbol{\sigma}\cdot\mathbf{q}^\star\,\mathbf{p}^\star_\pi\cdot\boldsymbol{\epsilon}}{|\mathbf{p}^\star_\pi|\,|\mathbf{q}^\star|}\,\mathcal{F}_3 + i\,\frac{\boldsymbol{\sigma}\cdot\mathbf{p}^\star_\pi\,\mathbf{p}^\star_\pi\cdot\boldsymbol{\epsilon}}{|\mathbf{p}^\star_\pi|^2}\,\mathcal{F}_4 \\
& + i\,\frac{\boldsymbol{\sigma}\cdot\mathbf{q}^\star\,\mathbf{q}^\star\cdot\boldsymbol{\epsilon}}{|\mathbf{q}^\star|^2}\,\mathcal{F}_5 + i\,\frac{\boldsymbol{\sigma}\cdot\mathbf{p}^\star_\pi\,\mathbf{q}^\star\cdot\boldsymbol{\epsilon}}{|\mathbf{p}^\star_\pi|\,|\mathbf{q}^\star|}\,\mathcal{F}_6 - i\,\epsilon_0\frac{\boldsymbol{\sigma}\cdot\mathbf{p}^\star_\pi}{|\mathbf{p}^\star_\pi|}\,\mathcal{F}_7 - i\,\epsilon_0\frac{\boldsymbol{\sigma}\cdot\mathbf{q}^\star}{|\mathbf{q}^\star|}\,\mathcal{F}_8 ,
\end{aligned} \tag{B.3}$$

where momenta $\mathbf{q}^\star$ and $\mathbf{p}^\star_\pi$ are given in the centre-of-mass system of the final hadronic state. From the gauge invariance for the reduced amplitude $\mathcal{F}$, i. e. $\epsilon_\mu \to q^\star_\mu \Rightarrow \mathcal{F} \to 0$, it follows that

$$i\boldsymbol{\sigma}\frac{\mathbf{q}^\star}{|\mathbf{q}^\star|}\left[\,|\mathbf{q}^\star|\,\mathcal{F}_1 + |\mathbf{q}^\star|\cos\theta^\star_\pi\mathcal{F}_3 + |\mathbf{q}^\star|\,\mathcal{F}_5 - \omega^\star\mathcal{F}_8\,\right] = 0 , \tag{B.4}$$

$$i\boldsymbol{\sigma}\frac{\mathbf{p}^\star_\pi}{|\mathbf{p}^\star_\pi|}\left[\,|\mathbf{q}^\star|\cos\theta^\star_\pi\mathcal{F}_4 + |\mathbf{q}^\star|\,\mathcal{F}_6 - \omega^\star\mathcal{F}_7\,\right] = 0 , \tag{B.5}$$

where $|\mathbf{p}_\pi^\star||\mathbf{q}^\star| = \cos\theta_\pi^\star$. Gauge invariance therefore allows us to eliminate either $\mathcal{F}_7$ and $\mathcal{F}_8$ or $\mathcal{F}_5$ and $\mathcal{F}_6$ from (B.3). Each of the remaining 6 amplitudes $\mathcal{F}_j$ is just a linear combination of the 6 invariant amplitudes A_j (in the case of photo-production, two amplitudes again vanish due to $\boldsymbol{\epsilon}\cdot\mathbf{q}^\star = 0$). If we eliminate $\mathcal{F}_7$ and $\mathcal{F}_8$, we speak of the virtual photons as having two transverse and a longitudinal component, whereas if we eliminate $\mathcal{F}_5$ and $\mathcal{F}_6$, we speak of the photons as having two transverse and a scalar component. The liberty of doing this is called *choosing a gauge*.

Let us choose a gauge in which the scalar component of the virtual photon is eliminated. The amplitude $\mathcal{F}$ then remains of the form (B.3) if ϵ_μ is replaced by

$$a_\mu = \epsilon_\mu - \frac{\epsilon^0}{\omega^\star}\, q_\mu^\star \,.$$

In the next step, the amplitude $\mathcal{F}$ is expanded in terms of the electro-production multipoles [136], where the summations run over all allowed relative angular momenta of the emitted pion

$$\begin{aligned}
\mathcal{F}_1 &= \sum_{l=0}^{\infty}(lM_{l+} + E_{l+})P'_{l+1}(x) + \sum_{l=2}^{\infty}((l+1)M_{l-} + E_{l-})P'_{l-1}(x)\,,\\
\mathcal{F}_2 &= \sum_{l=1}^{\infty}((l+1)M_{l+} + lM_{l-})P'_l(x)\,,\\
\mathcal{F}_3 &= \sum_{l=1}^{\infty}(E_{l+} - M_{l+})P''_{l+1}(x) + \sum_{l=3}^{\infty}(E_{l-} + M_{l-})P''_{l-1}(x)\,,\\
\mathcal{F}_4 &= \sum_{l=2}^{\infty}(M_{l+} - E_{l+} - M_{l-} - E_{l-})P''_l(x)\,,\\
\mathcal{F}_5 &= \sum_{l=0}^{\infty}(l+1)L_{l+}P'_{l+1}(x) - \sum_{l=2}^{\infty} lL_{l-}P'_{l-1}(x)\,,\\
\mathcal{F}_6 &= \sum_{l=1}^{\infty}(lL_{l-} - (l+1)L_{l+})P'_l(x)\,,
\end{aligned}$$

and $x = \cos\theta_\pi^\star = \hat{\mathbf{p}}_\pi^\star\cdot\hat{\mathbf{q}}^\star$. In practice, one rarely ventures beyond $l = 2$, and mostly only terms with $l = 0$ and $l = 1$ are kept. The expansion then simplifies to

$$\begin{aligned}
\mathcal{F}_1 &= E_{0+} + 3(M_{1+} + E_{1+})\cos\theta_\pi^\star\,,\\
\mathcal{F}_2 &= 2M_{1+} + M_{1-}\,,\\
\mathcal{F}_3 &= 3(E_{1+} - M_{1+})\,,\\
\mathcal{F}_4 &= 0\,,\\
\mathcal{F}_5 &= L_{0+} + 6L_{1+}\cos\theta_\pi^\star\,,\\
\mathcal{F}_6 &= L_{1-} - 2L_{1+}\,.
\end{aligned}$$

The amplitudes $\mathcal{F}_5$ and $\mathcal{F}_6$ occur only in electro-production.

For the sake of completeness, we also quote the inverse relations, expressing the multipole amplitudes in terms of the reduced amplitudes. These relations follow from the recurrence and orthogonality relations of the Legendre polynomials:

$$M_{l+} = \frac{1}{2(l+1)}\int_{-1}^{1} dx\left[\mathcal{F}_1 P_l - \mathcal{F}_2 P_{l+1} - \mathcal{F}_3\frac{P_{l-1} - P_{l+1}}{2l+1}\right],$$

$$
\begin{aligned}
E_{l+} &= \frac{1}{2(l+1)}\int_{-1}^{1} dx \left[\mathcal{F}_1 P_l - \mathcal{F}_2 P_{l+1} + \mathcal{F}_3 \frac{l(P_{l-1}-P_{l+1})}{2l+1} + \mathcal{F}_4 \frac{(l+1)(P_l - P_{l+2})}{2l+3}\right], \\
L_{l+} &= \frac{1}{2(l+1)}\int_{-1}^{1} dx \left[\mathcal{F}_5 P_l + \mathcal{F}_6 P_{l+1}\right], \\
M_{l-} &= \frac{1}{2l}\int_{-1}^{1} dx \left[-\mathcal{F}_1 P_l + \mathcal{F}_2 P_{l-1} + \mathcal{F}_3 \frac{P_{l-1}-P_{l+1}}{2l+1}\right], \\
E_{l-} &= \frac{1}{2l}\int_{-1}^{1} dx \left[\mathcal{F}_1 P_l - \mathcal{F}_2 P_{l-1} - \mathcal{F}_3 \frac{(l+1)(P_{l-1}-P_{l+1})}{2l+1} + \mathcal{F}_4 \frac{l(P_l - P_{l-2})}{2l-1}\right], \\
L_{l-} &= \frac{1}{2l}\int_{-1}^{1} dx \left[\mathcal{F}_5 P_l + \mathcal{F}_6 P_{l-1}\right],
\end{aligned}
$$

where all P_l depend on x and $'$ denotes a derivative with respect to x. The advantage of the inverse formulas is that one can easily read off the power behaviour of the electro-production multipoles for small values of $|\mathbf{q}^\star|$ and $|\mathbf{p}_\pi^\star|$. In this limit, the reduced amplitudes $\mathcal{F}_j$ can be expanded as

$$
\mathcal{F}_i = \sum_{n=0}^{\infty} F_{in} (|\mathbf{p}_\pi^\star|\,|\mathbf{q}^\star|\,x)^n ,
$$

so that in the vicinity of the threshold

$$
\begin{aligned}
E_{l+}, L_{l+} &\sim |\mathbf{q}^\star|^l\,|\mathbf{p}_\pi^\star|^l \qquad & l \geq 0 , \\
M_{l+}, M_{l-} &\sim |\mathbf{q}^\star|^l\,|\mathbf{p}_\pi^\star|^l \qquad & l \geq 1 , \\
E_{l-}, L_{l-} &\sim |\mathbf{q}^\star|^{l-2}\,|\mathbf{p}_\pi^\star|^l \qquad & l \geq 2 ,
\end{aligned}
$$

with the exception of $L_{1-} \sim |\mathbf{q}^\star|\,|\mathbf{p}_\pi^\star|$. We see from these expressions that close to the pion production threshold, only s-wave pions are emitted, since all multipoles behave as $|\mathbf{p}_\pi^\star|^l$.

In the final step, the structure functions R_T, R_L, R_{LT} and R_{TT} have to be expressed in terms of $\mathcal{F}_j$s and, through these, in terms of the multipoles. The procedure gives

$$
\begin{aligned}
R_T &= |\mathcal{F}_1|^2 + |\mathcal{F}_2|^2 + \tfrac{1}{2}\sin^2\theta_\pi^\star\,[\,|\mathcal{F}_3|^2 + |\mathcal{F}_4|^2\,] \\
&\quad - \mathrm{Re}\,[\,2\cos\theta_\pi^\star\,\mathcal{F}_1^*\mathcal{F}_2 - \sin^2\theta_\pi^\star\,(\,\mathcal{F}_1^*\mathcal{F}_4 + \mathcal{F}_2^*\mathcal{F}_3 + \cos\theta_\pi^\star\,\mathcal{F}_3^*\mathcal{F}_4\,)\,]\,, \\
R_L &= |\mathcal{F}_5|^2 + |\mathcal{F}_6|^2 + 2\cos\theta_\pi^\star\,\mathrm{Re}\,[\,\mathcal{F}_5^*\mathcal{F}_6]\,, \\
R_{LT} &= -\sin\theta_\pi^\star\,\mathrm{Re}\,[\,(\,\mathcal{F}_2^* + \mathcal{F}_3^* + \cos\theta_\pi^\star\,\mathcal{F}_4^*\,)\mathcal{F}_5 + (\,\mathcal{F}_1^* + \mathcal{F}_4^* + \cos\theta_\pi^\star\,\mathcal{F}_3^*\,)\mathcal{F}_6\,]\,, \\
R_{TT} &= \sin^2\theta_\pi^\star\,[\,\tfrac{1}{2}(\,|\mathcal{F}_3|^2 + |\mathcal{F}_4|^2\,) + \mathrm{Re}\,[\,\mathcal{F}_1^*\mathcal{F}_4 + \mathcal{F}_2^*\mathcal{F}_3 + \cos\theta_\pi^\star\,\mathcal{F}_3^*\mathcal{F}_4\,]\,]\,.
\end{aligned}
$$

Again limiting our considerations only to $l_\pi \leq 1$, we get

$$
\begin{aligned}
R_T &\equiv a_0 + a_1\cos\theta_\pi^\star + a_2\cos^2\theta_\pi^\star \\
&= |E_{0+}|^2 + \tfrac{1}{2}\,|2M_{1+} + M_{1-}|^2 + \tfrac{1}{2}\,|3E_{1+} - M_{1+} + M_{1-}|^2 \\
&\quad + 2\cos\theta_\pi^\star\,\mathrm{Re}\,[\,E_{0+}^*(3E_{1+} + M_{1+} - M_{1-})\,] \\
&\quad + \cos^2\theta_\pi^\star\,(\,|3E_{1+} + M_{1+} - M_{1-}|^2 - \tfrac{1}{2}\,|2M_{1+} + M_{1-}|^2 \\
&\qquad - \tfrac{1}{2}\,|3E_{1+} - M_{1+} + M_{1-}|^2)\,, \qquad \text{(B.6)}
\end{aligned}
$$

$$
\begin{aligned}
R_L &\equiv a_0' + a_1'\cos\theta_\pi^\star + a_2'\cos^2\theta_\pi^\star \\
&= |L_{0+}|^2 + 4|L_{1+}|^2 + |L_{1-}|^2 - 4\mathrm{Re}\,[\,L_{1+}^* L_{1-}] \\
&\quad + 2\cos\theta_\pi^\star\,\mathrm{Re}\,[\,L_{0+}^*(4L_{1+} + L_{1-})\,] + 12\cos^2\theta_\pi^\star\,(\,|L_{1+}|^2 + \mathrm{Re}\,[\,L_{1+}^* L_{1-}]\,)\,, \qquad \text{(B.7)}
\end{aligned}
$$

$$
\begin{aligned}
R_{LT} &\equiv \sin\theta_\pi^\star (d_0 + d_1 \cos\theta_\pi^\star) \\
&= -\sin\theta_\pi^\star \,\mathrm{Re}\,[\, L_{0+}^*(3E_{1+} - M_{1+} + M_{1-}) - E_{0+}(2L_{1+}^* - L_{1-}^*) \\
&\qquad + 6\cos\theta_\pi^\star\,(L_{1+}^*(E_{1+} - M_{1+} + M_{1-}) + L_{1-}^* E_{1+})\,]\,, \qquad \text{(B.8)} \\
R_{TT} &\equiv \sin^2\theta_\pi^\star c_0 \\
&= 3\sin^2\theta_\pi^\star\,[\,\tfrac{3}{2}\,|E_{1+}|^2 - \tfrac{1}{2}\,|M_{1+}|^2 - \mathrm{Re}\,[\,E_{1+}^*(M_{1+} - M_{1-}) + M_{1+}^* M_{1-}]\,]\,. \qquad \text{(B.9)}
\end{aligned}
$$

The meaning of coefficients a, b, c and d becomes apparent when the differential electroproduction cross-section is expanded in terms of the pion scattering angle

$$
\begin{aligned}
\frac{d\sigma_v}{d\Omega_\pi^\star} &= \overline{A}_0 + \overline{A}_1 \cos\theta_\pi^\star + \overline{A}_2 \cos^2\theta_\pi^\star + \overline{A}_3 \cos^3\theta_\pi^\star + \ldots \\
&\quad + \varepsilon\,(C_0 + C_1 \cos\theta_\pi^\star + C_2 \cos^2\theta_\pi^\star + \ldots)\sin^2\theta_\pi^\star \cos 2\phi_\pi \\
&\quad + \sqrt{2\,\varepsilon_L^\star(1+\varepsilon)}\,(D_0 + D_1 \cos\theta_\pi^\star + D_2 \cos^2\theta_\pi^\star + \ldots)\sin\theta_\pi^\star \cos\phi_\pi\,. \qquad \text{(B.10)}
\end{aligned}
$$

The expansion coefficients $\overline{A}_0, \ldots, C_0, \ldots, D_0, \ldots$ are independent of $\theta_\pi^\star$; at given energy and momentum transfers they depend only on the individual multipoles. Since only the s and p-waves contribute in the region below the Δ-resonance, we read off from (B.6–B.9) that

$$
\begin{aligned}
\overline{A}_0 &= \frac{|\mathbf{p}_\pi^\star|}{Q_\gamma^\star}\,[a_0 + \varepsilon_L^\star a_0']\,, \qquad C_0 = \frac{|\mathbf{p}_\pi^\star|}{Q_\gamma^\star}\,c_0\,, \\
\overline{A}_1 &= \frac{|\mathbf{p}_\pi^\star|}{Q_\gamma^\star}\,[a_1 + \varepsilon_L^\star a_1']\,, \qquad D_0 = \frac{|\mathbf{p}_\pi^\star|}{Q_\gamma^\star}\,d_0\,, \qquad \text{(B.11)} \\
\overline{A}_2 &= \frac{|\mathbf{p}_\pi^\star|}{Q_\gamma^\star}\,[a_2 + \varepsilon_L^\star a_2']\,, \qquad D_1 = \frac{|\mathbf{p}_\pi^\star|}{Q_\gamma^\star}\,d_1\,.
\end{aligned}
$$

C

Isospin decomposition

Even though electro-magnetic interactions do not conserve isospin, the interaction Hamiltonian operator possesses certain properties with respect to isospin transformations. The reason for this is the structure of the electro-magnetic current, which in isospin space acts as an isoscalar plus the third component of an isovector, $J^{\mu}_{EM} = J^{\mu}_{s} + J^{\mu}_{3}$. The selection rule is $\Delta T = 0$ for isoscalar transitions, and $\Delta T = 0, \pm 1$ for isovector transitions. Therefore *three* independent isospin amplitudes are required to express the pion electro-production amplitude, which can be expanded in isospin space in a symmetrical form

$$A_j(s,t,u,q^2) = A_j^{(+)}\,\delta_{\alpha 0} + A_j^{(-)}\,\tfrac{1}{2}[\tau_\alpha,\tau_0] + A_j^{(0)}\,\tau_\alpha\,,$$

where α is the isospin index of the emitted pion and $\boldsymbol{\tau}$ are the nucleon isospin matrices. We suppress the index j and quote only the isospin structure of the amplitudes [135, 136]. The physical amplitudes (pertaining to specific reaction channels) are

$$\begin{aligned}
A(\gamma_v p \to n\pi^+) &= \sqrt{2}\left[A^{(0)} + A^{(-)}\right]\,,\\
A(\gamma_v p \to p\pi^0) &= \quad\left[A^{(0)} + A^{(+)}\right]\,,\\
A(\gamma_v n \to p\pi^-) &= \sqrt{2}\left[A^{(0)} - A^{(-)}\right]\,,\\
A(\gamma_v n \to n\pi^0) &= -\left[A^{(0)} - A^{(+)}\right]\,.
\end{aligned}$$

D

Corrections of radiation losses in $p(e, e'\pi^+)n$

The electrons and the pions taking part in the $p(e,e'\pi^+)n$ reaction interact with the target protons and with the electron clouds of the target atoms, and thereby lose a fraction ΔE of their energy E_i by radiating additional real or virtual photons. Since these *radiation losses* can not be directly measured, the reconstructed energy transfer, momentum transfer, missing mass and related distributions become distorted: they develop *radiative tails*. For example, the spectrum of the scattered electron energies E_f should ideally appear as a sharp peak, broadened only by the intrinsic energy resolution of the experimental setup. With radiation losses, in which the electrons randomly radiate away a certain amount of energy, the spectrum acquires an energy-dependent tail

$$\frac{d\sigma_0}{dE_f} = \sigma_0 f(E_f)$$

with the probability density $f(E_f)$ normalised to unity, $\int_0^{E_f^0} f(E_f)dE_f = 1$. The experimental spectrum σ is obtained by counting the events contained within the interval between the maximum possible energy E_f^0 and some minimum energy $E_f^0 - \Delta E$, where ΔE is much larger than the experimental energy resolution. The 'true' spectrum σ_0 (i. e. without any losses) is then obtained from the measured spectrum σ according to

$$\sigma = \int_{E_f^0-\Delta E}^{E_f^0} \frac{d\sigma_0}{dE} dE = \sigma_0 \int_{E_i^0-\Delta E}^{E_i^0} f(E_f)dE_f = F(\Delta E)\sigma_0 \,,$$

where $F(\Delta E)$ is the fraction of electrons which suffered an energy loss of less than ΔE. In other words, the fraction of events that due to radiation losses migrated to energies, lower than $E_f^0 - \Delta E$, is equal to $1 - F(\Delta E)$. The 'true' number of events is then

$$\sigma_0 = \frac{1}{F(\Delta E)}\sigma \equiv K(\Delta E)\sigma \,, \tag{D.1}$$

where $K(\Delta E)$ is the *correction factor*. In $p(e,e'\pi^+)n$ experiments with particle momenta of a few hundred MeV, typical correction factors are between 1.05 and 1.20 for *cut-off* energies ΔE of 3 to 10 MeV.

The problem is that the energy losses ΔE of the particles do not map trivially to the corresponding shifts in the missing mass, since M_m (4.1) is a non-linear function of E_e, E_e' and E_π. For example, it is obvious that an incoming electron's energy loss of 10 MeV, which is also 'inherited' by the exchanged virtual photon, does not necessarily correspond to a shift of 10 MeV in the M_m distribution. Furthermore, if beam wobbling over extended targets is used in a real

experiment, the paths traversed by the particles vary for each event and so do their energy losses. In addition, the detector acceptances should be unfolded from the radiative losses. The 'average' correction factors $K(\Delta E)$ do not take any of these effects into account. In our analysis, the radiative corrections were evaluated in the simulation of the detector acceptances. For the sake of being complete, the following section presents both approaches.

Energy losses in individual radiative processes

The photons emitted in the radiative processes are not detected in the experiment, so that the theoretical probability densities f have to be averaged over all their possible momenta and emission angles. The treatment of radiative losses is usually simplified by assuming that only the magnitude of a particle's momentum changes in the radiative process, and not its direction (the *forward-peaking approximation*). Consequently, the averaged correction factors depend only on ΔE, the momenta of the particles involved, and the target composition.

However, when radiative processes are included in a computer simulation, full track can be kept of the particles' trajectories and their lengths in various materials, and the corresponding energy losses and corrections can be evaluated for each event separately. The energy losses in the simulation are treated in two steps. When events are *generated* (see also section 4.7), authentic experimental conditions are simulated by assigning to each particle involved an energy loss of dE/dx, integrated over the length of its path Δx in a given material. To be able to compare the resulting distributions to the measured ones, the energy losses then have to be corrected for in exactly the same manner as it is done in the analysis program. But since exact energy losses in each event of the real data are not known, we use *most probable* energy losses for the correction in the data analysis as well as in the simulation.

Internal Bremsstrahlung

The process in which the electrons radiate real or virtual photons (in addition to the exchanged virtual photon) in the vicinity of the target protons, is known as the *Schwinger radiation* or the *internal Bremsstrahlung*. In $p(e,e'\pi^+)n$ reactions, this is by far the largest contribution to the radiative tails: since the Bremsstrahlung probability is inversely proportional to the square of the particle's mass, the contribution of the pions to this process is entirely negligible. The lowest order Feynman graphs contributing to the Schwinger radiation in $p(e,e'\pi^+)n$ are shown in figure D.1. Internal Bremsstrahlung occurs during the reaction itself, so that the averaged Schwinger correction factor does not depend on the target thickness.

The averaged correction factors for Schwinger radiation have been parameterised in a number of ways [137, 138, 139], but all methods give almost identical results. A common starting point is the factor in the form

$$K_{\mathrm{Schw}} = \frac{e^{\delta_{\mathrm{real}}}}{1+\delta_{\mathrm{virt}}} \tag{D.2}$$

which was successfully used in radiative corrections of the $A(e,e'p)B$ data [139]. The graphs of type **a** in figure D.1 contribute to δ_{real}, whereas graphs of type **b**, **c** and **d** contribute to δ_{virt}:

$$\delta_{\mathrm{real}} = \frac{2\alpha}{\pi}\ln\frac{\sqrt{b}\sqrt{E_e E'_e}}{\eta\Delta E}\left[\ln\frac{-q^2}{m_e^2}-1\right],$$

$$\delta_{\mathrm{virt}} = \frac{2\alpha}{\pi}\left\{\frac{13}{12}\left[\ln\frac{-q^2}{m_e^2}-1\right]-\frac{17}{36}-\frac{1}{4}\ln^2\frac{E_e}{E'_e}-\frac{\pi^2}{12}+\frac{1}{2}L_2\left(\cos^2\frac{\theta_e}{2}\right)\right\}.$$

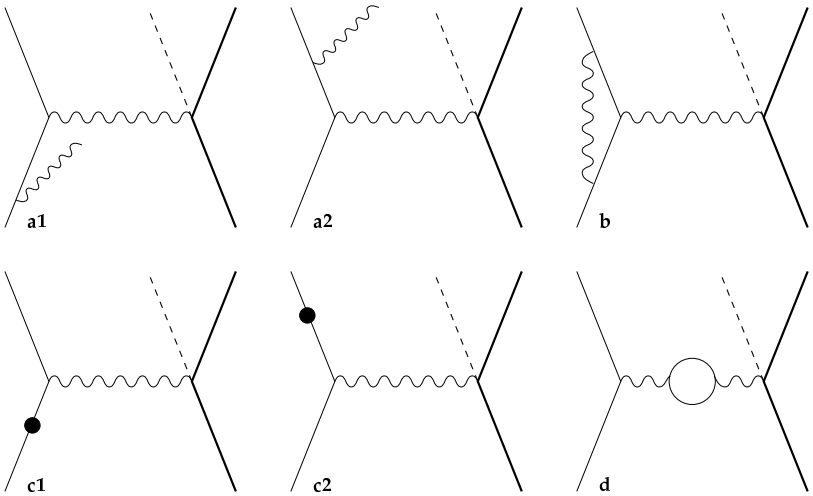

Figure D.1: The lowest order Feynman graphs for internal Bremsstrahlung processes (Schwinger radiation) in $p(e,e'\pi^+)n$ **a1**, **a2** – emission of real photons, **b** – electron vertex correction, **c1**, **c2** – renormalisation of the electron mass (emission and reabsorption of the photon in the electron line), **d** – vacuum polarisation.

These expressions generalise the results for potential scattering [140] and for inelastic electron-nucleon scattering. The factors b and η are inserted as effective corrections due to the recoil of the target nucleus (they become important when $-q^2$ becomes comparable to the target nucleus mass) and are equal to

$$b = 1 + \frac{2\omega}{M}\sin^2\frac{\theta_e}{2}\,,$$
$$\eta = 1 + \frac{2E_e}{M}\sin^2\frac{\theta_e}{2}\,,$$

and $L_2(x)$ is the Spence function, $L_2(x) = \sum_n x^n/n^2$. Very often, an *exponentiated* parameterisation of the correction factors is used instead of (D.2). As long as δ_{virt} is small, we may rewrite K_{Schw} as

$$K_{Schw} = \frac{e^{\delta_{real}}}{1+\delta_{virt}} \simeq e^{\delta_{real}}(1-\delta_{virt}) \simeq e^{\delta_{real}-\delta_{virt}} \equiv e^{\delta_{Schw}}\,,$$

where

$$\delta_{Schw} = \frac{2\alpha}{\pi}\left\{\left[\ln\frac{q^2}{m_e^2}-1\right]\left[\ln\frac{\sqrt{b}\sqrt{E_eE_e'}}{\eta\Delta E}-\frac{13}{12}\right]+\frac{17}{36}+\frac{1}{4}\ln^2\frac{E_e}{E_e'}+\frac{1}{2}\left[\frac{\pi^2}{6}-L_2\left(\cos^2\frac{\theta_e}{2}\right)\right]\right\}.$$

The exponentiated form has a deeper physical background [137, 138]. Schwinger has shown in his analysis of potential scattering [140] with $M\to\infty$ that the measured cross-section and the cross-section, evaluated in the plane-wave Born approximation, are related through

$$d\sigma = (1-\delta_{pot})\,d\sigma|_{Born}\,, \tag{D.3}$$

as in (D.1). Here δ_{pot} is equal to the expression for δ_{Schw} with all terms from 17/36 left out, $\sqrt{E_eE_e'}$ replaced by E_e (since $E_e = E_e'$ for potential scattering), and recoil factors b and η set to unity. The δ_{pot} is logarithmically divergent for $\Delta E\to 0$, and (D.3) leads to a negative cross-section. On the other hand, scattering processes are *always* accompanied by emissions of real or virtual photons, so that physically, one expects $d\sigma\to 0$ for $\Delta E\to 0$. The exponential form

$1 - \delta \rightarrow e^{-\delta}$ with the correct behaviour for $\Delta E \rightarrow 0$ was proposed already by Schwinger. Its physical content is the possibility of an emission of *soft* real or virtual photons with the number of quanta going to infinity and the energy of quanta going to zero, but with a *finite* total radiated energy. This is the basic statement of the Bloch-Nordsieck theorem [141]: the intensity of the radiation I_ω per unit of frequency goes to zero when $\omega \rightarrow 0$; but in the same limit, $I_\omega/\hbar\omega$ (which can be understood as the average number of quanta per unit of frequency) goes to infinity.

In the framework of the acceptance simulation, the Schwinger processes are treated in two steps. The vertex correction and the vacuum polarisation processes remain encapsulated in the correction factor δ_{virt} and the simulated spectra are weighted by $\exp(-\delta_{\text{virt}})$. On the other hand, the treatment of the real-photon part of Schwinger radiation follows the prescription of [137] that the effect of internal Bremsstrahlung can be approximated by a joint effect of two external radiators (the so-called *equivalent radiators*), one placed before and one after the scattering, each of thickness

$$\frac{t}{X_0} = \frac{\alpha}{\pi b}\left[\ln\frac{-q^2}{m_e^2} - 1\right], \tag{D.4}$$

with

$$b = \frac{4}{3}\left[1 + \frac{1}{9}\frac{Z+1}{Z+\xi}\ln^{-1}(183\,Z^{-1/3})\right]$$

and $\xi = \ln(1440\,Z^{-2/3})/\ln(183\,Z^{-1/3})$, where the target surface thickness t and the radiation length X_0 are both given in g/cm^2.

External Bremsstrahlung

In the process of the external Bremsstrahlung, either the electron before the reaction or the scattered electron emit photons in the field of *other* nuclei (sc. those not involved in the reaction under study). As opposed to the Schwinger radiation, the external Bremsstrahlung occurs while the incoming and the scattered electron penetrate through the target and interact with its nuclei: the averaged correction factor is proportional to the target thickness and is written in the exponentiated form [142] $K_{\text{brems}} = e^{\delta_{\text{brems}}}$, since

$$\delta_{\text{brems}} = \frac{t}{X_0}\left[-(\zeta - \tfrac{1}{2}) + \zeta\ln\frac{E}{\Delta E} + \zeta\frac{\Delta E}{E} - \frac{1}{2}\left(\frac{\Delta E}{E}\right)^2\right]$$

diverges for $\Delta E \rightarrow 0$. In the expression above, E is the electron energy before or after the reaction, and ζ is a known function of Z of the target nucleus

$$\zeta = \frac{1}{9}\left[12 + \frac{Z+1}{Z l_1(Z) + l_2(Z)}\right].$$

The parameters l_1 and l_2 are tabulated and have values between 5 and 7 for light nuclei. In our case with $Z = 1$, $\zeta \simeq 4/3$ and $X_0 = 63.29\,g/cm^2$ for a liquid hydrogen target (parameterisations of the radiation length in Z and A for other target materials also exist [139]).

In the simulation program, the distribution of energy losses in $\Delta E \equiv E - E'$ (where E is the unperturbed energy of the particle) due to external Bremsstrahlung of electrons is described in terms of the probability distribution

$$\frac{dP}{d\Delta E} = \frac{bt/X_0}{\Gamma(1 + bt/X_0)}\left[\frac{\Delta E}{E}\right]^{bt/X_0}\frac{1}{\Delta E}. \tag{D.5}$$

The parameter b is the same as in the case of internal Bremsstrahlung, whereas the surface thickness $t = \rho\Delta x$ is calculated for each generated electron track when its length Δx within the material of density ρ is reconstructed from the position of the reaction point. The internal and external Bremsstrahlung energy losses are imposed simultaneously by adding this calculated t to the t from (D.4) and picking a random value of ΔE according to the distribution (D.5). Note that in all circumstances, $t_{IB} \gg t_{EB}$. In our kinematical settings, a typical trajectory length within the target cell is $t_{EB}/\rho_{LH_2} \simeq 0.5\,\mathrm{cm}$, whereas typically $t_{IB} \simeq 20\,t_{EB}$, and so $t_{IB} + t_{EB} \simeq t_{IB}$: the energy losses of electrons originate mostly in the Schwinger processes, and the averaged correction factors are between 1.05 and 1.20. For external Bremsstrahlung of electrons, the correction factors are between 1.00 and 1.01. Bremsstrahlung of pions is suppressed by a factor of m_e^2/m_π^2 and may be neglected.

Ionisation losses

On their passage through the target material, particles also lose energy by excitations and ionisations of the target molecules and atoms. The strength of this effect (known as Landau energy straggling, originally discussed in [143]) also increases with the target thickness. A common parameterisation of the averaged correction factor is

$$K_{\mathrm{Land}} = \left[\sum_{i=1}^{9} f_i\right]\left[\sum_{i=1}^{9} f_i \,\mathrm{erf}\,(x_i(\Delta E))\right]^{-1},$$

where $\mathrm{erf}(x)$ is the usual probability integral, f_i are known tabulated coefficients, and x_is are functions of ΔE, of the particle's energy E and of the (Z,A) of the target nucleus, and are also parameterised with a known set of coefficients [144].

As in the treatment of energy losses due to Bremsstrahlung, ionisation effects for electrons were incorporated into the acceptance calculation program by directly assigning energy losses to the particles involved. For Landau straggling, the distribution in *deviations* $\lambda \equiv (\Delta E - \Delta E_{mp})/\zeta$ of the actual energy loss ΔE from the most probable energy loss ΔE_{mp} is given by

$$\phi(\lambda) = \frac{1}{\pi}\int_0^\infty dr\, e^{-\lambda r - r\ln r}\,\sin(\pi r)\,, \tag{D.6}$$

and ΔE_{mp} is parameterised in terms of the target's mass number, atomic charge, average ionisation potential, and on the electron's velocity [145]. For pions, the Bethe-Bloch formula was used to estimate ΔE_{mp}. The parameter ζ is linear in the target thickness t and specifies the characteristic shape of the straggling distribution. During the simulation, generated electrons are assigned an energy loss of $\Delta E = \Delta E_{mp} + \lambda\zeta(t)$, where $t = \rho\Delta x$ is calculated from the position of the reaction point and λ is a random number distributed according to (D.6). However, the effects of Landau straggling can be neglected for target thicknesses smaller than 0.05 of the target material's radiation length [137]. With our 2 cm cylindrical target, $t/X_0 \simeq 0.0022$, and with the extended 5 cm target, $t/X_0 \simeq 0.0055$, well below this limit.

E

The DHKT model

In the energy region between the threshold and the Δ-resonance (as in our experiment), the electro-production cross-section becomes sensitive to the low-energy end tails of the lowest nucleon resonances. As a cross-check against our extraction of $G_A(q^2)$, we used an improved version of the DT model described in section 5.2. The DHKT model of Drechsel, Hanstein, Kamalov and Tiator [39] took over the successes of the isobar model of [42], and since resonance features of photo- and electro-production on the nucleon can be clearly distinguished already by observing the cross-sections, it assumes that the leading part of the total production amplitude is equal to the sum of the resonant amplitudes with Breit-Wigner forms, plus some non-resonant 'background'.

The electro-production amplitude is treated in two parts (as in the DT model): the part which describes the coupling of the virtual photon to the nucleon or to the pion, and the part which describes the πNN vertex. The electro-magnetic γNN and $\gamma\pi\pi$ vertices have a well-defined structure

$$\mathcal{L}_{\gamma NN} = -e\overline{\psi}\left[\gamma_\mu A^\mu F_1^{p,n}(q^2) + \frac{\sigma_{\nu\mu}}{2M}\,\partial^\mu A^\nu F_2^{p,n}(q^2)\right]\psi\,,$$
$$\mathcal{L}_{\gamma\pi\pi} = e\left[(\partial_\mu \boldsymbol{\pi})^\dagger \times \boldsymbol{\pi}\right]_3 A^\mu F_\pi(q^2)\,,$$

where A^μ is the electro-magnetic four-vector potential and F_1, F_2 are the usual Dirac-Pauli nucleon form factors (these can be converted to the Sachs form factors G^E and G^M according to (A.5) and (A.6)), and F_π is the pion electro-magnetic form factor. In the DHKT model, gauge invariance is imposed by the simplest requirement

$$G_A(q^2) = F_\pi(q^2) = F_1^v(q^2)\,.$$

The difference with respect to the simpler DT model appears at the πNN vertex, which is far more involved than the electro-magnetic vertex, since it embodies the strong interaction part of the electro-production process. At energies in the vicinity of the threshold, the pseudo-vector (PV) coupling

$$\mathcal{L}_{\pi NN}^{PV} = -\frac{f}{m_\pi}\overline{\psi}\gamma_5\gamma_\mu\boldsymbol{\tau}\partial^\mu\boldsymbol{\pi}\psi$$

of the DT model is sufficient to describe charged pion electro-production. This coupling also reproduces PCAC and is consistent with the low-energy theorems and chiral perturbation theory to the leading order. At higher energies, the pseudo-scalar (PS) coupling

$$\mathcal{L}_{\pi NN}^{PS} = ig\overline{\psi}\gamma_5\boldsymbol{\tau}\boldsymbol{\pi}\psi$$

where $f/m_\pi = g/2M$, is preferred to the pseudo-vector since the PS is renormalisable in the usual manner whereas the PV is not. In the DHKT model, the description of the hadronic part of the process is therefore attempted by a simple form of the mixed coupling

$$\mathcal{L}_{\pi NN} = \frac{\Lambda^2}{\Lambda^2 + q_0^2}\,\mathcal{L}^{PV}_{\pi NN} + \frac{q_0^2}{\Lambda^2 + q_0^2}\,\mathcal{L}^{PS}_{\pi NN}\,,$$

which exhibits a gradual transition from the low-energy 'PV-regime' to the high-energy 'PS-regime'. The q_0 is the asymptotic pion momentum in the centre-of-mass frame of the final πN system, and Λ is the mixing parameter. The value which best fits the $M_{1-}^{(3/2)}$ and $E_{0+}^{(3/2)}$ multipoles (see appendix B for their definitions), is $\Lambda = 450\,\mathrm{MeV}$. However, one should note that in the charged pion channels as in $p(e,e'\pi^+)n$, the multipole E_{0+} which dominates the non-resonant background, is sensitive neither to the choice of the coupling scheme (of the Λ), nor to the re-scattering effects mentioned below.

A relatively new addition to the model are the vector meson exchange terms which are generally much smaller than the Born terms, but in fact bring the $M_{1+}^{(1/2)}$ multipoles into excellent agreement with the data. Vector meson exchange also plays a role in the unitarisation procedure for the isospin-T th component of the electric dipole amplitude

$$E_{0+}^{(T)} \to E_{0+}^{(T)\,\mathrm{Born,VME}}\left(1 + i t_{\pi N}^{(T)}\right),$$

where $t_{\pi N}^{(T)} = [\eta_T \exp(i\delta_{\pi N}^T) - 1]/2i$ is the πN elastic scattering amplitude with the phase shift $\delta_{\pi N}^T$ and η_T is the inelasticity parameter. Using this prescription, the pion-nucleon rescattering effects causing a large imaginary contribution to $E_{0+}^{(T)}$ are taken into account.

Once the non-resonant 'background' is fixed, a certain analytical scheme has to be adopted to determine the resonant contributions to the multipoles. In the DHKT model, the genuine ('*bare*') resonances are thought to interfere with the non-resonant parts of the amplitude, and the effects of this interference show up in the vertex corrections (however, at resonance positions, the contributions of the interference terms are expected to be small). In principle, the individual resonance positions and resonance widths entering the Breit-Wigner parameterisations are known from pion-nucleon scattering, so that the energy dependence of the resonant amplitudes is known in advance. An important additional component of these parameterisations is an unitarity phase factor which has the important role of adjusting the phase of the total amplitude ('background' plus resonance) to the corresponding pion-nucleon scattering phase shift according to the Fermi-Watson theorem.

When the DHKT model is extended to virtual photons, the multipoles and their intrinsic kinematical factors become q^2-dependent. For the small E_{1+} and S_{1+} multipoles in the $T = 3/2$ channel which are relevant to $p(e,e'\pi^+)n$ in the vicinity of the Δ-resonance, the form of this dependence is only poorly known, and it is assumed that it is equal to the q^2-dependence of $M_{1+}^{(3/2)}$. But fortunately this assumption does not affect the unitarisation procedure since the Fermi-Watson theorem requires that neither the phases of the total $M_{1+}^{(3/2)}$, $E_{1+}^{(3/2)}$ and $S_{1+}^{(3/2)}$ multipoles nor the $\Delta(1232)$ resonance position should depend on q^2. Once the unitarisation procedure is carried out, the unitarity phase factor in the Breit-Wigner parameterisation depends on both W and q^2. As a consequence, the total phase of the resonance multipoles is 90° at the resonance position $W = 1232\,\mathrm{MeV}$ and their real parts vanish.

F

The Lagrangians of the LSM and the CDM

The *linear σ-model* (LSM) of the nucleon is a prototype of a phenomenological model incorporating the violation of chiral symmetry and containing the mechanism of its spontaneous breakdown. In its original version [146], the model unified these concepts naturally within the field-theoretical framework of fermion fields ψ coupled to scalar-isoscalar fields σ and pseudoscalar/isovector fields $\boldsymbol{\pi}$, interpreted as nucleons, σ-mesons and pions, respectively. In our calculations, we use an advanced version of the model [116] with the u and d quarks as fermions. The (chirally invariant) Lagrangian density of the LSM is

$$\begin{aligned}\mathcal{L}_0(x) &= i\overline{\psi}\gamma^\mu\partial_\mu\psi - g\overline{\psi}(\sigma + i\boldsymbol{\tau}\cdot\boldsymbol{\pi}\gamma_5)\psi \\ &\quad + \frac{1}{2}(\partial_\mu\sigma)(\partial^\mu\sigma) + \frac{1}{2}(\partial_\mu\boldsymbol{\pi})(\partial^\mu\boldsymbol{\pi}) - \frac{\lambda^2}{4}\left(\boldsymbol{\pi}^2 + \sigma^2 - \nu^2\right)^2 + \mathcal{U}_0\,, \end{aligned} \tag{F.1}$$

where g is the coupling constant of the quark-meson interaction. The quarks (or the nucleons) in the LSM do not acquire their constituent masses through the usual Dirac term $-m_N\overline{\psi}\psi$ since it violates chiral symmetry, but through the chirally invariant interaction term $-g\overline{\psi}(\sigma + i\boldsymbol{\tau}\cdot\boldsymbol{\pi}\gamma_5)\psi$ after the chiral symmetry becomes spontaneously broken as described below. The meson fields additionally enter the Lagrangian density in their individual kinetic terms and in the potential

$$\mathcal{U} = \frac{\lambda^2}{4}\left(\boldsymbol{\pi}^2 + \sigma^2 - \nu^2\right)^2, \tag{F.2}$$

where λ is the coupling constant of the inter-meson interaction. The canonical formalism [147] applied to this Lagrangian density yields the equations of motion for the model particles: the Dirac equation for the quarks coupled to the meson cloud, and a Klein-Gordon equation describing the meson cloud having a potential energy of (F.2) and with a quark core source.

The parameter ν^2 in (F.2) determines the mode in which chiral symmetry is realised within the model. In the *Nambu-Goldstone's* realisation with $\nu^2 > 0$, the vacuum is degenerate and any value of the meson fields satisfying the constraint of the '*chiral circle*' $\sigma^2 + \boldsymbol{\pi}^2 = \nu^2$ minimises the potential energy. We *choose* the solution for which the meson fields fluctuate around their vacuum expectation values $\boldsymbol{\pi} = 0$ and $\sigma_v = +\nu$, and interpret these fluctuations as the actual physical fields. After the shift of fields, the Lagrangian density is still chirally invariant, but the chosen solution, i. e. the chosen realisation of the vacuum, is not. The consequence of this *spontaneous symmetry breakdown* is the quark constituent mass

$$m_q = g\nu\,.$$

Obviously, absolute confinement of quarks can not be achieved in the LSM for finite values of g, and only quarks with energies $E \leq gf_\pi$ are bound.

Since confinement seems to be the dominant feature of the strong interaction at low energies, it motivated [148] to search for a way to introduce its main aspects into chiral soliton models like LSM. In this approach, the interactions of the gluon fields with the scalar field σ of the underlying LSM are represented by the colour dielectric function $\kappa(\sigma)$ which exponentially decreases when the σ field approaches its physical vacuum expectation value. In other words, the non-perturbative vacuum of QCD is understood as a perfect dielectric with $\kappa = 0$ surrounding the $\kappa \neq 0$ region in the interior of the hadron. Such mechanism directly generates the confinement of colour charges: according to the Gauss Law $\nabla \cdot \mathbf{D}^{(a)} = \rho^{(a)}$, an isolated colour charge $\rho^{(a)}$ generates a colour dielectric field $\mathbf{D}^{(a)}(r) \propto 1/r^2$ and its energy $\int d^3\mathbf{r}\, \mathbf{D}^{(a)2}(r)/\kappa(r)$ diverges for $r \to \infty$. These authors have shown how colour-singlet contributions to κ can be derived directly from QCD by averaging over all gluon field configurations. In this approximation $\kappa = (g\chi(r))^4$, where χ is a scalar-isoscalar field.

The extended version of the LSM incorporating the additional field χ became known as the *chiral chromodielectric model* (CDM). Its Lagrangian density [149, 150] differs from the one of the LSM by the additional kinetic and corresponding mass term for the χ field

$$\mathcal{L}_\chi^{\mathrm{CDM}} = \frac{1}{2}(\partial_\mu\chi)(\partial^\mu\chi) - \frac{1}{2}m_\chi^2\chi^2$$

and in the structure of the quark-meson interaction term, in which the (radially dependent) χ acts as a coupling 'constant',

$$\mathcal{L}_{q\pi}^{\mathrm{CDM}} = -\frac{g}{\chi}\overline{\psi}(\sigma + i\boldsymbol{\tau}\cdot\boldsymbol{\pi}\gamma_5)\psi\,. \tag{F.3}$$

The appearance of the χ field in the denominator of (F.3) brings about the dominant feature of the model: the variational procedure in which $\chi(r)$ is self-consistently determined, yields solutions with $\chi(r \to \infty) \to 0$, so that the effective quark mass of $m_q = gv/\chi(r)$ increases with r. It should be noted that unlike in the models with an r^n scalar confining potential, the quark mass is thus *dynamically* generated, and the quarks remain 'confined' (for typical values of the coupling constant, m_q remains below 0.2 GeV and constant for radii smaller than $\simeq 1$ fm, and begins to rise rapidly to a few GeV within the next 1 fm).

Recently, the χ field acquired further phenomenological support. Since χ is a colour singlet field, it is not supposed to simulate the (coloured) gluon fields within the nucleon, but is believed to effectively represent the net effect of colourless gluon clusters known as *scalar glueballs*. In the recent years, there were numerous experimental indications [151, 152] for existence of such clusters with masses around $m_\chi \simeq 1.5$ GeV.

The contribution (F.2) in the LSM and the CDM can be understood as the potential energy of the mesons. When the symmetry is spontaneously broken in the Nambu-Goldstone fashion, the σ-mesons acquire a mass of $(2\lambda^2v^2)^{1/2}$, whereas the pions remain massless. Only when the chiral symmetry of the Lagrangian is additionally *explicitly* broken by a term linear in the σ-field $\mathcal{L}_{\mathrm{sb}} = f_\pi m_\pi^2\sigma(x)$ [146, 147] do the pions acquire a mass. The coefficient $f_\pi m_\pi^2$, where $f_\pi = 93$ MeV is the pion decay constant, is fixed by the PCAC relation [147]. The coupling constant g is the only genuine free parameter of the LSM and CDM. The mass of the pion is taken to be $m_\pi = 139$ MeV, whereas the σ meson is usually identified with the unstable 0^+ meson with a mass of $400 < m_\sigma < 1200$ MeV, decaying predominantly into two pions [24].

G

The model wave-function of the LSM and the CDM

Since the LSM and CDM can not be solved exactly, certain simplifications are made in our version of the models [116]. In the *one radial mode* approximation, we assume that all three quarks of the quark core occupy the same radial state with angular momentum $l = 0$, and that the radial dependence of the pion cloud can be described by a single function $\phi(r)$. The one-particle quark bispinor has the general form

$$q_{nljm_j m_t}(r) = \begin{pmatrix} u_{nlj}(r) \\ i\boldsymbol{\sigma}\cdot\hat{\mathbf{r}}v_{nlj}(r) \end{pmatrix} \sum_{m_l m_s} C^{jm_j}_{lm_l\frac{1}{2}m_s} Y_{lm_l}(\hat{\mathbf{r}})\xi_{m_s m_t} \,.$$

Here, the $\xi_{m_s m_t} = \chi_{\frac{1}{2}m_s}\Phi_{\frac{1}{2}m_t}$ is the spin-isospin part of the wave-function. In the LSM and the CDM, we use a particular ansatz of the form

$$q(r) = \frac{1}{\sqrt{4\pi}} \begin{pmatrix} u(r) \\ i\boldsymbol{\sigma}\cdot\hat{\mathbf{r}}v(r) \end{pmatrix} |\,\xi_{\text{spin-isospin}}\rangle \,, \tag{G.1}$$

where functions $u(r)$ in $v(r)$ are normalised according to

$$N \equiv \int_0^\infty dr\, r^2 (u(r)^2 + v(r)^2) = 1 \,,$$

and the so-called *hedgehog ansatz* is used for the spin-isospin part

$$|\,\xi_{\text{spin-isospin}}\rangle \equiv |\,\xi_{hh}\rangle = \frac{|\,u\downarrow\rangle - |\,d\uparrow\rangle}{\sqrt{2}} \,, \tag{G.2}$$

in which arrows indicate the third spin component of the quarks. It is the principal feature of the hedgehog ansatz that the spin (s^2, m_s) and isospin (t^2, m_t) separately are not good quantum numbers, and that only $m_t = -m_s$ appear in the linear combination (G.2). The three valence quarks in their lowest single-particle states differ only by the quantum numbers of colour. The colour part of the three-quark wave-function (which we omit in the expressions) takes care that the complete wave-function is antisymmetric with respect to the interchange of the quarks; the spin-isospin part and the space part of the wave-function are symmetric. The ansatz for the bare baryon wave-function is then [8]

$$|\,B\rangle = \frac{1}{\sqrt{2}}\Big[\,|\,N\rangle + |\,\Delta\rangle\,\Big] \,.$$

[8] We could introduce an additional *mixing angle* δ, allowing us to mix the bare nucleon states $|N\rangle$ and bare Δ states $|\Delta\rangle$ with relative weights other than $1:1$, like $|B(\delta)\rangle = \cos\delta\,|N\rangle + \sin\delta\,|\Delta\rangle$. In this case, the variation procedure has to be extended to this new degree of freedom, so that the baryon energy is minimised with respect to it.

The mesons in the LSM and the CDM are represented by *coherent states*. The coherent states $|\Sigma\rangle$ of the meson field σ and $|\Pi\rangle$ of the pion field $\boldsymbol{\pi}$ are defined in k-space as eigenstates of the annihilation operators of the individual meson fields [116, 153]. For the expectation value of the pion and the sigma field we choose the *meson hedgehog ansatz*,

$$\pi_t(\mathbf{r}) = \langle \Pi | \hat{\pi}_t | \Pi \rangle = \frac{r_t}{r}\phi(r) \,, \tag{G.3}$$

$$\sigma(\mathbf{r}) = \langle \Sigma | \hat{\sigma} | \Sigma \rangle = \sigma(r) \,. \tag{G.4}$$

Typical solutions for the radial fields obtained in a self-consistent variational calculation are shown in figure G.1.

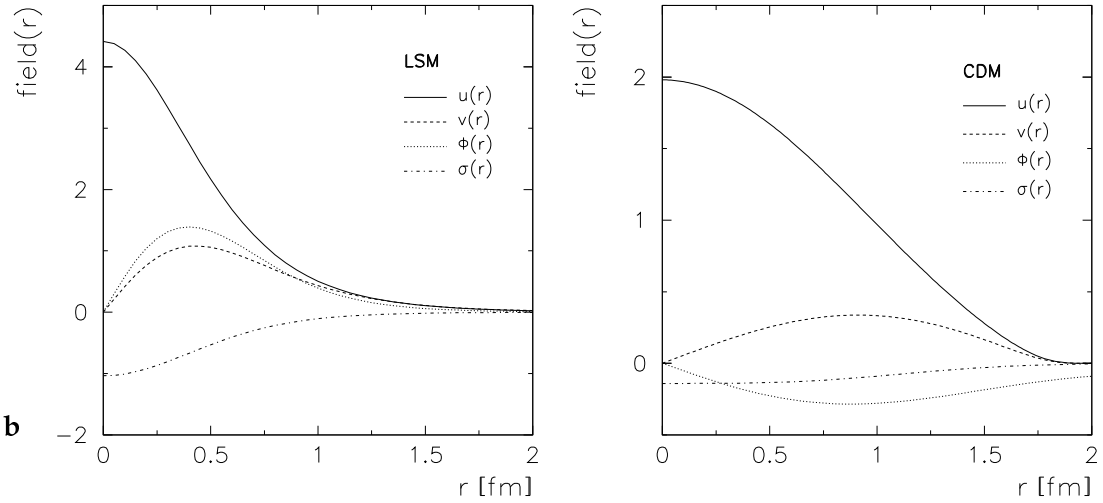

a **b**

Figure G.1: Typical solutions for the radial fields obtained in self-consistent variational calculations **a** – for the LSM, **b** – for the CDM. Note the change of scale on the y-axis of the plots.

The total trial wave-function of the (dressed) baryon is the product of the quark part and of the part describing the meson cloud

$$|\psi_{hh}\rangle = |B(\delta)\rangle \otimes |\Sigma\rangle \otimes |\Pi\rangle \,. \tag{G.5}$$

The overlap matrix elements quoted in (6.8) are given by $F_J = \langle \psi_{hh} | \hat{P}_J | \psi_{hh} \rangle$ and the total baryon energy is equal to the expectation value of the Hamiltonian density $\hat{\mathcal{H}} = \hat{\mathcal{H}}_q + \hat{\mathcal{H}}_{q\sigma} + \hat{\mathcal{H}}_{q\pi} + \hat{\mathcal{H}}_\sigma + \hat{\mathcal{H}}_\pi + \hat{\mathcal{H}}_{\sigma\pi} + (\hat{\mathcal{H}}_\chi^{CDM})$, where all the creation and annihilation operators contained in it are arranged in normal order

$$E = \langle \psi_{hh} | \, : \hat{\mathcal{H}} : \, | \psi_{hh} \rangle \,. \tag{G.6}$$

It is worth stressing that (G.6) is equal to the total baryon energy obtained classically in the mean-field approximation (MFA). All quantum corrections of the individual contributions to (G.6) are eliminated through normal ordering.

H

Evaluation of $G_A(q^2)$ in the LSM and the CDM: technical details

In the LSM and the CDM, the axial current operator contains a quark and a pion contribution

$$\begin{aligned}\hat{A}^{\mu j}(x) &= \hat{A}^{\mu j}_{q}(x) + \hat{A}^{\mu j}_{\sigma\pi}(x) \\ &= \sum_{a} \overline{\psi}_a(x)\gamma^\mu\gamma_5\tfrac{1}{2}\tau_j\psi_a(x) + \sigma(x)\partial^\mu\pi_j(x) - \pi_j(x)\partial^\mu\sigma(x)\end{aligned}$$

where we have used $\psi(x)$ to denote quark spinors and $\sigma(x)$ and $\pi(x)$ represent the σ-meson and the pion fields. The sum runs over all three quarks $1 \leq a \leq 3$ and j is the isospin index. The calculation of $G_A(q^2)$ with the centre-of-mass motion and recoil effects eliminated amounts to the evaluation of the matrix element of $\hat{A}^{\mu j}(x)$ between states of definite spin, isospin and linear momentum, as given in (6.15). To begin with, we rewrite (6.15) by isolating the integrals over $d^3\mathbf{r}$ from the integrals over $d^3\Omega$ and $d^3\mathbf{a}$

$$\begin{aligned}G_A(q^2) = \frac{2}{\mathcal{N}}\Bigg\{ &\sum_{Q=-1}^{1} C_Q \int d^3\mathbf{a}\, d^3\Omega \left[\mathcal{D}^{*\frac{1}{2}}_{-\frac{1}{2}-Q,-\frac{1}{2}}(\Omega)\cdot\widetilde{I}^{3Q} + \mathcal{D}^{*\frac{1}{2}}_{\frac{1}{2}-Q,\frac{1}{2}}(\Omega)\cdot\widetilde{K}^{3Q}\right] \\ &- \sqrt{2\pi}\sum_{Q=-1}^{1} C_Q \int d^3\mathbf{a}\, d^3\Omega \left[\mathcal{D}^{*\frac{1}{2}}_{-\frac{1}{2}-Q,-\frac{1}{2}}(\Omega)\cdot\widetilde{J}^{3Q} + \mathcal{D}^{*\frac{1}{2}}_{\frac{1}{2}-Q,\frac{1}{2}}(\Omega)\cdot\widetilde{L}^{3Q}\right] \Bigg\},\end{aligned}$$

where we have abbreviated the j_0 and j_2 quark/meson contributions by

$$\begin{aligned}\widetilde{I}/\widetilde{K}^{3Q}(\Omega,\mathbf{a}) &= \int d^3\mathbf{r}\, j_0(qr)\left\langle \hat{U}(-\tfrac{1}{2}\mathbf{a})\psi_{hh}\,\middle|\,\hat{A}^{3Q}_{q/\sigma\pi}(\mathbf{r})\,\middle|\,\hat{U}(\tfrac{1}{2}\mathbf{a})R(\Omega)\psi_{hh}\right\rangle, \\ \widetilde{J}/\widetilde{L}^{3Q}(\Omega,\mathbf{a}) &= \int d^3\mathbf{r}\, j_2(qr)\left\langle \hat{U}(-\tfrac{1}{2}\mathbf{a})\psi_{hh}\,\middle|\,\left[Y_2(\hat{\mathbf{r}})\otimes\hat{\mathbf{A}}^{Q}_{q/\sigma\pi}(\mathbf{r})\right]_{10}\,\middle|\,\hat{U}(\tfrac{1}{2}\mathbf{a})R(\Omega)\psi_{hh}\right\rangle.\end{aligned}$$

H.1 The quark contribution to the term with $j_0(qr)$

As suggested in [123], the first step is to perform the rotation of the hedgehog in isospin space, so that the matrix element $\widetilde{I}^{3Q}(\Omega,\mathbf{a})$ can be reduced to the expectation value between the quark hedgehog states (G.2)

$$\begin{aligned}\widetilde{I}^{3Q}(\Omega,\mathbf{a}) &= \int d^3\mathbf{r}\, j_0(qr)\left\langle \hat{U}(-\tfrac{1}{2}\mathbf{a})\psi_{hh}\,\middle|\,\hat{A}^{3Q}_{q}(\mathbf{r})\,\middle|\,\hat{U}(\tfrac{1}{2}\mathbf{a})R(\Omega)\psi_{hh}\right\rangle \\ &= 3n_q^2(a)\,\mathcal{N}_q^2(\Omega)\,n_\pi(a)\,\mathcal{N}_\pi(\Omega,\mathbf{a})\,n_\sigma(a)\,I^{3Q}(\Omega,\mathbf{a}),\end{aligned}$$

where the ns and the $\mathcal{N}$s are functions of Ω and $\mathbf{a}$, as given in the equation group (D.30) of [123]. In short, $\mathcal{N}_q$ is a function of the Euler angles Ω only, whereas $\mathcal{N}_\pi$ depends in a rather complicated way on the double Fourier transform of the pion field $\phi(r)$ and can be related to the total number of pions in the model. The n_q, n_π and n_σ are also double Fourier transforms of $u(r)$ and $v(r)$, $\phi(r)$ and $\sigma(r)$, respectively. In practice, they are calculated numerically from the model fields obtained in the variation. The portion of the amplitude pertaining to the axial current operator is enclosed in $I^{3Q}(\Omega, \mathbf{a})$, where

$$I^{mQ}(\Omega, \mathbf{a}) = \int d^3\mathbf{r}\, j_0(qr) \left\langle \xi_{hh} \,\middle|\, \overline{q}(r_+)\gamma^m\gamma_5 \frac{\tau_Q}{2} q(r_-) \,\middle|\, R(\Omega)\xi_{hh} \right\rangle ,$$

with $r_\pm$ defined in (6.16). To perform the integration over azimuthal angles, the $\mathbf{r} = (x, y, z)$ system is rotated in such a way that the z' axis of the new system is aligned with $\mathbf{a}$,

$$\begin{aligned} x &= x' , \\ y &= \cos\gamma\, y' + \sin\gamma\, z' , \\ z &= -\sin\gamma\, y' + \cos\gamma\, z' . \end{aligned}$$

There is no loss of generality in this particular choice since the integral over directions of $\mathbf{a}$ still has to be performed. The integrand is rewritten in terms of the variables in the primed system and it is easy to see that on symmetry grounds, 'odd' terms containing $r'_i r'_j$ with $i \neq j$ vanish, and only terms with $i = j$ contribute to the integral. Using the formula

$$\begin{aligned} \int d\hat{\mathbf{r}}\, \hat{r}_i \hat{r}_j\, f(a\mathbf{r}) &= \delta_{ij} G(a) + \hat{a}_i \hat{a}_j \Big[F(a) - G(a) \Big] , \qquad \text{(H.1)} \\ F(a) &= 2\pi \int_{-1}^{1} dx\, x^2\, f(r, a, x) , \\ G(a) &= \pi \int_{-1}^{1} dx\, (1 - x^2)\, f(r, a, x) , \end{aligned}$$

in which x was redeclared to the variable denoting the cosine of the relative polar angle between $\mathbf{r}$ and $\mathbf{a}$ in accordance with (6.16), we obtain

$$I^{3Q}(\Omega, \mathbf{a}) = A_0 \left\langle \xi_{hh} \,\middle|\, \sigma_3 \tfrac{1}{2}\tau_Q \,\middle|\, R(\Omega)\xi_{hh} \right\rangle + A_2 \sum_k \hat{a}_3 \hat{a}_k \left\langle \xi_{hh} \,\middle|\, \sigma_k \tfrac{1}{2}\tau_Q \,\middle|\, R(\Omega)\xi_{hh} \right\rangle$$

with

$$\begin{aligned} A_0 &= \frac{1}{2} \int_0^\infty dr\, r^2\, j_0(qr) \int_{-1}^{1} dx \left[u(r_+)u(r_-) - \frac{v(r_+)v(r_-)}{r_+ r_-} \left(r^2 x^2 - \frac{a^2}{4} \right) \right] , \\ A_2 &= \frac{1}{2} \int_0^\infty dr\, r^2\, j_0(qr) \int_{-1}^{1} dx\, \frac{v(r_+)v(r_-)}{r_+ r_-} \left(r^2(3x^2 - 1) - \frac{a^2}{2} \right) . \end{aligned}$$

H.2 The quark contribution to the term with $j_2(qr)$

We proceed in an analogous manner in calculating the j_2 contribution

$$\begin{aligned} \widetilde{J}^{3Q}(\Omega, \mathbf{a}) &= \int d^3\mathbf{r}\, j_2(qr) \left\langle \hat{U}(-\tfrac{1}{2}\mathbf{a})\psi_{hh} \,\middle|\, \Big[Y_2(\hat{\mathbf{r}}) \otimes \hat{\mathbf{A}}^Q_q(\mathbf{r}) \Big]_{10} \,\middle|\, \hat{U}(\tfrac{1}{2}\mathbf{a}) R(\Omega)\psi_{hh} \right\rangle \\ &= 3 n_q^2(a) \mathcal{N}_q^2(\Omega) n_\pi(a) \mathcal{N}_\pi(\Omega, \mathbf{a}) n_\sigma(a) \sum_m J^{mQ}(\Omega, \mathbf{a}) \end{aligned}$$

with

$$J^{mQ}(\Omega,\mathbf{a}) = \int d^3\mathbf{r}\, j_2(qr) \left\langle \xi_{hh} \,\middle|\, \overline{q}(r_+)\gamma^m\gamma_5\frac{\tau_Q}{2}\, C^{10}_{2-m1m}\, Y_{2-m}(\hat{\mathbf{r}})\, q(r_-) \,\middle|\, R(\Omega)\xi_{hh}\right\rangle .$$

Fortunately, the spherical harmonic Y_{2-m} does not cause any problems, since the summation over m generates contributions of the same type as in I^{mQ} when we calculate the integral over the azimuthal angle. This can be seen by explicitly writing the Y_{2-m} in terms of coordinates in the spherical basis, and weighting the sum with the corresponding Clebsch-Gordan coefficients. We get

$$\sum_m J^{mQ}(\Omega,\mathbf{a}) = B_0 \left\langle \xi_{hh} \,\middle|\, \sigma_3\tfrac{1}{2}\tau_Q \,\middle|\, R(\Omega)\xi_{hh}\right\rangle + B_2 \sum_k \hat{a}_3\hat{a}_k \left\langle \xi_{hh} \,\middle|\, \sigma_k\tfrac{1}{2}\tau_Q \,\middle|\, R(\Omega)\xi_{hh}\right\rangle$$

where

$$B_0 = -\frac{1}{\sqrt{8\pi}}\int_0^\infty dr\, r^2\, j_2(qr) \int_{-1}^1 dx \left\{ \left[\frac{u(r_+)u(r_-)}{4} - \frac{v(r_+)v(r_-)}{4r_+r_-}\left(r^2-\frac{a^2}{4}\right)\right]\left[1-3x^2\right] + \frac{v(r_+)v(r_-)}{r_+r_-}\, r^2(1-x^2)\right\},$$

$$B_2 = -\frac{1}{\sqrt{8\pi}}\int_0^\infty dr\, r^2\, j_2(qr) \int_{-1}^1 dx \left[\frac{3u(r_+)u(r_-)}{4} + \frac{v(r_+)v(r_-)}{4r_+r_-}\left(r^2-\frac{a^2}{4}\right)\right]\left[3x^2-1\right].$$

What remains to be done are the integrals over $d^3\mathbf{a}$ and $d^3\Omega$. As it has been shown in [123], the integration over the Euler angles can be done analytically only if $\mathbf{a}$ is substituted by $\mathbf{a} \to T^{-1}(\Omega')\,\mathbf{a}$ with T defined by a similarity transformation $T(\Omega')R(\Omega)T^{-1}(\Omega') = R_z(\phi)$ which transforms the bilinear form $\hat{\mathbf{a}}^T R(\Omega)\hat{\mathbf{a}}$ into the form $\hat{\mathbf{a}}^T R_z(\phi)\hat{\mathbf{a}}$, where $R_z(\phi)$ corresponds to a rotation for an angle of ϕ about the z-axis. Then $\int d^3\mathbf{a} = \int da\, a^2\, d(\cos\theta_{\mathbf{a}})\, d\phi_{\mathbf{a}}$, where the final integrals over da and $d(\cos\theta_{\mathbf{a}})$ have to be done numerically. For the A_0 and the B_0 terms, the integration over $\phi_{\mathbf{a}}$ is trivial (2π) and we get

$$\frac{1}{2\pi^2}\int d^3\Omega \int d\phi_{\mathbf{a}}\, \mathcal{D}^{*\frac{1}{2}}_{-\frac{1}{2}-Q,-\frac{1}{2}}(\Omega)\, \mathcal{N}_q^2(\Omega)\, \mathcal{N}_\pi(\Omega,z) \left\langle \xi_{hh} \,\middle|\, \sigma_3\tfrac{1}{2}\tau_Q \,\middle|\, R(\Omega)\xi_{hh}\right\rangle$$
$$= \begin{cases} -2\pi\,\dfrac{e^{-z}}{z}\left[I_1(z)+I_2(z)\right] & Q=0\,, \\ \dfrac{2\sqrt{2}\pi}{3}\,\dfrac{e^{-z}}{z}\left[I_1(z)-I_2(z)\right] & Q=-1\,, \end{cases}$$

where $I_j(z)$ are the modified Bessel functions of the second kind, z is given by (H.5) and where only the terms depending on Ω were considered for reasons of clarity. In the A_2 and the B_2 terms, however, also the $\hat{\mathbf{a}}_3\hat{\mathbf{a}}_k$ depend on $\phi_{\mathbf{a}}$ and one first performs this integration using

$$\int d\phi_{\mathbf{a}}\, \hat{\mathbf{a}}_i(\Omega)\hat{\mathbf{a}}_j(\Omega) = C_{ij}(\Omega,s) \tag{H.2}$$

given by the equation group (N.16) of [123]. This yields

$$\frac{1}{2\pi^2}\int d^3\Omega\ \mathcal{D}^{*\frac{1}{2}}_{-\frac{1}{2}-Q,-\frac{1}{2}}(\Omega)\, \mathcal{N}_q^2(\Omega)\, \mathcal{N}_\pi(\Omega,z) \sum_k C_{3k}(\Omega,s) \left\langle \xi_{hh} \,\middle|\, \sigma_k\tfrac{1}{2}\tau_Q \,\middle|\, R(\Omega)\xi_{hh}\right\rangle$$
$$= \begin{cases} -\dfrac{2\pi}{3}\,\dfrac{e^{-z}}{z}\left[I_1(z)+I_2(z)\right] & Q=0\,, \\ \dfrac{\sqrt{2}\pi}{3}\dfrac{e^{-z}}{z}\left[I_1(z)-I_2(z)\right](1-s^2) & Q=-1\,. \end{cases}$$

Putting all the pieces together, summing over Q with the appropriate C_Q coefficients as specified in (6.15), and dividing out the normalisation overlap $\mathcal{N}$, we obtain the final expression for the quark contribution to the axial form factor

$$\begin{aligned} G_A^{(q)}(q^2) &= \frac{1}{3}\frac{\int_0^\infty da\, a^2\, n^{(2)}(a)\, A_{q0}(a) \int_0^1 ds\, (e^{-z}/z)\left[5I_1(z)+I_2(z)\right]}{\int_0^\infty da\, a^2\, n^{(3)}(a)\, j_0(\frac{1}{2}qa)\int_0^1 ds\,(e^{-z}/z)\left[I_1(z)+I_2(z)\right]} \\ &+ \frac{4}{9}\frac{\int_0^\infty da\, a^2\, n^{(2)}(a)\, A_{q2}(a) \int_0^1 ds\, (e^{-z}/z)\, P_2(s)\left[I_1(z)-I_2(z)\right]}{\int_0^\infty da\, a^2\, n^{(3)}(a)\, j_0(\frac{1}{2}qa)\int_0^1 ds\,(e^{-z}/z)\left[I_1(z)+I_2(z)\right]}\,, \end{aligned} \tag{H.3}$$

where we have identified $n^{(i)}(a) \equiv n_q^i(a)\, n_\pi(a)\, n_\sigma(a)$ and where

$$\begin{aligned} A_{q0}(a) &= \left(A_0 - \sqrt{2\pi}\,B_0\right) + \tfrac{1}{3}\left(A_2 - \sqrt{2\pi}\,B_2\right), \\ A_{q2}(a) &= -\tfrac{1}{2}\left(A_2 - \sqrt{2\pi}\,B_2\right), \end{aligned}$$

and all remaining integrals have to be performed numerically. To check the static limit of our results against the results of [123] which were obtained in a completely different way, by evaluating the expectation values between rotated and translated hedgehog states in k-space, we have to use these relations with A_0, A_2, B_0 and B_2 evaluated at $q = |\mathbf{q}| = 0$.

H.3 The meson contribution to the term with $j_0(qr)$

To calculate the contributions of the meson cloud, we have to evaluate the expectation value of the axial current operator $\sigma(x)\partial^\mu\pi_j(x) - \pi_j(x)\partial^\mu\sigma(x)$ between rotated and translated hedgehog states. Using partial integration it is easy to show that the expectation values of the two terms of this operator differ only by a sign, so either of them is sufficient to obtain the complete matrix element. For convenience, we chose the second term, so that

$$\begin{aligned} \widetilde{K}^{3Q}(\Omega, \mathbf{a}) &= \int d^3\mathbf{r}\, j_0(qr) \left\langle \hat{U}(-\tfrac{1}{2}\mathbf{a})\psi_{hh} \right| \hat{A}^{3Q}_{\sigma\pi}(\mathbf{r}) \left| \hat{U}(\tfrac{1}{2}\mathbf{a})R(\Omega)\psi_{hh} \right\rangle \\ &= -2\int d^3\mathbf{r}\, j_0(qr) \left\langle \hat{U}(-\tfrac{1}{2}\mathbf{a})\psi_{hh} \right| : \pi_Q(\mathbf{r})\partial^3\sigma(\mathbf{r}) : \left| \hat{U}(\tfrac{1}{2}\mathbf{a})R(\Omega)\psi_{hh} \right\rangle . \end{aligned}$$

We insert the plane-wave expansions

$$\begin{aligned} \partial^j\sigma(\mathbf{r}) &= -i\,\frac{1}{(2\pi)^{3/2}}\int d^3\mathbf{k}\,\frac{1}{(2\omega_\sigma)^{1/2}}\,k_j\left[a(k)e^{i\mathbf{kr}} - a^\dagger(k)e^{-i\mathbf{kr}}\right], \\ \pi_Q(\mathbf{r}) &= \frac{1}{(2\pi)^{3/2}}\int d^3\mathbf{k}\,\frac{1}{(2\omega_\pi)^{1/2}}\left[b_Q(\mathbf{k})e^{i\mathbf{kr}} + b_Q^\dagger(\mathbf{k})e^{-i\mathbf{kr}}\right], \end{aligned}$$

and make use of the fact that a translated and/or rotated hedgehog state is still a hedgehog state, i. e. for the pion fields

$$\begin{aligned} b_Q(\mathbf{k}')\left|\hat{U}(\mathbf{x})R(\Omega)\psi_{hh}\right\rangle &= \sqrt{\frac{\omega_\pi(\mathbf{k}')}{2}}\sum_{k=1}^{3}\mathcal{R}^{-1}_{Qk}(\Omega)\xi_k(\mathbf{k}')e^{-i\mathbf{k}'\mathbf{x}}\left|\hat{U}(\mathbf{x})R(\Omega)\psi_{hh}\right\rangle, \\ \left\langle\psi_{hh}\hat{U}(\mathbf{x})\right| b_Q^\dagger(\mathbf{k}') &= \left\langle\psi_{hh}\hat{U}(\mathbf{x})\right|\sqrt{\frac{\omega_\pi(\mathbf{k}')}{2}}\,\xi_Q^*(\mathbf{k}')e^{i\mathbf{k}'\mathbf{x}}, \end{aligned}$$

and analogously for the σ-meson fields

$$a(k)\left|\,\hat{U}(x)R(\Omega)\psi_{hh}\right\rangle = \sqrt{\frac{\omega_\sigma(k)}{2}}\eta(k)e^{-ikx}\left|\,\hat{U}(x)R(\Omega)\psi_{hh}\right\rangle,$$
$$\left\langle\psi_{hh}\hat{U}(x)\right|a^\dagger(k) = \left\langle\psi_{hh}\hat{U}(x)\right|\sqrt{\frac{\omega_\sigma(k)}{2}}\eta(k)e^{ikx},$$

where we have used

$$\xi_Q(k) = -i\,\hat{k}_Q\sqrt{\frac{2}{\pi}}\int dr\,r^2 j_1(kr)\phi(r) \equiv -i\,\hat{k}_Q A(k),$$
$$\eta(k) = \sqrt{\frac{2}{\pi}}\int dr\,r^2 j_0(kr)\sigma(r).$$

Applying the relation $\int d\hat{k}\,\hat{k}_j\,e^{\pm ikr_\mp} = \pm 4\pi i\,\hat{r}_{\mp j}\,j_1(kr_\mp)$, the resulting expressions can then be integrated over $d\hat{k}$ and $d\hat{k}'$. We obtain (note the $n_q^3(a)\,\mathcal{N}_q^3(\Omega)$ factor appearing in the expression instead of the $3n_q^2(a)\,\mathcal{N}_q^2(\Omega)$ factor in the quark contribution where two of the quarks were acting as spectators)

$$\tilde{K}^{jQ}(\Omega,\mathbf{a}) = n_q^3(a)\,\mathcal{N}_q^3(\Omega)\,n_\pi(a)\,\mathcal{N}_\pi(\Omega,\mathbf{a})\,n_\sigma(a)\,K^{jQ}(\Omega,\mathbf{a}),$$

where

$$K^{jQ}(\Omega,\mathbf{a}) = -2\int d^3\mathbf{r}\,j_0(qr)\,\frac{1}{2\pi}\sum_{k=1}^{3}\left[\hat{r}_{+j}C(r_+) + \hat{r}_{-j}C(r_-)\right]\left[\mathcal{R}^{-1}_{Qk}\hat{r}_{-k}D(r_-) + \delta_{Qk}\hat{r}_{+k}D(r_+)\right],$$

and where we have used $C(r)$ and $D(r)$ to denote double Fourier-transforms of the meson fields. From the recurrence relations for the spherical Bessel functions, it is easy to see that these transforms reduce to the original radial fields, i. e.

$$C(r) = \int dk\,k^3 j_1(kr)\,\eta(k) \equiv -\sqrt{\frac{\pi}{2}}\,\frac{d\sigma(r)}{dr},$$
$$D(r) = \int dk\,k^2 j_1(kr)\,A(k) \equiv \sqrt{\frac{\pi}{2}}\,\phi(r).$$

When individual pieces are decomposed using (6.16) and conveniently regrouped, the angular integral over the azimuthal angle of $\mathbf{a}$ can be performed according to (H.1). Care must be taken that terms of the form $C(r)D(r)r_i a_j$ in general neither vanish nor cancel with the terms of the form $C(r)D(r)a_i r_j$. We finally obtain

$$K^{3Q}(\Omega,\mathbf{a}) = -2\left[C_0\left(\mathcal{R}_{3Q}(\Omega)+\delta_{Q3}\right) + C_2\sum_k \hat{a}_3\hat{a}_k\left(\mathcal{R}_{kQ}(\Omega)+\delta_{Qk}\right)\right]$$

with

$$C_0 = \frac{1}{2}\int_0^\infty dr\,r^2\,j_0(qr)\int_{-1}^{1}dx\quad\left(\frac{C(r_+)D(r_-)}{r_+r_-}+\frac{C(r_-)D(r_-)}{r_-^2}\right)r^2(1-x^2),$$
$$C_2 = \frac{1}{2}\int_0^\infty dr\,r^2\,j_0(qr)\int_{-1}^{1}dx\left[\left(\frac{C(r_+)D(r_-)}{r_+r_-}+\frac{C(r_-)D(r_-)}{r_-^2}\right)r^2(3x^2-1)\right.$$
$$\left.+\frac{1}{2}\left(\frac{C(r_-)D(r_-)}{r_-^2}-\frac{C(r_+)D(r_-)}{r_+r_-}\right)a^2+2\,\frac{C(r_+)D(r_+)}{r_+^2}\,rax\right].$$

H.4 The meson contribution to the term with $j_2(qr)$

We proceed analogously in calculating the j_2 term of the meson contribution

$$\tilde{L}^{3Q}(\Omega,\mathbf{a}) = n_q^3(a)\,\mathcal{N}_q^3(\Omega)\,n_\pi(a)\,\mathcal{N}_\pi(\Omega,\mathbf{a})\,n_\sigma(a)\sum_m L^{mQ}(\Omega,\mathbf{a})\,,$$

with

$$\begin{aligned} L^{mQ}(\Omega,\mathbf{a}) \;=\; & -2\int d^3\mathbf{r}\, j_2(qr)\,\frac{1}{2\pi}\sum_k C^{10}_{2-m1m}\,Y_{2-m}(\hat{\mathbf{r}}) \\ & \cdot\Big[\hat{r}_{+m}C(r_+)+\hat{r}_{-m}C(r_-)\Big]\Big[\mathcal{R}^{-1}_{Qk}\hat{r}_{-k}D(r_-)+\delta_{Qk}\hat{r}_{+k}D(r_+)\Big]\,. \end{aligned}$$

After the spherical harmonic Y_{2-m} is written out explicitly in terms of coordinates in the spherical basis, the resulting expression for $L^{mQ}(\Omega,\mathbf{a})$ can be integrated over the azimuthal angle of $\mathbf{a}$ using the formula

$$\begin{aligned} \int d\hat{\mathbf{r}}\,\hat{r}_i\hat{r}_j\hat{r}_k\hat{r}_l\,f(a\mathbf{r}) \;=\; & \hat{a}_i\hat{a}_j\hat{a}_k\hat{a}_l\Big[H(a)-6F(a)+G(a)\Big]+\tfrac{1}{3}\Big[\delta_{ij}\delta_{kl}+\delta_{ik}\delta_{jl}+\delta_{il}\delta_{jk}\Big]G(a) \\ & +\Big[\delta_{ij}\hat{a}_k\hat{a}_l+\delta_{kl}\hat{a}_i\hat{a}_j+\delta_{ik}\hat{a}_j\hat{a}_l+\delta_{jl}\hat{a}_i\hat{a}_k+\delta_{il}\hat{a}_j\hat{a}_k+\delta_{jk}\hat{a}_i\hat{a}_l\Big]\Big[F(a)-\tfrac{1}{3}G(a)\Big]\,, \\ F(a) \;=\; & \pi\int_{-1}^{1}dx\,x^2(1-x^2)\,f(r,a,x)\,, \\ G(a) \;=\; & \frac{3\pi}{4}\int_{-1}^{1}dx\,(1-x^2)^2\,f(r,a,x)\,, \\ H(a) \;=\; & 2\pi\int_{-1}^{1}dx\,x^4\,f(r,a,x) \end{aligned}$$

After some book-keeping algebra, the j_2 contribution can be brought into the same form as the j_0 contribution, but with different coefficients involving integrals of $C(r)$ and $D(r)$. We obtain

$$L^{3Q}(\Omega,\mathbf{a}) = -2\Big[D_0\Big(\mathcal{R}_{3Q}(\Omega)+\delta_{Q3}\Big)+D_2\sum_k\hat{a}_3\hat{a}_k\Big(\mathcal{R}_{kQ}(\Omega)+\delta_{Qk}\Big)\Big]$$

with

$$\begin{aligned} D_0 \;=\; & -\frac{1}{\sqrt{8\pi}}\int_0^\infty dr\,r^2\,j_2(qr)\int_{-1}^{1}dx\Bigg[\quad\Big(\frac{C(r_+)D(r_-)}{r_+r_-}+\frac{C(r_-)D(r_-)}{r_-^2}\Big)\,r^2\,(1-x^2) \\ & +\frac{3}{4}\Big(\frac{C(r_+)D(r_-)}{r_+r_-}-\frac{C(r_-)D(r_-)}{r_-^2}\Big)\,rax\,(1-x^2)\Bigg]\,, \\ D_2 \;=\; & -\frac{1}{\sqrt{8\pi}}\int_0^\infty dr\,r^2\,j_2(qr)\int_{-1}^{1}dx\Bigg[\quad\Big(\frac{C(r_+)D(r_-)}{r_+r_-}+\frac{C(r_-)D(r_-)}{r_-^2}\Big)\,r^2\,(3x^2-1) \\ & -\frac{1}{4}\Big(\frac{C(r_+)D(r_-)}{r_+r_-}-\frac{C(r_-)D(r_-)}{r_-^2}\Big)\,a^2\,(3x^2-1) \\ & -\frac{9}{4}\frac{C(r_+)D(r_-)}{r_+r_-}\,rax\,(1-x^2)-\frac{1}{4}\frac{C(r_-)D(r_-)}{r_-^2}\,rax\,(9x^2-1)\Bigg]\,. \end{aligned}$$

As in the quark contribution, the remaining task is to perform the integrals over $d^3\mathbf{a}$ and $d^3\Omega$. The integration over the Euler angles can be done analytically if $\mathbf{a}$ is substituted by

$\mathbf{a} \to T^{-1}(\Omega')\,\mathbf{a}$ with T defined by a similarity transformation $T(\Omega')R(\Omega)T^{-1}(\Omega') = R_z(\phi)$ which transforms the bilinear form $\hat{\mathbf{a}}^T R(\Omega)\hat{\mathbf{a}}$ into the form $\hat{\mathbf{a}}^T R_z(\phi)\hat{\mathbf{a}}$, where $R_z(\phi)$ corresponds to a rotation for an angle of ϕ about the z-axis. For the C_0 and the D_0 terms, the integration over $\phi_{\mathbf{a}}$ is again trivial (2π) and we get

$$\frac{1}{4\pi^2}\int d^3\Omega \int d\phi_{\mathbf{a}}\, \mathcal{D}^{*\frac{1}{2}}_{\frac{1}{2}-Q,\frac{1}{2}}(\Omega)\,\mathcal{N}_q^3(\Omega)\,\mathcal{N}_\pi(\Omega,z)\left[\mathcal{R}_{3j}(\Omega)+\delta_{3j}\right]_Q^1$$
$$= \begin{cases} -\dfrac{\sqrt{2}\pi}{2}\dfrac{e^{-z}}{z}\left[I_1(z)-I_3(z)\right] & Q=+1\,, \\ \pi\dfrac{e^{-z}}{z}\left[3I_1(z)+4I_2(z)+I_3(z)\right] & Q=0\,. \end{cases}$$

In the C_2 and the D_2 terms, the $\hat{\mathbf{a}}_3\hat{\mathbf{a}}_k$ depend on $\phi_{\mathbf{a}}$ and the integration is again performed using (H.2) and taking the appropriate spherical components

$$C^{(1)}_{\pm 1k}(\Omega,s) \equiv \mp\frac{1}{\sqrt{2}}\left[C_{1k}(\Omega,s) \pm i\, C_{2k}(\Omega,s)\right].$$

Together with $C^{(1)}_{0k}(\Omega,s) = C_{3k}(\Omega,s)$ this yields

$$\frac{1}{4\pi^2}\int d^3\Omega\ \mathcal{D}^{*\frac{1}{2}}_{\frac{1}{2}-Q,\frac{1}{2}}(\Omega)\,\mathcal{N}_q^3(\Omega)\,\mathcal{N}_\pi(\Omega,z)\sum_k C^{(1)}_{Qk}(\Omega,s)\left[\mathcal{R}_{k3}(\Omega)+\delta_{k3}\right]$$
$$= \begin{cases} -\dfrac{\sqrt{2}\pi}{4}\dfrac{e^{-z}}{z}\left[I_1(z)-I_3(z)\right](1-s^2) & Q=+1\,, \\ \dfrac{\pi}{6}\dfrac{e^{-z}}{z}\left[3s^2\left(I_1(z)-I_3(z)\right)+5I_1(z)+8I_2(z)+3I_3(z)\right] & Q=0\,. \end{cases}$$

Putting all the pieces together, summing over Q with the appropriate C_Q coefficients as specified in (6.15), and dividing out the normalisation overlap $\mathcal{N}$, we obtain the final expression for the meson contribution to the axial form factor

$$G_A^{(m)}(q^2) = \frac{4}{9}\,\frac{\int_0^\infty da\, a^2\, n^{(3)}(a)\, A_{m0}(a)\int_0^1 ds\,(e^{-z}/z)\left[I_1(z)+I_2(z)\right]}{\int_0^\infty da\, a^2\, n^{(3)}(a)\, j_0(\frac{1}{2}qa)\int_0^1 ds\,(e^{-z}/z)\left[I_1(z)+I_2(z)\right]}\,, \tag{H.4}$$

where

$$A_{m0}(a) = 6\left(C_0-\sqrt{2\pi}\,D_0\right)+2\left(C_2-\sqrt{2\pi}\,D_2\right),$$
$$A_{m2}(a) = -2\left(C_2-\sqrt{2\pi}\,D_2\right),$$

and all remaining integrals have to be performed numerically (note that only $A_{m0}(a)$ is needed to calculate the meson contribution). To check the static limit of our results against the results of [123], these relations have to be used with C_0, C_2, D_0 and D_2 evaluated at $q = |\mathbf{q}| = 0$. The complete expression for the axial form factor is obtained by adding the quark contribution (H.3) and the meson contribution (H.4).

H.5 The norm overlap

Apart from a j_0 factor, the norm overlap $\mathcal{N}$ between the translated and rotated hedgehog states is equal to the one obtained in the static limit [123], i. e.

$$\mathcal{N} = \int d^3\mathbf{a}\, d^3\Omega\, \mathcal{D}^{*\frac{1}{2}}_{\frac{1}{2},\frac{1}{2}}(\Omega)\, j_0\Big(\frac{qa}{2}\Big)\left\langle \psi_{hh}\,\middle|\,\hat{U}(\mathbf{a})\,R(\Omega)\,\middle|\,\psi_{hh}\right\rangle$$

$$= 8\pi^3 \int_0^\infty da\, a^2\, n_q^3(a)\, n_\pi(a)\, n_\sigma(a)\, j_0\Big(\frac{qa}{2}\Big) \int_{-1}^{1} ds\, \frac{e^{-z}}{z} \Big[\, I_1(z) + I_2(z) \Big]\,,$$

where s is the cosine of the polar angle between $\mathbf{a}$ and $\mathbf{q}$, and

$$z = \frac{2}{3}\Big[\, f_0^\pi(a) + P_2(s) f_2^\pi(a) \Big] \tag{H.5}$$

is expressed in terms of the Legendre polynomial $P_2(s)$ and

$$f_l^\pi(a) \;=\; 2\pi \int dk\, k^2\, j_l(ka)\, \omega_\pi(k)\, A^2(k)\,,$$
$$A(k) \;=\; \sqrt{\frac{2}{\pi}} \int dr\, r^2\, j_1(kr) \phi(r)\,.$$

References

[1] H. Tyren, P. Hillman, Th. A. J. Maris, *High energy* $(p, 2p)$ *reactions and proton binding energies*, Nucl. Phys. **7** (1958) 10.

[2] B. Kundu, B. K. Jain, A. B. Santra, *The elementary* $p(p, p'\pi^+)n$ *reaction*, Preprint nucl-th/9806077.

[3] A. D. Hancock et al., *Asymmetries and cross sections for the reaction* $\vec{p} + p \to p + \pi^+ + n$ *at* 800 MeV, Phys. Rev. C **27** (1983) 2742.

[4] U. Amaldi et al., *Inner-shell proton binding energies in* ^{12}C *and* ^{27}Al *from the* $(e, e'p)$ *reaction using* 550 MeV *electrons*, Phys. Rev. Lett. **13** (1964) 341.

[5] G. Bardin et al., *A transverse and longitudinal cross-section separation in a* π^+*–electroproduction coincidence experiment and the pion radius*, Nucl. Phys. B **120** (1977) 45.

[6] E. Amaldi, S. Fubini, G. Furlan, *Pion-electroproduction: electroproduction at low energy and hadron form factors*, Springer Tracts in Modern Physics **83**, Springer Verlag, Berlin 1979.

[7] F. J. Ynduráin, *The theory of quark and gluon interactions*, Texts and Monographs in Physics, Springer Verlag, Berlin 1993.

[8] U.–G. Meißner, *Recent developments in chiral perturbation theory*, Rep. Prog. Phys. **56** (1993) 903.

[9] G. Fanourakis et al., *Study of low-energy antineutrino interactions on protons*, Phys. Rev. D **21** (1980) 562.

[10] L. A. Ahrens et al., *Measurement of neutrino-proton and antineutrino-proton elastic scattering*, Phys. Rev. D **35** (1987) 785.

[11] L. A. Ahrens et al., *A study of the axial-vector form factor and second-class currents in antineutrino quasielastic scattering*, Phys. Lett. B **202** (1988) 284.

[12] S. J. Barish et al., *Study of neutrino interactions in hydrogen and deuterium: Description of the experiment and study of the reaction* $\nu + d \to \mu^- + p + p_s$, Phys. Rev. D **16** (1977) 3103.

[13] K. L. Miller et al., *Study of the reaction* $\nu_\mu + n \to \mu^- p p_s$, Phys. Rev. D **26** (1982) 537.

[14] W. A. Mann et al., *Study of the reaction* $\nu + n \to \mu^- + p$, Phys. Rev. Lett. **31** (1973) 844.

[15] N. J. Baker et al., *Quasielastic neutrino scattering: A measurement of the weak nucleon axial-vector form factor*, Phys. Rev. D **23** (1981) 2499.

[16] T. Kitagaki et al., *High-energy quasielastic* $\nu_\mu n \to \mu^- p$ *scattering in deuterium*, Phys. Rev. D **28** (1983) 436.

[17] M. Holder et al., *Spark-chamber study of elastic neutrino interactions*, Nuovo Cim. A **57** (1968) 338.

[18] R. L. Kustom et al., *Quasielastic neutrino scattering*, Phys. Rev. Lett. **22** (1969) 1014.

[19] D. Perkins, in: *Proceedings of the* 16^{th} *International Conference on High Energy Physics*, J. D. Jackson, A. Roberts (eds.), National Accelerator Laboratory, Batavia, Illinois, 1973, Vol. IV, 189.

[20] A. Orkin-Lecourtois, C. A. Piketty, *The quasi-elastic events of the CERN bubble chamber neutrino experiment and the determination of the axial form factor*, Nuovo Cim. A **50** (1967) 927.

[21] S. Bonetti et al., *Study of quasi-elastic reactions of* ν *and* $\overline{\nu}$ *in Gargamelle*, Nuovo Cim. A **38** (1977) 260.

[22] N. Armenise et al., *Charged current elastic antineutrino interactions in propane*, Nucl. Phys. B **152** (1979) 365.

[23] I. Budagov et al., *A study of the elastic neutrino process* $\nu + n \to \mu^- + p$, Lett. Nuovo Cim. **2** (1969) 689.

[24] Particle Data Group, *Review of particle properties*, Phys. Rev. D **54** (1996).

[25] Particle Data Group, *Review of particle properties*, Eur. Phys. J. C **3** (1998) 622.

[26] A. S. Esaulov et al., *Longitudinal and transverse contributions to the threshold cross-section of single-pion electroproduction by a proton*, Nucl. Phys. B **136** (1978) 511.

[27] M. G. Olsson, E. T. Osypowski, E. H. Monsay, *Electroproduction of low hadronic masses*, Phys. Rev. D **17** (1978) 2938.

[28] E. Amaldi et al., *On pion electroproduction at* $5\,\text{fm}^{-2}$ *near threshold*, Nuovo Cim. A **65** (1970) 377.

[29] E. Amaldi et al., *Axial-vector form-factor of the nucleon from a coincidence experiment on electroproduction at threshold*, Phys. Lett. B **41** (1972) 216.

[30] P. Brauel et al., π^+*–electroproduction on hydrogen near threshold at four-momentum transfers of* 0.2, 0.4 *and* 0.6 GeV^2/c^2, Phys. Lett. B **45** (1973) 389.

[31] A. del Guerra et al., *Measurements of threshold* π^+ *electroproduction at low momentum transfer*, Nucl. Phys. B **99** (1975) 253.

[32] A. del Guerra et al., *Threshold* π^+ *electroproduction at high momentum transfer: a determination of the nucleon axial vector form factor*, Nucl. Phys. B **107** (1976) 65.

[33] P. Joos et al., *Determination of the nucleon axial vector form-factor from* $\pi\Delta$ *electroproduction near threshold*, Phys. Lett. B **62** (1976) 230.

[34] S. Choi, *Etude experimentale et theorique de l'electroproduction de pions pres du seuil mesure des facteurs de forme axial et pseudo-scalaire*, These No. 2643, Universite Paris XI Orsay, Paris 1993.

[35] S. Choi et al., *Axial and pseudo-scalar nucleon form factors from low energy pion electroproduction*, Phys. Rev. Lett. **71** (1993) 3927; see also comment in [82].

[36] Y. Nambu, M. Yoshimura, *Axial-vector form factor of nucleon determined from threshold electropion production*, Phys. Rev. Lett. **24** (1970) 25.

[37] E. D. Bloom et al., *Measurements of inelastic electron scattering cross sections near the one-pion threshold*, Phys. Rev. Lett. **30** (1973) 1186.

[38] D. Drechsel, L. Tiator, *Threshold pion photoproduction on nucleons*, J. Phys. G: Nucl. Part. Phys. **18** (1992) 449.

[39] D. Drechsel, O. Hanstein, S. S. Kamalov, L. Tiator, *An unitary isobar model for pion photo- and electroproduction on the proton up to* 1 GeV, Preprint MKPH–T–98–10, Mainz 1998.

[40] I. Blomqvist, J. M. Laget, *A non-relativistic operator convenient for analysis of pion photoproduction on nuclei in the* $\Delta(1236)$ *region*, Nucl. Phys. A **280** (1977) 405.

[41] J. M. Laget, *On the longitudinal electromagnetic coupling of the* Δ, Nucl. Phys. A **481** (1988) 765.

[42] R. G. Moorhouse, *Electromagnetic excitation and decay of hadron resonances*, in: A. Donnachie, G. Shaw (Eds.), *Electromagnetic interactions of hadrons*, Plenum, New York 1978, p. 83.

[43] T. W. Donnelly, A. S. Raskin, *Considerations of polarization in inclusive electron scattering from nuclei*, Ann. Phys. (USA) **169** (1986) 247.

[44] A. S. Raskin, T. W. Donnelly, *Polarization in coincidence electron scattering from nuclei*, Ann. Phys. (USA) **191** (1989) 78.

[45] J. D. Bjorken, S. D. Drell, *Relativistic quantum mechanics*, McGraw-Hill, New York 1964.

[46] L. N. Hand, *Experimental investigation of pion electroproduction*, Phys. Rev. **129** (1963) 1834.

[47] W. Bartel et al., *Electroproduction of pions near the* $\Delta(1236)$ *isobar and the form factor* $G_M^*(q^2)$ *of the* $(\gamma N\Delta)$ *vertex*, Phys. Lett. B **28** (1968) 148.

[48] W. Bartel et al., *Inelastic electron-proton scattering in the region of the* $\Delta(1236)$ *resonance*, Phys. Lett. B **35** (1971) 181.

[49] S. Galster et al., *Coincidence experiment on inelastic electron-proton scattering in the region of the* $\Delta(1236)$ *at* $q^2 = -0.35$ *and* $-1.0\,(\mathrm{GeV/c})^2$, Phys. Rev. D **5** (1972) 519.

[50] W. W. Ash et al., *Measurement of the* γNN *form factor*, Phys. Lett. B **24** (1967) 165.

[51] C. Mistretta et al., *Coincidence measurements of single-pion electroproduction near the* $\Delta(1236)$ *resonance*, Phys. Rev. **184** (1969) 1487.

[52] W. Albrecht et al., *π^0 electroproduction at $\Delta(1236)$ and a four-momentum transfer of $15\,\mathrm{fm}^{-2}$*, Nucl. Phys. B **25** (1970) 1.

[53] W. Albrecht et al., *Electroproduction of $\Delta(1236)$ in the π^0 channel at a four-momentum transfer of $25\,\mathrm{fm}^{-2}$*, Nucl. Phys. B **27** (1971) 615.

[54] R. D. Hellings et al., *Electroproduction of π^0 mesons in the region of the first pion-nucleon resonance*, Nucl. Phys. B **32** (1971) 179.

[55] R. Siddle et al., *Coincidence π^0 electroproduction experiments in the first resonance region at momentum transfers of $0.3, 0.45, 0.60, 0.76\,(\mathrm{GeV/c})^2$*, Nucl. Phys. B **35** (1971) 93.

[56] J. C. Alder et al., *π^0 electroproduction at the first resonance at momentum transfers $q^2 = 0.6, 1.0$ and $1.56\,\mathrm{GeV}^2$*, Nucl. Phys. B **46** (1972) 573.

[57] K. Bätzner et al., *π^0 electroproduction at the $\Delta(1236)$ resonance at a four-momentum transfer of $q^2 = 0.3\,(\mathrm{GeV/c})^2$*, Nucl. Phys. B **76** (1974) 1.

[58] C. W. Akerlof et al, *Measurement of the pion form factor*, Phys. Rev. **163** (1967) 1482.

[59] D. R. Boterill et al., *The polar-angle dependence in π^+–electroproduction near threshold*, Lett. Nuovo Cim. **10** (1974) 629.

[60] H. Breuker et al., *Forward π^+ electroproduction in the first resonance region at four-momentum transfers $q^2 = -0.15$ and $-0.3\,\mathrm{GeV}^2/\mathrm{c}^2$*, Nucl. Phys. B **146** (1978) 285.

[61] M. L. Goldberger, S. B. Treiman, *Conserved currents in the theory of Fermi interactions*, Phys. Rev. **110** (1958) 1478.

[62] G. Ecker, private communication.

[63] R. Dashen, M. Weinstein, *Experimental tests of theories of chiral symmetry breaking*, Phys. Rev. **188** (1969) 2330.

[64] B. R. Holstein, *Nucleon axial matrix elements*, Preprint nucl-th/9806036, and references [2–5] therein.

[65] P. Bopp et al., *Beta-decay asymmetry of the neutron and g_A/g_V*, Phys. Rev. Lett. **56** (1986) 919.

[66] B. G. Erozolimskii et al., *New measurements of the electron-neutron spin asymmetry in neutron beta-decay*, Phys. Lett. B **263** (1991) 33; see also the Corrigendum in Phys. Lett. B **412** (1997) 240.

[67] K. Schreckenbach et al., *A new measurement of the beta emission asymmetry in the free decay of polarized neutrons*, Phys. Lett. B **349** (1995) 427.

[68] P. Liaud et al., *The measurement of the beta asymmetry in the decay of polarized neutrons*, Nucl. Phys. A **612** (1997) 53.

[69] H. Abele et al., *A measurement of the beta asymmetry A in the decay of free neutrons*, Phys. Lett. B **407** (1997) 212.

[70] R. Koch, E. Pieterinin, *Low-energy πN partial wave analysis*, Nucl. Phys. A **336** (1980) 331.

[71] R. Arndt et al., *Determination of the πNN coupling constant from elastic pion-nucleon scattering data*, Phys. Rev. Lett. **65** (199) 157.

[72] N. M. Kroll, M. A. Ruderman, *A theorem on photomeson production near threshold and the suppression of pairs in pseudoscalar meson theory*, Phys. Rev. **93** (1954) 233.

[73] Y. Nambu, D. Lurié, *Chirality conservation and soft pion production*, Phys. Rev. **125** (1962) 1429.

[74] Y. Nambu, E. Shrauner, *Soft pion emission induced by electromagnetic and weak interactions*, Phys. Rev. **128** (1962) 862.

[75] G. Furlan, N. Paver, C. Verzegnassi, *Low-energy electroproduction and equal-time commutators*, Nuovo Cim. A **70** (1970) 247.

[76] C. Verzegnassi, *Low energy photo- and electroproduction, multipole analysis by current algebra commutators*, Springer Tracts in Modern Physics **59** (1971) 154, Springer Verlag, Berlin 1971.

[77] G. Furlan, N. Paver, C. Verzegnassi, *Low energy theorems and photo- and electroproduction near threshold by current algebra*, Springer Tracts in Modern Physics **62** (1972) 118, Springer Verlag, Berlin 1972.

[78] N. Dombey, B. J. Read, *Pion electroproduction and photoproduction including PCAC*, Nucl. Phys. B **60** (1973) 65.

[79] B. J. Read, *Threshold electroproduction experiments and the axial vector form factor*, Nucl. Phys. B **74** (1974) 482.

[80] G. Benfatto, F. Nicolò, G. C. Rossi, *Implications of gauge invariance for pion electroproduction at threshold*, Nucl. Phys. B **50** (1972) 205.

[81] G. Benfatto, F. Nicolò, G. C. Rossi, *Pion electroproduction at threshold*, Nuovo Cim. A **14** (1973) 425.

[82] V. Bernard, N. Kaiser, U.–G. Meißner, *Determining the axial radius of the nucleon from data on pion electroproduction*, Phys. Rev. Lett. **69** (1992) 1877; see also comment to [35] in Phys. Rev. Lett. **72** (1994) 2810.

[83] K. I. Blomqvist et al. (A1 Collaboration), *Measurement of* $\mathrm{H(e,e'\pi^+)n}$ *in parallel kinematics*, Proposal A1/2–90, Mainz 1990.

[84] A. W. Richter, *Trennung des longitudinalen, transversalen und longitudinal-transversal interferierenden Anteils des Wirkungsqerschnitts der Reaktion* $\mathrm{H(e,e'\pi^+)}$ *in der Nähe der Pionschwelle*, Dissertation KPH 21/94, Institut für Kernphysik, Universität Mainz, Mainz 1994.

[85] K. I. Blomqvist et al. (A1 Collaboration), *Precise pion electroproduction in the* $\mathrm{p(e,e'\pi^+)n}$ *reaction at* $W = 1125\,\mathrm{MeV}$, Z. Phys. A **353** (1996) 415.

[86] A. P. Liesenfeld, Dissertation, in preparation.

[87] W. U. Boeglin, *Coincidence experiments with electrons*, Czech. J. Phys. **45** (1995) 295.

[88] I. Ewald, *Entwicklung und Erprobung einer langen, dünnen Flüssig-Wasserstoff-Targetzelle*, Diplom KPH 5/96, Institut für Kernphysik, Universität Mainz, Mainz 1996.

[89] S. Schardt, *Aufbau und Erprobung der Drei-Spektrometer-Anordnung für Koinzidenzexperimente mit Elektronen am* 855 MeV Elektronbeschleuniger MAMI, Dissertation KPH 8/95, Institut für Kernphysik, Universität Mainz, Mainz 1994.

[90] K. I. Blomqvist et al. (A1 Collaboration), *The three-spectrometer facility at the Mainz microtron MAMI*, Nucl. Instr. Meth. A **403** (1998) 263.

[91] M. Korn, *Entwicklung des Bahnrückverfolgungsverfahrens für die Drei-Spektrometer Anlage und experimentelle Bestimmung der Abbildungseigenschaften der Spektrometer A und B mit elastischer Elektronenstreuung*, Dissertation KPH 4/95, Institut für Kernphysik, Universität Mainz, Mainz 1994.

[92] H. Kramer, *Grundlagen für das Steuerungs- und Überwachungssystem der Drei-Spektrometer-Anlage am Elektronenbeschleuniger MAMI*, Dissertation, Institut für Kernphysik, Universität Mainz, Mainz 1994.

[93] K. Herter, *Entwicklung und Erprobung eines Verfahrens zur Messung der absoluten Energie des Elektronenstrahls von MAMI*, Diplom KPH 5/1992, Institut für Kernphysik, Universität Mainz, Mainz 1992.

[94] M. Distler, *Aufbau und Test einer vertikalen Driftkammer*, Diplom KPH 7/1990, Institut für Kernphysik, Universität Mainz, Mainz 1990.

[95] M. Kahrau, *Aufbau der vertikalen Driftkammern des Spektrometers C an MAMI*, Diplom KPH 5/1993, Institut für Kernphysik, Universität Mainz, Mainz 1993.

[96] A. Wagner, *Aufbau eines Laser-Monitor-Systems für die Spektrometerdetektoren*, Diplom KPH 7/92, Institut für Kernphysik, Universität Mainz, Mainz 1992.

[97] S. Kowalski, H. A. Enge, *Raytrace*, LNS and Dept. of Physics, MIT, Cambridge 1987.

[98] M. Kuss, *Elektroproduktion von geladenen Pionen an* ^{3}He *und die Suche nach Delta-Baryonen im Grundzustand des* ^{3}He, Dissertation, TH Darmstadt, Darmstadt 1996.

[99] R. A. Arndt, I. I. Strakovsky, R. L. Workman, *Updated resonance photodecay amplitudes to* 2 GeV, Phys. Rev. C **53** (1996) 430; see also [100].

[100] R. A. Arndt, I. I. Strakovsky, R. L. Workman, *Pion photoproduction in the* Δ *resonance region*, Phys. Rev. C **56** (1997) 577.

[101] O. Hanstein, D. Drechsel, L. Tiator, *Multipole analysis of pion photoproduction based on fixed-*t *dispersion relations and unitarity*, Nucl. Phys. A **632** (1998) 561.

[102] D. Drechsel, G. Krein, *The Gerasimov-Drell-Hearn sum rule and the single-pion photoproduction multipole* E_{0+} *close to threshold*, Phys. Rev. D **58** (1998) 116009.

[103] J. D. Bjorken, S. D. Drell, *Relativistic quantum fields*, McGraw-Hill, New York 1965.

[104] A. Chodos et al., *New extended model of hadrons*, Phys. Rev. D **9** (1974) 3471.

[105] A. Chodos et al., *Baryon structure in the bag theory*, Phys. Rev. D **10** (1974) 2599.

[106] R. Tegen, M. Schedl, W. Weise, *On the axial charge and other static properties of the quark core in nucleons*, Phys. Lett. B **125** (1983) 9.

[107] J. F. Donoghue, E. Golowich, B. R. Holstein, *Dynamics of the standard model*, Cambridge University Press, Cambridge 1994, p. 316.

[108] R. Tegen, W. Weise, *The nucleon axial form factor and the pion-nucleon vertex function*, Z. Phys. A **314** (1983) 357.

[109] M. Rho, *Pions and the chiral bag*, Prog. Part. Nucl. Phys. **8** (1982) 103.

[110] G. E. Brown, *Nucleon-nucleon forces from bags, quarks and boson exchange*, Prog. Part. Nucl. Phys. **8** (1982) 147.

[111] V. Vento, *Chiral pion dynamics for spherical nucleon bags*, Nucl. Phys. A **345** (1980) 413.

[112] G. A. Miller, A. W. Thomas, S. Théberge, *Pion-nucleon scattering in the Brown-Rho bag model*, Phys. Lett. B **91** (1980) 192.

[113] G. A. Miller, A. W. Thomas, S. Théberge, *Pionic corrections to the MIT bag model: the $(3,3)$ resonance*, Phys. Rev. D **22** (1980) 2823.

[114] A. W. Thomas, *Chiral symmetry and the bag model: a new starting point for nuclear physics*, Adv. Nucl. Phys. **13** (1983) 1.

[115] W. Weise, *Quarks, chiral symmetry and dynamics of nuclear constituents*, in: W. Weise (ed.), *Quarks and nuclei*, World Scientific, Singapore 1984, p. 57.

[116] M. Fiolhais, *Description of static properties of the nucleon in the framework of the sigma model with quarks*, Doctoral thesis, University of Coimbra, Coimbra 1988.

[117] S. Fubini, G. Furlan, *Dispersion theory of low-energy limits*, Ann. Phys. (USA) **48** (1968) 322.

[118] E. Braaten S. Tse, C. Wilcox, *Electroweak form factors of the Skyrmion*, Phys. Rev. D **34** (1986) 1482.

[119] U.–G. Meißner, N. Kaiser, W. Weise, *Nucleons as Skyrme solitons with vector mesons: electromagnetic and axial properties*, Nucl. Phys. A **466** (1987) 685.

[120] P. Alberto et al., *Form factors in the projected linear chiral sigma model*, Zeit. Phys. A **336** (1990) 449.

[121] P. Alberto, *Form factors in chiral soliton models with quarks*, Doctoral thesis, University of Coimbra, Coimbra 1991.

[122] T. Neuber, K. Goeke, *Peierls-Yoccoz linear and angular momentum projected observables in the linear chiral sigma model*, Phys. Lett. B **281** (1992) 202.

[123] T. Neuber, *Analyse spurioser Schwerpunktbewegungen in effektiven chiral-invarianten Solitonmodellen mit Valenzquarks*, Berichte der KFA Jülich, JÜL–2797, Jülich 1993.

[124] E. G. Lübeck, M. C. Birse, E. M. Henley, L. Wilets, *Momentum projection and relativistic boost of solitions: Coherent states and projection*, Phys. Rev. D **33** (1986) 234.

[125] A. Drago, M. Fiolhais, U. Tambini, *Recoil effects on nucleon electromagnetic form factors*, Nucl. Phys. A **609** (1996) 488.

[126] D. Baumann, Dissertation, in preparation.

[127] M. Ding, Dissertation, in preparation.

[128] S. R. Amendolia et al., *A measurement of the pion charge radius*, Phys. Lett. B **146** (1984) 116.

[129] S. R. Amendolia et al., *A measurement of the kaon charge radius*, Phys. Lett. B **178** (1986) 435.

[130] R. P. Feynman, M. Gell-Mann, *Theory of the Fermi interaction*, Phys. Rev. **109** (1958) 193.

[131] P. Renton, *Electroweak Interactions*, Cambridge University Press, Cambridge 1990, p. 397.

[132] J. Templon, *Few-body physics*, summary talk at the "Nuclear and Particle Physics with CEBAF at Jefferson Lab" Meeting, Dubrovnik, Croatia, November 3–10, 1998, to be published.

[133] D. H. Perkins, *Introduction to High Energy Physics*, 3rd Edition, Addison-Wesley, 1987, p. 195 and the reference therein.

[134] G. F. Chew, M. L. Goldberger, F. E. Low, Y. Nambu, *Relativistic dispersion relation approach to photomeson production*, Phys. Rev. **106** (1957) 1345.

[135] A. Donnachie, *Photo- and electroproduction processes*, in: E. H. S. Burhop (Ed.), *High energy physics*, Academic press, New York 1972, 1.

[136] F. A. Berends, A. Donnachie, D. L. Weaver, *Photoproduction and electroproduction of pions: (I) Dispersion relation theory*, Nucl. Phys. B **4** (1967) 1.

[137] L. W. Mo, Y. S. Tsai, *Radiative corrections to elastic and inelastic* ep *and* μp *scattering*, Rev. Mod. Phys. **41** (1969) 205.

[138] L. C. Maximon, *Comments on radiative corrections*, Rev. Mod. Phys. **41** (1969) 193.

[139] E. N. M. Quint, *Limitations of the mean-field description for nuclei in the* Pb *region, observed with the* $(e, e'p)$ *reaction*, Doctoral thesis, Vrije Universiteit te Amsterdam, Amsterdam 1988.

[140] J. Schwinger, *On radiative corrections to electron scattering*, Phys. Rev. **75** (1949) 898.

[141] F. Bloch, A. Nordsieck, *Note on the radiation field of the electron*, Phys. Rev. **52** (1937) 54.

[142] J. Friedrich, *Radiation tail and radiative corrections for elastic electron scattering*, Nucl. Instr. Meth. **129** (1975) 505.

[143] L. Landau, J. Phys. USSR **8** (1944) 201.

[144] D. J. S. Findlay, A. R. Dusautoy, *Improvements to the Blunck-Leisegang energy loss straggling distribution*, Nucl. Instr. Meth. **174** (1980) 531.

[145] W. R. Leo, *Techniques for nuclear and particle physics experiments*, 2nd Edition, Springer Verlag, Berlin 1994.

[146] M. Gell-Mann, M. Lévy, *The axial vector current in beta decay*, Nuovo Cim. **16** (1960) 705.

[147] C. Itzykson, J.–B. Zuber, *Quantum field theory*, McGraw–Hill, New York 1985.

[148] H. B. Nielsen, A. Patkós, *Effective dielectric theory from QCD*, Nucl. Phys. B **195** (1982) 137.

[149] T. Neuber, M. Fiolhais, K. Goeke, J. N. Urbano, *Nucleon description in a projected chiral soliton model with dynamical confinement*, Nucl. Phys. A **560** (1993) 909.

[150] A. Drago, M. Fiolhais, U. Tambini, *Quark matter in the chiral color-dielectric model*, Nucl. Phys. A **588** (1995) 801.

[151] C. Amsler, F. E. Close, *Evidence for a scalar glueball*, Phys. Lett. B **353** (1995) 385.

[152] C. Amsler, F. E. Close, *Is* $f_0(1500)$ *a scalar glueball?*, Phys. Rev. D **53** (1996) 295.

[153] M. C. Birse, *Chiral model of the nucleon: Projecting the hedgehog as a coherent state*, Phys. Rev. D **33** (1986) 1934.

Index

A

accelerator, MaMi–B, 16
acceptance, calculation, 42
acceptance, nominal, 42
accidental coincidences, 16, 30
ADC, time gate, 28
axial coupling constant, 5, 53
axial current, CBM, 55
axial current, divergence of, 55
axial current, MIT bag, 54
axial form factor, 2
axial form factor, calculation, 53
axial form factor, data, 3
axial form factor, formal definition, 58
axial form factor, from neutrino scattering, 70
axial form factor, in LSM and CDM, 60, 62, 63, 88, 127
axial form factor, 'normalised', 66
axial form factor, 'unnormalised', 63
axial mass, 4
axial mass discrepancy, 4
axial mass, definition, 3, 46, 51
axial mass, extraction, 46, 51
axial radius, definition, 3
axial-vector coupling constant, 53

B

background reduction, 33
bag, 54
bare resonances, 83
beam current, maximum, 17
beam current, measurement, 18, 19
beam energy, final, 17
beam energy, gain per turn, 17
beam monitor, HF, 19
beam wobbler, 17, 18
bispinor, for valence quarks, 86
Bloch-Nordsieck theorem, 80
boosting, 61
Born approximation, plane-wave, 6
Born terms, 83
Breit frame, hadron, 59
Breit-Wigner parameterisation, 82, 83
Bremsstrahlung, external, 80
Bremsstrahlung, internal, 78

C

centre-of-mass corrections, 54
Čerenkov detectors, 24
chiral bag models, 55
chiral perturbation theory, conventional, 13
chiral perturbation theory, generalised, 13
chiral soliton models, 56
chiral symmetry, 12, 55
'clam-shell' dipole, 22
cloudy bag model, 55
CMS, of the final hadrons, 9
coherent states, for mesons, 87
coincidence efficiency, 37
coincidence experiments, with electrons, 1
coincidence experiments, with hadrons, 1
coincidence gate, 30
coincidence peak, width, 31
coincidence PLU, 27
coincidence TDC, 29
coincidence time, 29
coincidence time, corrected, 30
coincidence time, raw, 30
confining potential in CDM, quadratic, 66, 85
confining potential in CDM, quartic, 66
correction factor, 40, 77

correction factor, exponentiation, 79, 80
correction factors, averaged, 78
cross-section, differential, 7, 10, 44
cryo-target, 17
current conservation, 49
cut-off energy, 40, 77
CVC hypothesis, 70

D

Dashen-Weinstein theorem, 13
dead time correction, 37
detector efficiencies, 34
Dirac operators, 71
Dirac-Pauli form factors, 69
dispersion, 21
dispersive plane, 21
drift chambers, resolution, 23
drift chambers, trajectory reconstruction, 23
drift chambers, vertex reconstruction, 23
duty factor, 16

E

effective Lagrangian model, 49, 82
efficiencies, VDC, 34
efficiency, Čerenkov detectors, 36
efficiency, coincidence, 37
efficiency, overall VDC, 35
efficiency, scintillator detectors, 36
efficiency, single wire VDC, 34
eigenstates, of linear momentum, 60
eigenstates, of spin and isospin, 57
electro-magnetic current, 69
electronic factors, 8
electronics, individual spectrometer, 25
electronics, 25
energy loss, in acceptance simulation, 43
energy-momentum relation, 61
equivalent photon energy, 10
equivalent radiators, 80
event module, 28
exclusive experiments, 2
exponentiation, of correction factor, 79, 80
external radiators, 80

F

Fermi interaction, 69
Fermi-Watson theorem, 83
focal plane, 21, 23
forward-peaking approximation, 78
Förster probe, 19

G

gauge invariance, 49
glue-balls, 85
Goldberger-Treiman discrepancy, 12
Goldberger-Treiman relation, 12

H

hadronic probes, 1
hadronic structure functions, 8
hadronic tensor, 6
Hall probe, 22
hedgehog Ansatz, for pions, 87
hedgehog Ansatz, for quarks, 86
HF beam monitor, 19

I

inclined pole faces, 21
inclusive experiments, 2
interrupt, from coincidence PLU, 28
invariant amplitudes, 71
invariant mass, 10
ionisation losses, 81
isobar model, 82
isospin decomposition, 76

K

knock-out, one nucleon, 2

L

Lagrangians, of LSM and CDM, 84
Landau energy straggling, 81
laser monitoring system, 25
leptonic current, 69
leptonic factors, 8
leptonic tensor, 6, 8
liquid hydrogen cryo target, 17
luminosity, 40

M

μBusy module, 28
magnetic field, measurement, 22
magnetic spectrometers, parameters, 20
magnification, 21
MaMi–B accelerator, 16
matrix element, invariant, 7
missing mass, 31
MIT bag model, 54, 58
mixing parameter, 83
model wave-function, of LSM and CDM, 86
most probable energy loss, 78, 81
multipole expansion, 71
muon contamination, 33
muon contamination, simulation of, 38

N

NMR probes, 22
non-relativistic constituent quark model, 54
non-resonant background, 82

P

parallel kinematics, 45
parallel-to-point imaging, 21
PCAC, 82
Peierls-Yoccoz projection, 57, 61
photon, polarisation, 10
photon, degree of polarisation, 10
photon, longitudinal polarisation, 10
photon, transverse polarisation, 10
pion decay, 37
pion decay correction, 37
pion decay length, 38
pion decay time, 38
pion field, Yukawa form, 56
pion form factor, extraction, 46, 51
plane-wave Born approximation, 6
PLU, clear, 27
PLU, coincidence, 27
PLU, programming, 27
PLU, spectrometer, 25
PLU, strobe, 27
point-to-point imaging, 21
pole face curvature, 21
positron background, 33
projection operator, linear momentum, 61
projection operator, spin-isospin, 57
projection, of linear momentum, 60
projection, Peierls-Yoccoz, 57, 61
proton background, 34
pseudo-scalar coupling, 82
pseudo-vector coupling, 49, 82

Q

quark mass, dynamical generation in CDM, 85
quasi-elastic neutrino scattering, 69
quasi-elastic scattering, 1

R

racetrack microtron, 17
radiation loss corrections, 39
radiation losses, 40, 77
radiation losses, correction of, 40
radiative tails, 40, 77
raw detector data, 25
reaction plane, 7
reaction point, in acceptance simulation, 43
recoil effects, 5, 15
recoil factor, 7
reference trajectory, 21
rescattering effects, 83
resonant amplitudes, 82
retiming, 27
Rosenbluth separation, 45

S

Sachs form factors, 70
scalar confining potential, models with, 54, 58
scattering plane, 7
Schwinger radiation, 78
scintillator detector, layers, 24
scintillator detector, segmentation of, 24
scintillator paddles, 24
sextupole magnet, 21
signal-to-noise ratio, 16
spectrometer imaging modes, 21
spectrometer magnetic field, measurement, 22
spectrometer PLU, signals, 27
spectrometer PLU, 25

spherical aberrations, 21
spurious centre-of-mass motion, 5, 15, 54
static approximation, 59

T

target, cryogenic, 17
TDC, stop for drift chambers, 28
time-of-flight detectors, 24
timing detectors, 24
timing, in a double-arm experiment, 29
trajectory reconstruction, using VDCs, 23
trigger detectors, 24
trigger system, 25
true coincidences, 30

U

unitarisation, 83

V

variation after projection, in CDM, 66
variation after projection, in LSM, 63
vector meson exchange, 83
vertex corrections, to the resonance, 83
vertex reconstruction, using VDCs, 23
virtual photon, 6
virtual photon flux, 10

W

weak form factors, 69
weak hadronic current, 69
wobbler, 17